NONLINEAR RECTIFICATION OF QUATERNARY CLIMATE DRIVERS AT HIGH AND LOW LATITUDES

A DISSERTATION SUBMITTED TO THE GRADUATE DIVISION OF THE UNIVERSITY OF HAWAI'I AT MĀNOA IN PARTIAL FULFILLMENT OF THE REQUIREMENTS FOR THE DEGREE OF

DOCTOR OF PHILOSOPHY

IN

OCEANOGRAPHY

DECEMBER 2015

By

Michelle Tigchelaar

Dissertation Committee:

Axel Timmermann, Chairperson
Niklas Schneider
Oliver Elison Timm
Richard Zeebe
Gregory Ravizza

Acknowledgments

First and foremost I would like to thank my advisor, Axel Timmermann. Axel, you have taught me so much about science, and I continue to be amazed by your boundless curiosity and sharp mind every day. But perhaps more importantly, I am forever grateful for the continued personal support you have shown over the years – from the first warm welcome more than five years ago, to your excitement (at times) about my student activism and your deep concern over my future (academic) career. I would also like to thank my committee members – Gregory Ravizza, Niklas Schneider, Oliver Elison Timm and Richard Zeebe – for their patience and critical feedback. Paul Kemp, Jay McCreary and Kelvin Richards were part of earlier committee iterations, and took an important role in shaping my academic path. Thank you to Kristin, Catalpa, Pamela, Lance, Jeanie, Amy, Eby, Katie, Dave, Ron and Sharon for their administrative and technical support. I am also thankful for the opportunity to learn from David Ho and Kevin Weng as we taught OCN310 together. Many thanks to Fei-Fei Jin and Pedro DiNezio for sharing their insights on tropical hydroclimate and paleoclimatology.

The PhD process is an intensely solitary one, but I wouldn't have been able to go through it without the support of the many friends I made along the way. Thank you to Kelly, for being my first friend in the islands, and for taking the sharp edges of my judgmental Dutchness; to Johanna, for joining me to the dark end and back, and drinking lots of coffee and beer along the way (and to Josiah, for helping with the latter); to Adrienne, for laughing uncontrollably as I was bleeding dry; to Tom, for six pencils; to Gen, for five years of shared meals and a shared home (and Xue, for visiting!); to Angeles, for embracing bad TV habits; to Audine and Axel L., for your radiating happiness and love

of good food, both here and far away; to Malte I and Malte II, for showing me that one can never know too many Maltes (and to Christine for marrying one); to Andrew, for taking me out into the real world. Thank you also to my current and former office mates and fellow Oceanography students for making life in the department so much more enjoyable: Alyssa, other Michelle, Colette, Seth, Katie, Sherry, Øyvind, Adam, and all you other lovers of the ocean. Our lunch breaks were always filled with good conversation, be it science or otherwise, thanks to Tobias, Megumi, Yoshi, Matthew, Sam, Shayne, Nat and Neven.

I am incredibly proud of the time I spent with the UHM Graduate Student Organization, especially the year when I had the honor of being its president. To all the members of the 2014–2015 Executive Committee – Rebekah, Amanda, Tom, Adrienne, Jonathan, Nick, Bret, Victor, Leilei, Richard, Nathalie, Duyen, Daisy, Camila, Amber and Elita – and also Aaron, Kristine and Vincent: thank you all for your dedication, energy, care and friendship. I am also grateful to Dean Krystyna Aune and Vice Chancellor Lori Ideta for the many encouraging conversations we had.

The wonderful women of my Hui Nalu paddling team are to thank for keeping me (somewhat) in shape. I would like to thank in particular Jenny Webster and Mary Tschann for taking our teamwork out of the boat and into the bar. The terrific athletes of my marathon training group have kept me sane and going during the last stages of dissertation writing, and for that I am thankful as well.

I also think back fondly on the time I got to spend in Japan. I would like to thank Naomi Harada and Kimoto Katsunori ("Kimopi") for their support and hospitality aboard R/V MIRAI in 2011; and Mario Uchimiya, Shotaro Suzuki, Yuichi Hayasaki, and especially Jaeho Song, for their friendship at sea, and after. During the six months I spent at AORI in the winter of 2013–2014, I was lucky to work, discuss science and spend my lunch breaks with Ayako Abe-Ouchi, Yusuke Okazaki, Yusuke Yokoyama, Megumi Ookata, Makiko ("Makki") Hashimoto, Michiya Hayashi, Junya Uchida, Sam Sherif, Takashi Obase and the others in the Abe-ken and our third floor office. I am thankful to the many amazing people of the Kashiwanoha Lodge for creating such a powerful international buffer zone: Sonia, Sara, Rene, Blaz, Hagar, Vivek, Rohit, Moha and many others; and to Ben and Debbie for explorations on the other side of the Bay.

Last but not least, I am humbled by the tremendous support I received from my parents, my 'little' brother Yvo, my extended family (especially tante Ria), family friends and the many amazing people in the Netherlands (and elsewhere abroad) whom – even after living abroad for 5+ years – I am still fortunate enough to be able to call my friends: Lianne, Vincent, Gitte, Tetje & Bartjan, Merel, Victoria, Gwen, Floris Jan, Leanthe, Charlotte, Stijn, Nicole, Steven, Michou, Marie-Jette, Sietske and Jessica. Thank you for all your visits, cards, boxes of Sinterklaas candy, emails, Skype calls and messages from different time zones. Even though you were far away, it felt like you were always there.

Finally I am much obliged to the National Science Foundation (grants #1010869 and 1341311) for their generous support of my research.

Abstract

Variations in earth's climate are externally driven by changes in earth's orbit around the sun – orbital forcing, namely precession, eccentricity and obliquity – on timescales of 10^4–10^5 years. During the Quaternary, from 2.6 million years ago to present, these orbital drivers caused large oscillations of earth's climate system between cold glacials and relatively warm interglacials. The evolution of earth's climate however is not directly proportional to this orbital insolation forcing. For instance, reconstructions of (annual mean) paleoclimate show substantial variability on precessional time scales, even though there is no change in annual mean insolation associated with the precessional forcing. This means that nonlinear mechanisms rectify the zero-annual-mean precessional forcing into an annual mean climate response. Further, during the Late Quaternary (beginning roughly 800,000 years ago (800 ka)), glacial cycles have had a dominant period of ∼100 ka, a period not associated with a dominant orbital parameter. Feedbacks internal to the earth system thus amplify and modulate the external drivers. The Northern Hemisphere ice sheets are thought to be most directly sensitive to orbital insolation forcing, while other parts of the climate system – such as the tropics and the southern high latitudes – might respond more indirectly to the 100 ka earth system response. This dissertation explores the nonlinearities of precessional rectification and 100 ka modulation throughout the Late Quaternary at low and high latitudes.

Many records of tropical hydroclimate show substantial variability on precessional timescales. Part I of this dissertation aims to identify the nonlinear mechanisms responsible for rectifying the seasonal precessional forcing into an annual mean precipitation response. The traditional view

of precessionally-forced precipitation changes is that tropical precipitation increases with summer insolation. By comparing two simulations with an earth system model (CESM1.0.3), this paradigm is found to be true for continental but not for oceanic changes in precipitation. Focusing on the Atlantic Intertropical Convergence Zone (ITCZ), it is found that the continental temperature and precipitation response to precessional forcing are key rectifiers of annual mean precipitation over the ocean. A boundary layer response to temperature changes over northern Africa affects the *meridional position* of the ITCZ over the North Atlantic in boreal spring and summer, but not in fall and winter. Over the equatorial and South Atlantic, the *intensity* of precipitation is strongly impacted by diabatic forcing from the continents through an adjustment of the full troposphere. Although the top of atmosphere insolation forcing is seasonally symmetric, continental precipitation changes are largest in boreal summer, thus skewing the annual mean response. While the precessional forcing has only meridional gradients, the climatic response has strong zonal components. An important implication of this work is therefore that traditional zonal mean frameworks for assessing the ITCZ response to external forcing do not apply in the case of strong tropical insolation forcing. The response of tropical precipitation to external forcing thus depends on the ratio of tropical (i.e., precessional) to extratropical (i.e., 100 ka) forcing.

The Antarctic ice sheet (AIS) has varied substantially during the Late Quaternary, contributing more than 10 m to glacial sea level drop, and an estimated 3–6 m to interglacial sea level highstands. With its large marine margins, the AIS is sensitive to oceanic as well as atmospheric forcing, but the relative contributions of Quaternary climate forcings remain poorly constrained, with previous modeling studies relying heavily on parameterizations of past climate evolution. The evolution of northern and southern polar ice sheets appears to be synchronous on orbital timescales, which is somewhat unexpected given that precession – essential for Northern Hemisphere glacial terminations through its impact on summer insolation – is anti-phased between the hemispheres. Part II of this dissertation studies the drivers of AIS evolution over the last 800 ka by forcing an Antarctic ice sheet model with spatially and temporally varying climate anomalies from a transient simulation with an earth system model (LOVECLIM), in addition to reconstructions of global sea level change.

The simulated AIS evolution has a glacial-interglacial amplitude of 10–12 m sea level equivalent. Sensitivity experiments in which atmospheric, ocean temperature and sea level forcing are applied individually show that the full ice sheet response is a non-linear superposition of the individual drivers. The Northern Hemisphere sea level forcing impacts Antarctic ice volume by driving changes in the grounding line position. This grounding line migration modulates the Antarctic response to other climatic drivers: for both accumulation and oceanic melt rates the changes in configuration of the grounded ice sheet dominate over the glacial-interglacial climate forcing. Surface melt rates peak when austral summers are long, especially during periods of high annual mean temperature corresponding to high CO_2. These melt peaks provide a critical contribution to Antarctic deglaciation and are in phase with Northern Hemisphere summer insolation. Thus, on glacial timescales, Antarctica and the Northern Hemisphere ice sheets vary in unison through their respective orbital forcings, changes in global sea level, and CO_2.

Table of Contents

Acknowledgments . . . iii

Abstract . . . vii

List of Tables . . . xiii

List of Figures . . . xv

1 Introduction . . . 1

1.1 Earth's climate history in review . . . 1

1.2 Rectification in the climate system . . . 9

1.3 Dissertation outline . . . 14

I Rectification mechanisms at low latitudes 17

2 Mechanisms rectifying the annual mean response of tropical Atlantic rainfall to precessional forcing . . . 19

2.1 Introduction . . . 20

2.2 Methods . . . 26

2.3 Results . . . 29

2.4 Discussion . . . 47

2.5 Summary & Conclusion . . . 53

II Rectification mechanisms at high latitudes 57

3 Nonlinear response of the Antarctic ice sheet to Quaternary sea level and climate forcing 59

3.1 Introduction . . . 60

3.2 Methods . . . 63

3.3 Results . . . 72

3.4 Discussion and Conclusions . . . 84

4 Mechanisms of Late Quaternary bipolar ice sheet synchronization . . . 89

4.1 Introduction . . . 90

4.2 Methods . . . 91

4.3 Late Quaternary Antarctic climate variability . . . 93

4.4 Climatic drivers of AIS evolution . . . 96

4.5 Conclusions . . . 101

5 Synthesis . . . 103

5.1 Summary of main findings . . . 103

5.2 Discussion and Outlook . . . 109

A Atlantic moisture budget analysis . . . 115

B Antarctic mass balance during terminations . . . 121

Bibliography . . . 125

List of Tables

2.1 Overview of the experimental setup for the simulations with CESM1.0.3. 28

2.2 Seasonally and annually integrated P_{MAX}–P_{MIN} difference in total precipitation (m^3 and %) over the South American continent (80°W–40°W, 30°S–10°N), Atlantic Ocean (60°W–20°E, 20°S–20°N) and African continent (10°W–30°E, 30°S–30°N) 33

3.1 Overview of the sensitivity experiments described in Sect. 3.2.2 70

List of Figures

1.1 Earth's climate history throughout the Cenozoic, as indicated by the benthic $\delta^{18}O$ record. Generally, high $\delta^{18}O$ values indicate low temperatures, and vice versa. The top figure shows $\delta^{18}O$ values collected by Zachos et al. (2001); the bottom two figures show the Lisiecki & Raymo (2005) record. 3

1.2 Drivers of Late Quaternary climate variability – (A) illustration of orbital parameters: variations in earth's tilt – obliquity (ϵ), variations in how elliptical earth's orbit is – eccentricity (solid and dashed orbit and sun), variations in timing of perihelion – precession (solid and dashed earth; measured by angle $\overline{\omega}$); (B) monthly insolation anomalies (shading) and annual mean insolation (black) in W m^{-2} at 20 °N; (C) monthly insolation anomalies (shading) and annual mean insolation (black) in W m^{-2} at 65 °S; (D) atmospheric CO_2 concentrations from the EPICA Dome C ice core (Lüthi et al., 2008). 6

1.3 Theoretical example of nonlinear rectification – (A) seasonal insolation forcing (Q_{seas}) over the past 100 ka (Laskar et al., 2004); (B) rectified seasonal insolation forcing (Q_{rect}) according to Eq. 1.1; (C) annual mean of seasonal insolation forcing in (A) (black) and rectified seasonal insolation forcing in (B) (red). 12

2.1 (A) Paleorecords of tropical hydroclimate against the precessional cycle ($e\sin(\omega)$, see Methods; grey); from top to bottom: composite of speleothem $\delta^{18}O$ from Chinese caves (25–32°N): Dongge (Dykoski et al., 2005), Hulu (Wang et al., 2004b), Sanbao (Wang et al., 2008); North African humidity index (20.8°N) (Tjallingii et al., 2008); sediment total reflectance in Cariaco Basin (10.7°N) (Deplazes et al., 2013); salinity reconstruction from Ba/Ca in Eastern Atlantic (2.5°N) (Weldeab et al., 2007); ln(Ti/Ca) from West Pacific Warm Pool (2.5°S) (Tachikawa et al., 2014); sediment gamma radiation from Bolivia (20.3°S) (Fritz et al., 2004); speleothem $\delta^{18}O$ from Botuvera cave (Brazil; 27.2°S) (Wang et al., 2004b, Cruz et al., 2005, Wang et al., 2007). Records are ordered from north to south, with inferred precipitation increasing along the y-axis; A 1000-year running mean was applied to each record. (B) Precessional phase ω (see Methods) of the 25% highest values of the records in (A), scaled by amplitude. Colors correspond to the records of (A) 21

2.2 Top: Zonal mean shortwave radiation at the top of the atmosphere for (A) P_{MIN} ($[Q_{IN}]$) and (B) P_{MAX}–P_{MIN} ($[\delta Q_{IN}]$); Bottom: Zonal mean surface shortwave radiation for (E) P_{MIN} ($[Q_{SW}]$) and (F) P_{MAX}–P_{MIN} ($[\delta Q_{SW}]$). Insets on the right show the annual mean change. A detailed description of these various terms can be found in Section 2.1 . . . 24

2.3 Annual mean precipitation (top) and seasonality of precipitation (maximum minus minimum of monthly climatology; bottom) for CMAP monthly climatology (enhanced version, left; Xie & Arkin, 1997) and CESM1.0.3 pre-industrial control run (right; Chikamoto et al., 2015) 27

2.4 Annual mean P_{MAX}–P_{MIN} difference in precipitation (mm/day) for (A) zonal mean, separated by ocean (blue), land (red), and total (black); (B) spatial pattern in the tropics . 30

2.5 Zonal mean precipitation (mm/day) over the Atlantic (40–20°W) for (A) P_{MAX}; (B) P_{MIN}; (C) P_{MAX}–P_{MIN}. The black line indicates the position of the ITCZ as measured by the location of zero meridional wind speed for P_{MAX} (solid) and P_{MIN} (dashed). Insets on the right show the corresponding annual mean. Contours in (C) show P_{MAX}–P_{MIN} TOA insolation, as in Fig. 2.2B 32

2.6 Schematic illustrating the main processes affecting the position and intensity of the Atlantic ITCZ for JJA (top) and DJF (bottom), P_{MAX}–P_{MIN}. Changes in precipitation are indicated by green (wetter) and brown (drier) shading; contours indicate changes in surface shortwave radiation, with darker colors representing larger changes; red (left-slanted) and blue (right-slanted) hatching show surface warming and cooling respectively; black arrows indicate changes in surface winds, while grey arrows show changes in vertical circulation 35

2.7 JJA P_{MAX}–P_{MIN} change in (A) 2m temperature (°C; colors) and precipitation (contour levels 2 mm/day); and (B) cloud fraction (colors) and surface winds (m/s; vectors) . . . 36

2.8 Zonal mean SST (°C) over the Atlantic (40–20°W) for (A) P_{MAX}; (B) P_{MIN}; (C) P_{MAX}–P_{MIN}. The black line indicates the position of the ITCZ as measured by the location of zero meridional wind speed for P_{MAX} (solid) and P_{MIN} (dashed). Insets on the right show the corresponding annual mean. Contours in (C) show P_{MAX}–P_{MIN} TOA insolation, as in Fig. 2.2B 37

2.9 Zonal mean contributions to the P_{MAX}–P_{MIN} change in heating rate (°C/month) of the Atlantic Ocean (40–20°W) mixed layer (A), from (B) a change in shortwave radiation; (C) a change in longwave radiation; (D) a change in latent heat flux (negative plotted); (E) a change in sensible heat flux (negative plotted); (F) changes in advection and mixing; (G) changes in mixed layer depth; see Eq. (2.9). Insets on the right show the corresponding annual mean; green lines indicate the March (solid) and September (dashed) months for reference. Contours in (D) show P_{MAX}–P_{MIN} wind speed 39

2.10 JJA P_{MAX}–P_{MIN} change in vertical velocity (Pa/s; colors) and potential temperature anomalies with respect to the vertical average (contour levels 0.5°C) for various latitude bands across the tropical Atlantic: (A) 15°N–25°N; (B) 5°N–15°N; (C) 5°S–5°N; (D) 15°S–5°S; (E) 25°S–15°S. Black bars indicate land 41

2.11 DJF P_{MAX}–P_{MIN} change in (A) 2m temperature (°C; colors) and precipitation (contour levels 2 mm/day); and (B) cloud fraction (colors) and surface winds (m/s; vectors) . . . 44

2.12 DJF P_{MAX}–P_{MIN} change in vertical velocity (Pa/s; colors) and potential temperature anomalies with respect to the vertical average (contour levels 0.5°C) for various latitude bands across the tropical Atlantic: (A) 15°N–25°N; (B) 5°N–15°N; (C) 5°S–5°N; (D) 15°S–5°S; (E) 25°S–15°S. Black bars indicate land 46

2.13 Eccentricity rectification of annual mean precipitation (mm/day; colors) and surface winds (m/s; vectors); see Eq. (2.10) 52

3.1 Climate drivers over the last 400 ka – (A) precession ($e\sin(\omega)$, where e is eccentricity, $\omega = \pi + \widetilde{\omega}$ and $\widetilde{\omega}$ is the angle between the vernal equinox and perihelion (Paillard, 2001); grey) and obliquity (red) (Laskar et al., 2004); (B) monthly insolation anomalies (colors, contours ranging from ±65 W m^{-2}), annual mean insolation (black) and summer length (days with insolation >250 W m^{-2} (Huybers & Denton, 2008); purple) at 65 °S as a result of the orbital forcing in (A) (Laskar et al., 2004); (C) atmospheric CO_2 concentration (grey; Lüthi et al., 2008) and global sea level (m) scaled from Lisiecki & Raymo (2005) according to Eq. 3.4. 62

3.2 Schematic illustrating the modeling setup as described in Sect. 3.2. 65

3.3 Climate forcing on the ice model grid – (left) Present-day climate conditions (Locarnini et al., 2010, Le Brocq et al., 2010), (second from left) LOVECLIM bias with respect to present-day climate, (third from left) first EOF and (right) first PC1 in LOVECLIM for (top) annual mean atmospheric temperature, (middle) annual mean accumulation (observed) and precipitation (LOVECLIM) and (bottom) annual mean ocean temperature at 400 m depth. For annual mean temperature the LOVECLIM temperatures were first adjusted to observed elevations (Le Brocq et al., 2010) using a lapse-rate correction of 0.008 °C m^{-1}. The atmospheric and ocean temperature biases are plotted as LOVECLIM–observed, while the precipitation bias is plotted as LOVECLIM/observed. In addition, (J) shows a composite of reconstructed temperature anomalies from ice cores (°C, orange; locations indicated by black dots in (G); Parrenin et al., 2013), (K) shows a composite of reconstructed accumulation anomalies from ice cores (σ, green; locations indicated by black dots in (H); Steig et al., 2000, Bazin et al., 2013, Vallelonga et al., 2013) and (L) shows reconstructed SST anomalies at 80 °W, 54 °S (°C, blue; Ho et al., 2012). Percentages in (J)-(L) indicate percent variance explained by the first principal component. 68

3.4 Ice sheet evolution over the last 400 ka in the various experiments listed in Table 3.1 – (left) grounded ice sheet volume in m SLE; (right) floating ice sheet volume in km^3; for (top) 'ocn' (blue), 'atm' (green), 'sl' (orange) and 'full' (black); (middle) 'atm+ocn' (blue), 'sl+ocn' (green), 'sl+atm' (orange) and 'full' (black); and (bottom) 'param' (green), 'cliff+hydro' (orange) and 'full' (black). 73

3.5 Dominant spatial pattern (first EOF) of ice sheet thickness variability (m) and minimum (green), maximum (blue) and present-day (black) grounding line extent for (A) 'full', minimum at 331 ka, maximum at 18 ka; (B) 'cliff+hydro', minimum at 125 ka, maximum at 18 ka; (C) 'sl', minimum at 121 ka, maximum at 18 ka; (D) 'atm', minimum at 331 ka, maximum at 350 ka; (E) 'ocn', minimum at 7 ka, maximum at 156 ka; (F) 'sl+atm', minimum at 331 ka, maximum at 20 ka; (G) 'sl+ocn', minimum at 122 ka, maximum at 140 ka; (H) 'atm+ocn', minimum at 330 ka, maximum at 354 ka. 75

3.6 Grounded ice volume (km^3) vs. sea level forcing (m) for (top) 'sl' experiment; (bottom) 'full' experiment; in (left) Ross sector; and (right) Weddell sector. 77

3.7 Ice sheet averaged mass balance terms (m y^{-1}) for experiments 'ocn' (blue), 'atm' (green), 'sl' (orange) and 'full' (black) – (A) accumulation, (B) surface melt, (C) oceanic melt and (D) calving. 79

3.8 Ice sheet averaged mass balance terms (m y^{-1}) for experiments 'atm+ocn' (blue), 'sl+ocn' (green), 'sl+atm' (orange) and 'full' (black) – (A) accumulation, (B) surface melt, (C) oceanic melt and (D) calving. 82

3.9 Total ice loss as a result of calving over the period 133-127 ka (km; shading) and grounding line position at 2 ka intervals (lines) for (A) 'full' simulation, and (B) 'cliff+hydro' simulation. 85

4.1 Southern Hemisphere climate response to Late Quaternary forcing – (A) daily insolation anomalies at 65 °S as a result of orbital forcing (Laskar et al., 2004) (shading; colors range from -65 to +65 W m^{-2}) and CO_2 concentrations (Lüthi et al., 2008) (purple) over the last 800 ka; (B) normalized PC1 of modeled annual mean atmospheric temperatures (black), normalized PC1 of reconstructed atmospheric temperatures at five ice core locations (Parrenin et al., 2004, EPICA Community Members, 2006, Jouzel et al., 2007, Kawamura et al., 2007, Stenni et al., 2011, Uemura et al., 2012) (dark orange) and normalized composite of Antarctic temperature reconstructions (Parrenin et al., 2013) (light orange); (C) EOF1 of modeled annual mean atmospheric temperatures (shading) and reconstructed atmospheric temperatures at five ice core locations (Parrenin et al., 2004, EPICA Community Members, 2006, Jouzel et al., 2007, Kawamura et al., 2007, Stenni et al., 2011, Uemura et al., 2012) (dots); (D) normalized PC1 of modeled annual mean precipitation (black), normalized PC1 of reconstructed accumulation at five ice core locations (Steig et al., 2000, Bazin et al., 2013, Vallelonga et al., 2013) (dark green) and normalized composite of Antarctic accumulation reconstructions (Steig et al., 2000, Bazin et al., 2013, Vallelonga et al., 2013) (light green); (E) EOF1 of modeled annual mean precipitation (shading) and reconstructed accumulation at five ice core locations (Steig et al., 2000, Bazin et al., 2013, Vallelonga et al., 2013) (dots); (F) normalized PC1 of modeled 400 m ocean temperatures (black), composite of modeled sea surface temperature anomalies (light blue) and composite of reconstructed sea surface temperature amomalies (dark blue) at four locations (Nürnberg & Groeneveld, 2006, Cortese et al., 2007, Martínez-Garcia et al., 2009, Ho et al., 2012); (G) EOF1 of modeled 400 m ocean temperatures (shading) and locations of sea surface temperature reconstructions in (F) (black dots). 94

4.2 Evolution of the Antarctic ice sheet over the last eight glacial cycles – (A) normalized PC1 of ice sheet height (black) and ice sheet volume in meters sea level equivalent (orange); (B) EOF1 of modeled ice sheet height (shading), present-day (black), minimum (blue; 330 ka) and maximum (green; 20 ka) grounding line extent; (C) ice sheet integrated mass balance terms (shading; accumulation in blue, oceanic melt in grey, calving in green, residual ablation (see Methods) in purple) and net mass balance (black) in 10^3 Gt y^{-1}(10^3 Gt $y^{-1}\sim$ 0.03 Sv) and ice sheet area ranging from 14.2 to 17.5×10^6 km^2 (grey line); (D) same as (C), zoomed in on Termination I. 97

4.3 Climatic drivers of Antarctic mass balance terms – (A) grounded ice sheet area (black) and sea level forcing from $\delta^{18}O$ (light orange) (Lisiecki & Raymo, 2005); (B) 50 y mean ice sheet averaged calving rate; (C) normalized PC1 of modeled annual mean atmospheric temperatures (black) and 70 °S summer length (light green); (D) ice sheet averaged PDDs (black) and 50 y mean ice sheet averaged residual ablation (green; see Methods); (E) accumulation rate averaged over time-evolving ice sheet area (annual mean; dark purple) and present-day ice sheet area (1000-y mean; light purple); (F) zonally averaged 60 °S 400 m ocean temperatures; (G) average ocean temperatures underneath the ice shelves (black) and 50 y mean ice sheet averaged oceanic melt rate (blue). Terminations I-VIII are indicated by grey shading. 100

5.1 Eccentricity rectification of global carbon cycle – (left) carbon fixation from photosynthesis in surface ocean (gC m^{-2} y^{-1}); (right) deep-sea (2500–4000 m) $\delta^{13}C$ (permil; where $\delta^{13}C = -1.1 \times PO_4 + 2.9$ (Broecker & Maier-Reimer, 1992)). 112

A.1 JJA P_{MAX}–P_{MIN} change in precipitation (a); contributions to this change from changes in (b) evaporation; (c) winds (δDYN in Eq. (A.2)), (d) specific humidity (δTH in Eq. (A.2)), (e) divergence (δDYN_{DIV} in Eq. (A.3)) and (f) advection (δDYN_{ADV} in Eq. (A.3)); and (g) the difference between diagnosed and modeled changes in net precipitation 116

A.2 DJF P_{MAX}–P_{MIN} change in precipitation (a); contributions to this change from changes in (b) evaporation; (c) winds (δDYN in Eq. (A.2)), (d) specific humidity (δTH in Eq. (A.2)), (e) divergence (δDYN_{DIV} in Eq. (A.3)) and (f) advection (δDYN_{ADV} in Eq. (A.3)); and (g) the difference between diagnosed and modeled changes in net precipitation 118

B.1 Ice sheet integrated mass balance terms (shading; accumulation in blue, oceanic melt in grey, calving in green, residual ablation (see Methods) in purple) and net mass balance (black) in 10^3 Gt y^{-1} (10^3 Gt y^{-1} ~0.03 Sv) and ice sheet area (grey line) during (A) Termination VII, (B) Termination V, (C) Termination IV, (D) Termination III, (E) Termination II and (F) Termination I. Mass balance terms are plotted as 10-year averages. 122

B.2 Anomalies of ice sheet averaged mass balance terms with respect to the long-term mean (accumulation in blue, oceanic melt in grey, calving in green, residual ablation (see Methods) in purple) and net mass balance (black) in m y^{-1}(A) Termination VII, (B) Termination V, (C) Termination IV, (D) Termination III, (E) Termination II and (F) Termination I. Mass balance terms are plotted as 50-year averages. 123

CHAPTER 1

Introduction

1.1 Earth's climate history in review

The response of earth's climate system to external forcing is not constant in time. Even though its periodic external drivers have remained stable over the last ~50 million years (Ma) (Laskar et al., 2004), our planet has seen a widely varying array of climate variability over this period. This is illustrated in Fig. 1.1, which shows the evolution of estimated global mean temperatures through the last 65 Ma, using deep sea oxygen isotopes ($\delta^{18}O$) as a proxy. Since the beginning of the Cenozoic Era 66 Ma, the planet has been gradually cooling from a so-called 'Greenhouse climate' – accompanied by atmospheric CO_2 concentrations upwards of 1,500 ppmv (Pagani et al., 2005) – to the recent 'Icehouse climate' (Zachos et al., 2001), in response to longterm (10^5–10^7 year) changes in climatic boundary conditions, such as continental configuration, oceanic gateways, volcanic activity and atmospheric greenhouse gas concentrations. The overall cooling trend is interrupted by rapid transitions and 'brief' spikes, such as the much-studied Paleocene-Eocene Thermal Maximum (PETM) 55 Ma (e.g., Kennett & Stott, 1991, Sluijs et al., 2006).

The polar ice caps as we know them today, did not exist throughout the entire Cenozoic. Amidst

the early Cenozoic warmth, planet earth was entirely ice free, until greenhouse gas concentrations dropped sufficiently to allow for glaciation of the isolated Antarctic continent (DeConto & Pollard, 2003). The boundary between the Eocene and Oligocene Periods, at roughly 33.7 Ma, is marked by a sharp drop in benthic $\delta^{18}O$ levels (Fig. 1.1) that signifies the definitive establishment of the Antarctic ice sheet (e.g., Coxall & Pearson, 2007). Glaciation in the Northern Hemisphere did not occur until approximately 10 Ma (Zachos et al., 2001) and initially only occurred at a small scale (Maslin et al., 1998).

The Pliocene Epoch, from 5.3–2.6 Ma, is the most recent period in earth's climate history when atmospheric CO_2 concentrations were similar to or slightly higher than what they are today, and thus serves as an 'analog' for contemporary climate change (Haywood et al., 2013, Masson-Delmotte et al., 2013). As can be seen in Fig. 1.1, the amplitude of benthic $\delta^{18}O$ variations gradually increases towards the end of the Pliocene. This larger amplitude indicates both an increase in temperature variability and growing oscillations in global ice volume (Zachos et al., 2001). The final closure of the Panama Isthmus around 3 Ma, and subsequent reorganization of the meridional overturning circulation, ultimately allowed for northern polar ice sheets to grow to a size that substantially increased earth's sensitivity to external forcing (Haug & Tiedemann, 1998, Zachos et al., 2001, Bartoli et al., 2005, Lisiecki & Raymo, 2005). The resulting periodic Northern Hemisphere glaciations are what characterizes the current geologic Period – the Quaternary – which will be the focus of this dissertation.

1.1.1 The Quaternary

The Quaternary is the period from 2.6 Ma to present. It is split into the Pleistocene Epoch, which lasted until 11,700 years ago (11.7 ka), and the Holocene, an epoch of relative climatic stability that allowed for the establishment and growth of human civilization. During the Quaternary, earth's climate cycled between periods of relative warmth, so-called 'interglacials', and colder periods called 'glacials'. The amplitude of these oscillations increased progressively throughout the Quaternary, and

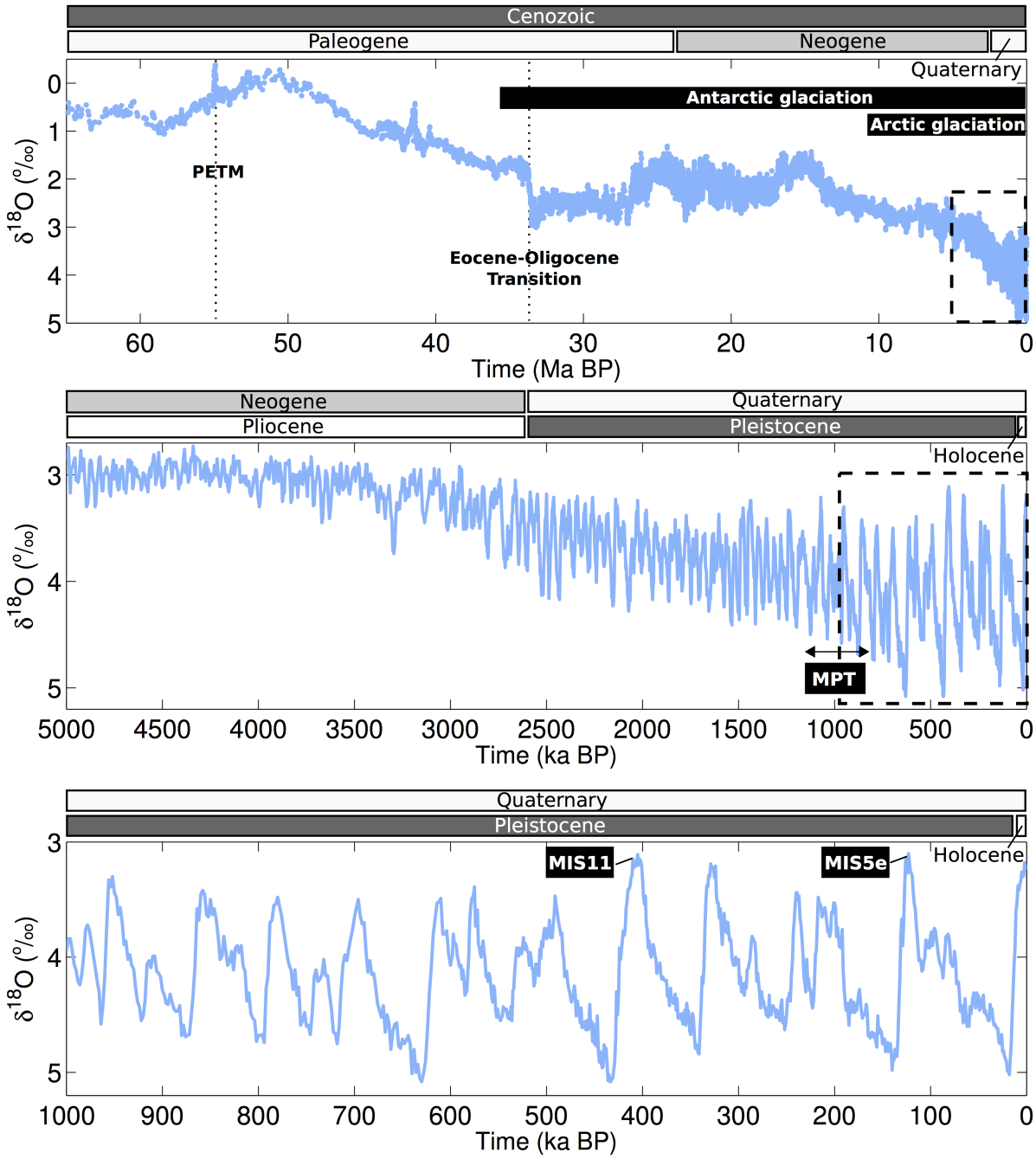

Figure 1.1: Earth's climate history throughout the Cenozoic, as indicated by the benthic $\delta^{18}O$ record. Generally, high $\delta^{18}O$ values indicate low temperatures, and vice versa. The top figure shows $\delta^{18}O$ values collected by Zachos et al. (2001); the bottom two figures show the Lisiecki & Raymo (2005) record.

while initially their period was 41 ka, since approximately 1 Ma glacial cycles have occurred with a period in the range of 80–120 ka (Fig. 1.1) (Lisiecki & Raymo, 2005). This shift from a 41 ka regime to a ~100 ka regime is referred to as the Mid-Pleistocene Transition (MPT), and has been attributed to changes in the insolation forcing around that time (Schulz & Zeebe, 2006), changing subglacial bedrock conditions (Clark et al., 2006) or threshold behavior in the climate system (Paillard, 2001). This dissertation will exclusively study the 100 ka regime of the Late Quaternary, here loosely defined as the period from 800 ka until present.

The Last Glacial Maximum (LGM) at ~20 ka, is the most recent glacial period and hence the most studied and documented. Global mean temperatures during the LGM were approximately 4 °C lower than they were before the onset of the Industrial Revolution ('pre-industrial') (Annan & Hargreaves, 2013). Massive ice sheets covered much of northern America and Eurasia (e.g., Peltier, 2004), and also the Antarctic ice sheet was substantially larger than it is presently (Bentley et al., 2014). As a result, global mean sea level was >120 m lower than today (Waelbroeck et al., 2002). Global cooling during glacial periods led to generally arid conditions (Kohfeld & Harrison, 2001), and significant differences exist between glacial and pre-industrial atmospheric circulation. For instance, the elevated albedo and orography of the Northern Hemisphere ice sheets substantially altered the path of the mid-latitude storm tracks (Roe & Lindzen, 2001, Justino et al., 2005), while pushing the Atlantic Intertropical Convergence Zone (ITCZ) south (Chiang & Bitz, 2005, Arbuszewski et al., 2013). Due to large-scale reconfigurations in earth's biosphere and the global ocean, particularly the Southern Ocean, atmospheric greenhouse gas concentrations were reduced during cold periods (Petit et al., 1999, Sigman et al., 2010). Atmospheric CO_2 concentrations dropped from ~280 ppmv during interglacials to ~180 ppmv during glacials (Fig. 1.2D) (Lüthi et al., 2008).

While these characteristics generally describe periods of maximum glaciation during the Late Quaternary, glacial climates are by no means stable. Reconstructions of past climates at both high and low latitudes have shown that glacial cycles are punctuated by superimposed climate variability on millennial scales. So-called Heinrich (Heinrich, 1988) and Dansgaard-Oeschger (Dansgaard et al., 1984) events – layers of ice-rafted debris in the North Atlantic – are manifestations of sudden collapses

of Northern Hemisphere ice sheets that led to reorganization of the global overturning circulation, with cooling in the northern high latitudes and warming over Antarctica (e.g., Blunier & Brook, 2001). These temporary climate swings had global impacts, as evidenced for example by rapid shifts in the Atlantic ITCZ on millennial time scales (Deplazes et al., 2013).

By contrast, interglacial climates are much more stable (North Greenland Ice Core Project Members, 2004), although marked differences still exist between the various interglacials. For instance, Marine Isotope Stage (MIS) 5e (130 ka) and 11 (410 ka) (Fig. 1.1) are thought to have been warmer than pre-industrial, with global sea level elevated by 3–9 m (Dutton et al., 2015). The differences between interglacial climates result from the fact that different combinations of Late Quaternary climate drivers (as discussed below) make up the boundary conditions of the various interglacials (Yin & Berger, 2010).

1.1.2 Drivers of Quaternary climate variability

What drives the climate cycles of the Late Quaternary depends on how the boundaries of the system of interest are defined. From an earth system point of view, 'external forcing' only includes those forcings that originate outside of our planet. On the other hand, certain forcings and feedbacks that are internal to the earth system – such as volcanic eruptions and the glacial changes in atmospheric greenhouse gases described above – can be treated as external when studying solely the climate system. Of course, atmospheric scientists and oceanographers might take this one step further, by regarding changes in respectively sea surface temperatures and surface wind patterns as boundary conditions to their system. Throughout this dissertation, the system under consideration consists of coupled atmosphere, ocean, sea ice and terrestrial vegetation components, with orbital forcing (see below), atmospheric greenhouse gases and Northern Hemisphere ice sheet conditions all serving as external drivers[1].

[1] The system will be studied, however, with two different climate models. See Sect. 2.2 and 3.2 for more details about the modeling setup.

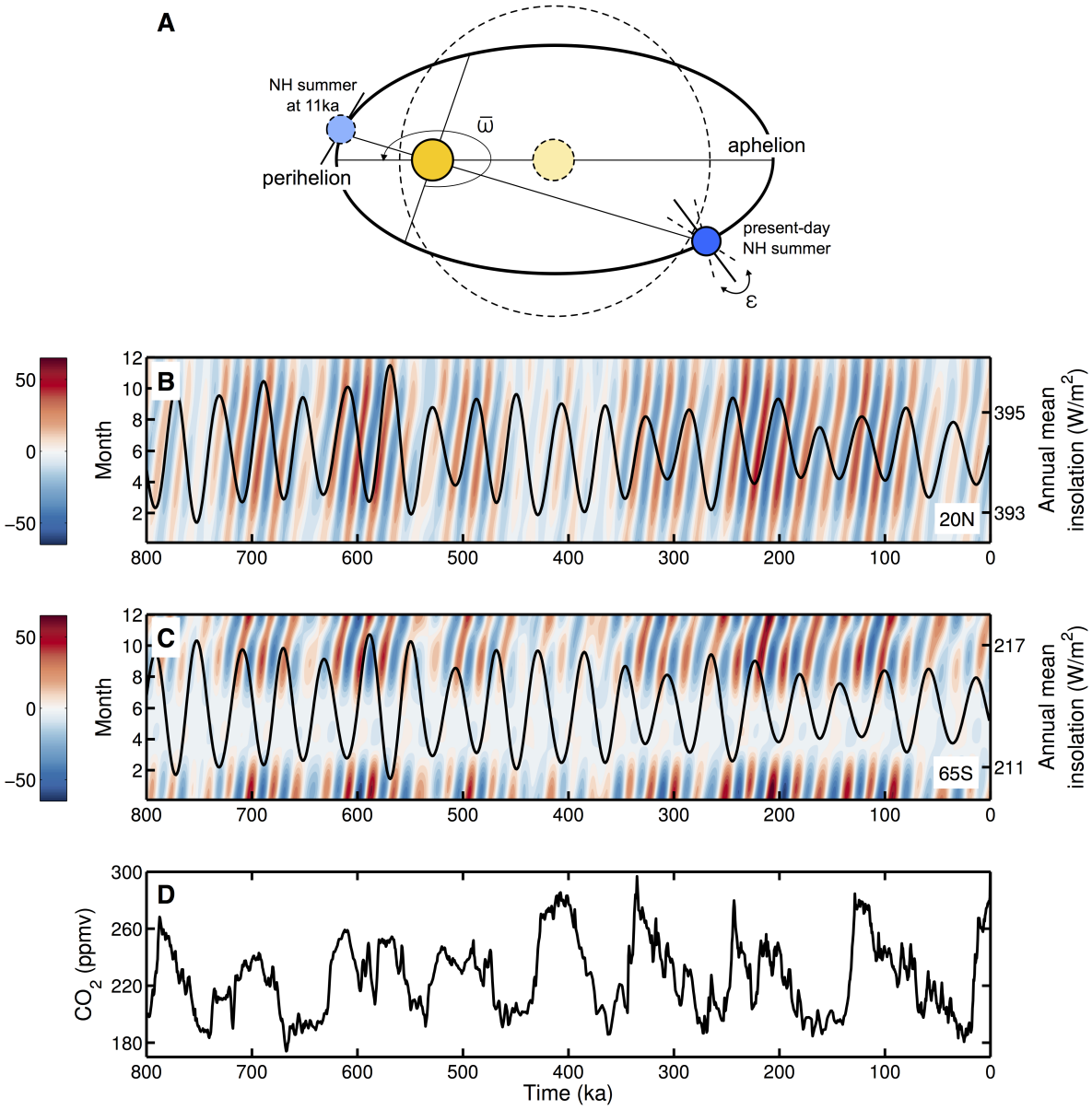

Figure 1.2: Drivers of Late Quaternary climate variability – (A) illustration of orbital parameters: variations in earth's tilt – obliquity (ϵ), variations in how elliptical earth's orbit is – eccentricity (solid and dashed orbit and sun), variations in timing of perihelion – precession (solid and dashed earth; measured by angle $\overline{\omega}$); (B) monthly insolation anomalies (shading) and annual mean insolation (black) in W m^{-2} at 20 °N; (C) monthly insolation anomalies (shading) and annual mean insolation (black) in W m^{-2} at 65 °S; (D) atmospheric CO_2 concentrations from the EPICA Dome C ice core (Lüthi et al., 2008).

Climate variability on time scales of 10^4–10^5 years ultimately derives from astronomical forcing (Milankovitch, 1941, Imbrie & Imbrie, 1980): cyclic changes in earth's orbit around the sun and its axial tilt, caused by the gravitational interaction between the earth, sun, moon, and the other planets in our solar system (Berger, 1978, Laskar et al., 2004). This astronomical forcing can be described by three parameters – obliquity, eccentricity and precession (illustrated in Fig. 1.2A) – that each affect the seasonal and latitudinal distribution of incoming solar radiation (insolation). Obliquity (ε in Fig. 1.2A) is the tilt of earth's axis with respect to the orbital plane. It varies between 22° and 24.5° with a dominant period of 40,978 year (41 ka; the period of glacial cycles before the MPT (Fig. 1.1); Berger, 1978, Laskar et al., 2004). At a given latitude, obliquity affects the amplitude of the seasonal cycle as well as annual mean insolation. This effect is asynchronous between high and low latitudes: when obliquity is high, annual mean insolation increases symmetrically at high latitudes and decreases at low latitudes. This can be seen in Figs. 1.2B & C, which shows seasonal and annual mean insolation changes at 20 °N and 60 °S. Annual mean insolation clearly oscillates with a 41 ka period, and is anti-phased between the low (Fig. 1.2B) and high (Fig. 1.2C) latitude location. Global annual mean insolation does not change with obliquity.

The eccentricity e indicates how elliptic the orbit of the earth around the sun is. It is defined as $e = c/a$, where a is the semi-major axis of earth's orbit, and c is the distance between the position of the sun (the focus) and the center of the ellipse (Fig. 1.2A; Paillard, 2001). The fact that earth's orbit is not entirely circular is the reason why Northern and Southern Hemisphere seasons differ in length and duration. The point on earth's orbit closest to the sun is called 'perihelion', while the location furthest away is referred to as 'aphelion'. When earth is closer to the sun, it receives more insolation (proportional to (sun-earth distance)$^{-2}$), but it also travels faster (as described by Kepler's second law). The season in perihelion (Southern Hemisphere summer for present-day precession, see below) is thus stronger but shorter than the season in aphelion (presently Northern Hemisphere summer). Eccentricity values vary between 0.0002 and 0.067 at the three dominant periods of 405,091 year, 94,932 year and 123,945 year (Berger, 1978, Laskar et al., 2004), where the former is usually referred to as the '400 ka' period of eccentricity and the latter two are commonly grouped together as '100 ka'.

The gravitational pull on the earth causes earth's axis to 'wobble', leading to a clockwise movement of the equinoxes along the earth's orbit that is called the precession of the equinoxes. This precession has a quasi-period of ~25.7 ka relative to the stars. For climatic purposes only the motion of the equinoxes with respect to perihelion is of interest. This is the climatic precession, measured by the (counter-clockwise) angle $\overline{\omega}$ between the vernal equinox and perihelion (Fig. 1.2A). In paleoclimate studies it is customary to reference precession as $\omega = \overline{\omega} + \pi$ (maximum precession when winter solstice is near perihelion; Berger, 1978, Paillard, 2001). The dominant periods of climatic precession are 23 ka and 19 ka.

In contrast to obliquity, eccentricity only has a very small effect on annual mean insolation, and precession has none. Precession merely redistributes the insolation across the year, i.e. it changes the amplitude of the seasonal cycle and the length of seasons. This is illustrated in Figs. 1.2B & C: the seasonal distribution of insolation at both high and low latitudes varies with a periodicity of ~20 ka, but there is no 20 ka variability in annual mean insolation. Also note in Fig. 1.2 that the effects of precession are anti-phased between hemispheres: when the annual cycle is strong in the Northern Hemisphere it is weak in the Southern Hemisphere. The amplitude of the precessional cycle is modulated by the eccentricity cycle, as there will be no climatic effect associated with precession when earth's orbit is perfectly circular (Fig. 1.2A). For this reason, climatic precession is usually expressed as $e\sin(\omega)$. The eccentricity modulation of precession can be seen in Figs. 1.2B & C as well: the amplitude of precessional variations in seasonal cycle strength is much higher at e.g., 200 ka than it is at 400 ka.

As discussed above, the glacial cycles of the Quaternary are associated with large variations in atmospheric greenhouse gas concentrations, most prominently carbon dioxide. Due to their ability to absorb longwave radiation, greenhouse gases exert a strong influence on earth's temperature. Atmospheric CO_2 is well-mixed in the atmosphere over time-scales of more than a year, so CO_2 changes affect climate globally. CO_2 concentrations over the last 1 Ma (Fig. 1.2D) have varied with global ice volume and temperature (Fig. 1.1). While the exact reasons for glacial-interglacial CO_2 variability

still remain elusive (Sigman et al., 2010), it is clear that they provide an essential positive feedback on the evolution of Quaternary climate (Shackleton, 2000, Shakun et al., 2012).

Other climatic drivers, such as atmospheric dust loading and ocean bathymetry (water depth and shelf exposure), also vary on glacial timescales, and are thought to provide substantial feedbacks on climate evolution (e.g., Bar-Or et al., 2008, DiNezio et al., 2011). However, because these drivers are either poorly constrained or not well represented in climate models, they will not be considered in this dissertation.

1.2 Rectification in the climate system

The parameters describing the astronomical forcing of earth's climate system are stable over time scales of tens of millions of years (Laskar et al., 2004), yet the brief climate history provided in Sect. 1.1 demonstrates that the system response to this forcing evolves through time. The occurrence of abrupt climate transitions (e.g., the PETM and rapid glacial-interglacial transitions ('deglaciations')), the increasing amplitude of climate oscillations on orbital (10^4–10^5 years) time scales throughout the Cenozoic, and the Pleistocene dominance of variability at a frequency (~100 ka) that does not correspond to a dominant astronomical forcing, are all indicators of the strongly nonlinear character of the climate system (Fig. 1.1; Rial et al., 2004, Lisiecki & Raymo, 2007). Evidently, the evolution of planetary boundary conditions (such as continental configuration and atmospheric composition) due to tectonic processes on time scales of 10^5–10^7 years, modulates the response of the climate system to external forcing (Short et al., 1991, Zachos et al., 2001). At the same time, the system sensitivity is further modulated by the climate response to the forcing, for instance through the glacial-interglacial change in atmospheric CO_2 concentrations or the albedo changes associated with massive ice sheet expansion (Abe-Ouchi et al., 2007). This dissertation examines case studies of two manifestations of nonlinear rectification mechanisms in the climate system: rectification of precessional forcing and 100 ka variability.

1.2.1 The precessional cycle

Despite the fact that no changes in annual mean insolation are associated with the precessional cycle (Fig. 1.2B, C), many climate records from many proxies, locations and times in the past show variability at precessional periods. The precessional cycle has the strongest influence on tropical climate (Clement et al., 2004), with a particularly notable influence on the monsoon systems. Variations in the African, Indian, East-Asian and Australian monsoon during the Pleistocene are recorded by a wide variety of proxies (Liu & Shi, 2009, Clemens et al., 2010), such as $\delta^{18}O$ in speleothems of Chinese (e.g. Wang et al., 2008, Cheng et al., 2009) and Brazilian (Cruz et al., 2005) caves, stable isotopes in marine sediment cores (Denison et al., 2005, Ziegler et al., 2010), an African humidity index (Tjallingii et al., 2008), iron input (Bozzano et al., 2002), primary productivity and length of season proxies (Beaufort et al., 2010), pollen records (Prell & Kutzbach, 1987) and the cyclic occurrence of sapropel layers in Mediterranean sediments (Hilgen, 1991, Lourens et al., 1996). Precessional variations in the EPICA Dome C (Antarctica) ice core methane concentrations over the last 800 ka are indicative of monsoon-related vegetation changes (Loulergue et al., 2008).

Imprints of precessional variability are also found in high-latitude climate records. Analyses of Antarctic ice cores show precessional energy in Antarctic temperature, greenhouse gas concentrations and atmospheric $\delta^{18}O$ (Petit et al., 1999, Stuiver & Grootes, 2000, North Greenland Ice Core Project Members, 2004, Jouzel et al., 2007). Records of ice-rafted debris (IRD) and benthic $\delta^{13}C$ and reconstructions of sea-surface temperature (SST) and salinity are thought to show precessionally paced ice sheet instabilities and meltwater pulses in both the Northern (Curry & Oppo, 1997, Chapman & Shackleton, 1999, Oppo et al., 2001, Knies & Vogt, 2003, Schmidt et al., 2004, Oppo et al., 2006, Knies et al., 2007, Timmermann et al., 2010) and Southern (Scherer et al., 2008) hemisphere. In the deep sea record, benthic $\delta^{18}O$ varies in phase across the world's oceans on precessional timescales (Lisiecki & Raymo, 2005, 2007).

As discussed above, the amplitude of the precessional cycle is modulated by eccentricity. The annual mean insolation forcing associated with the eccentricity cycle is small, yet numerous paleo-

climate proxies display substantial variability at the ~100 ka and 400 ka eccentricity periods. Some studies have attributed the ~100 ka periodicity of the post-MPT glacial cycles to a climate system amplification of the eccentricity forcing, though current understanding of glacial cycle dynamics revolves around the superposition of the obliquity cycle and eccentricity-modulated precession (Imbrie & Imbrie, 1980, Imbrie et al., 1993, Paillard, 1998, Schulz & Zeebe, 2006, Ganopolski & Calov, 2011, Heinemann et al., 2014). Statistical detection of the stronger but longer 400 ka period is limited by the length of paleorecords, but has been achieved for benthic carbon isotope (δ^{13}C) records from the Pliocene (Bickert et al., 1993, Tiedemann et al., 1994, Mix et al., 1995, Clemens & Tiedemann, 1997, Tian et al., 2002, Venz & Hodell, 2002, Wang et al., 2003, 2004a, 2010). ~400 ka cycles were also recorded in the Cretaceous (145–66 Ma), when there where no large ice sheets, suggesting that the processes driving the cycles are not directly related to fluctuations in ice volume (Russon et al., 2010). Marked changes happened to the 400 ka cycle during the Pleistocene, when their periodicity shifted to ~500 ka, obscuring the phase relationship with the eccentricity cycle (Wang et al., 2004a, 2010). 400 ka cycles are often used to develop common time scales for long paleorecords, adding impetus to understanding their origin and global phasing.

The presence of precessional variability in climate records indicates that nonlinear mechanisms rectify the zero annual mean precessional forcing into a non-zero annual mean climate response. Similarly, recorded eccentricity variability in the absence of strong annual mean eccentricity forcing suggests that the amplitude modulation of precession by eccentricity results in a nonlinear transfer of energy from the high-frequency precessional cycle to the low-frequency eccentricity cycle (Short et al., 1991, Herbert, 1997, Paillard, 2001, Huybers & Wunsch, 2003, Rial et al., 2004, Merlis et al., 2013). Huybers & Wunsch (2003) illustrate the concept of nonlinear rectification of the precessional cycle using several theoretical functions. A very simple rectification would be if the climate system

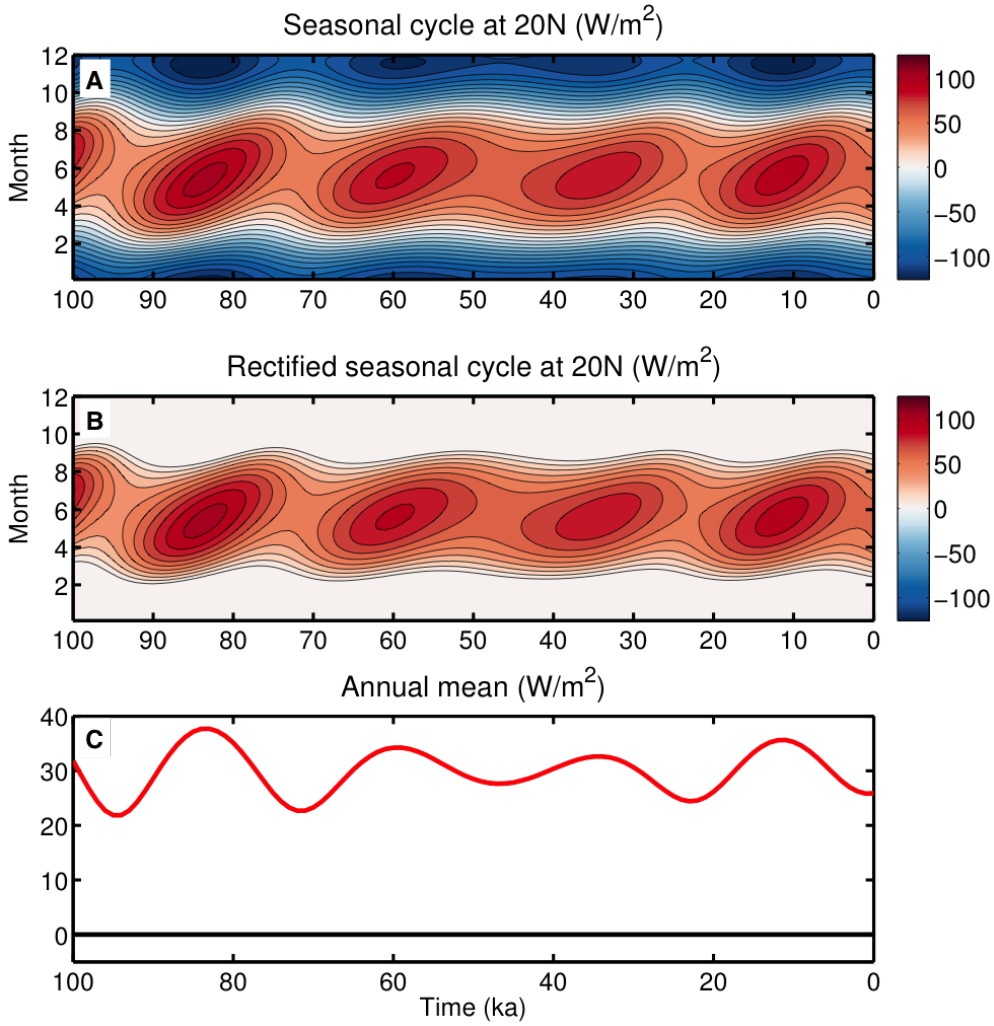

Figure 1.3: Theoretical example of nonlinear rectification – (A) seasonal insolation forcing (Q_{seas}) over the past 100 ka (Laskar et al., 2004); (B) rectified seasonal insolation forcing (Q_{rect}) according to Eq. 1.1; (C) annual mean of seasonal insolation forcing in (A) (black) and rectified seasonal insolation forcing in (B) (red).

only responds to seasonal insolation forcing Q_{seas} above a certain threshold, e.g. zero:

$$Q_{rect} = \begin{cases} Q_{seas}, & Q_{seas} \geq 0 \\ 0, & \text{otherwise} \end{cases} \tag{1.1}$$

Figure 1.3A shows the seasonal insolation forcing over the past 100 ka, while Fig. 1.3B shows what

this forcing would look like if rectified by Eq. 1.1. As can be seen in Fig. 1.3C, the annual mean associated with the initial seasonal forcing is zero, but the rectified annual mean response is several tens of W m^{-2} and modulated by the eccentricity cycle. This dissertation explores some of the nonlinear mechanisms that create rectification functions such as Eq. 1.1.

1.2.2 100 ka variability

The ~100 ka periodicity of Late Quaternary climate cycles, and in particular the role of carbon cycle feedbacks therein, remain one of the largest mysteries in our understanding of (paleo-)climate dynamics. Earlier work on this problem has tried to explain the 100 ka periodicity as a strong amplification of the weak ~100 ka eccentricity period, or an internal oscillation of the climate system (Imbrie & Imbrie, 1980, Oerlemans, 1982, Imbrie et al., 1993, Gildor & Tziperman, 2001). More recently however, the initiation and termination of large scale glaciations is attributed to the superposition of obliquity and precessional forcing. The combination of high obliquity and low precession (Northern Hemisphere summer solstice in perihelion) creates conditions of high summer melt that initiate glacial terminations (Schulz & Zeebe, 2006, Ganopolski & Calov, 2011, Heinemann et al., 2014). Eccentricity only plays a role here through its modulation of the precessional cycle. In addition, the efficacy of the orbitally-driven insolation forcing is strongly modulated by the state of the climate-ice sheet system. For example, the ability of insolation changes in the Northern Hemisphere to initiate a rapid and full deglaciation depends on the size of the Northern Hemisphere ice sheets: only when the ice sheets are above a certain size do they reach down to latitudes that allow for substantial surface melt and amplifying feedbacks (Imbrie et al., 1993, Abe-Ouchi et al., 2013). Moreover, numerous modeling studies have confirmed the essential role of changes in atmospheric greenhouse gas concentrations in amplifying global temperature changes and ice sheet evolution over the course of the Quaternary glacial cycles (e.g., Abe-Ouchi et al., 2007, Ganopolski & Calov, 2011, He et al., 2013, Heinemann et al., 2014). Finally, the instabilities that give rise to climate variability on millennial time scales only seem to exist in cold glacial climates, exemplifying how long(er)-term (10^4-10^5 year) variability

modulates short(er)-term (10^3 year) variability in the earth system.

In the present-day climate system, global climate variability on interannual to multi-decadal timescales is dominated by the dynamics of the tropical ocean-atmosphere system. Yet for millennial to orbital timescales, a picture emerges where climate change globally is paced by the glacial-interglacial variability of the northern high latitudes. The interpretation of paleoclimate records thus often revolves around the question whether local climate change is a direct result of local insolation forcing, or forced by changes in Northern Hemisphere polar climate. In the case of the tropics, Clement et al. (2004) argued that the magnitude of the effect on hydroclimate of local precessional forcing is comparable to that of 100 ka glacial-interglacial forcing. In the Southern Hemisphere, reconstructions from Antarctic ice cores suggest that local climate change is in phase with Northern Hemisphere climate evolution (EPICA Community Members, 2006, Kawamura et al., 2007, Parrenin et al., 2013), causing some to propose that 'north drives south', primarily through changes in the global overturning circulation and CO_2 concentrations (Huybers, 2009, Denton et al., 2010, He et al., 2013). Additionally, the large marine margins of the Antarctic ice sheet make it sensitive to 100 ka sea level variability (Ritz et al., 2001, Huybrechts, 2002, Schoof, 2007, Pollard & DeConto, 2009). Other studies however, have attributed the apparent co-evolution of bipolar climates to hemispheric differences in sensitivity to precessional phase (Huybers & Denton, 2008, Huybers, 2009, Timmermann et al., 2009), or to seasonal biases in the climate recorder (Laepple et al., 2011).

In short, the orbitally-driven northern hemisphere glaciations of the Late Quaternary with their 100 ka periodicity, and accompanying changes in CO_2, global sea level and other earth system variables, modulate the local response of tropical and southern extratropical climate to astronomical forcing. In many cases, the magnitude and dynamics of this rectification remain to be uncovered.

1.3 Dissertation outline

The discussion in the preceding sections of the nonlinear relationship between astronomical forcing and earth's climate system sets the stage for the work presented in this dissertation. The following

chapters will explore the nonlinearities of precessional rectification and 100 ka modulation through the Late Quaternary in two parts of the climate system:

Rectification mechanisms at low latitudes Part I of this dissertation focuses on precessional variability in reconstructions of tropical hydroclimate (Sect. 1.2.1). Chapter 2 sets out to identify the nonlinear mechanisms rectifying the response of the annual mean Atlantic ITCZ to precessional forcing in a series of time slice experiments with the Community Earth System Model (CESM) 1.0.3 (Chikamoto et al., 2015). The oceanic precipitation response to precessional forcing is found to be strongly linked to the response over the neighboring continents, which is rectified by the mean seasonal cycle and (time-constant) continental configuration. Chapter 2 also discusses eccentricity rectification and the modulation of the relative roles of tropical and extra-tropical dynamics by the 100 ka periodicity of glacial-interglacial cycles.

Rectification mechanisms at high latitudes Part II of this dissertation looks at orbital forcing of high latitude climates, in particular that of the Southern Hemisphere. Chapters 3 & 4 investigate the role of Late Quaternary climate and sea level changes in driving the evolution of the Antarctic ice sheet. To this end, the Penn State University Antarctic ice sheet model (Pollard & DeConto, 2012b) was forced with time-evolving climate conditions from the Earth System Model of Intermediate Complexity (EMIC) LOVECLIM (Goosse et al., 2010). Chapter 3 shows that individual drivers of the Antarctic mass balance (atmospheric, oceanic and sea level forcing) add nonlinearly in the full ice sheet response, while Chapter 4 argues that glacial termination of the Antarctic ice sheet occurred in phase with that of the Northern Hemisphere ice sheets. Precession and its modulation by the evolution of atmospheric CO_2 play an important role in initiating terminations and synchronizing ice sheet evolution in both hemispheres.

Part I

Rectification mechanisms at low latitudes

CHAPTER 2

Mechanisms rectifying the annual mean response of tropical Atlantic rainfall to precessional forcing

Numerous reconstructions of tropical hydroclimate in the Pleistocene display substantial variability on precessional timescales. Precessionally-induced insolation variations, with a mean period of ~21,000 years, affect the strength of the seasonal cycle, but not annual mean insolation. The existence of variations in annual mean climate on precessional timescales therefore hints at the existence of nonlinear mechanisms that rectify the zero annual mean forcing into a non-zero annual mean response. The aim of this study is to identify these nonlinear rectification mechanisms. The traditional view of precessionally-forced precipitation changes is that tropical precipitation increases with summer insolation. By comparing two simulations with an earth system model (CESM1.0.3) we find that this paradigm is true for continental but not for oceanic changes in precipitation. Focusing on the Atlantic Intertropical Convergence Zone (ITCZ), we find that the continental temperature and precipitation response to precessional forcing are key rectifiers of annual mean precipitation over the ocean. A boundary layer response to temperature changes over northern Africa affects the *meridional position* of the ITCZ over the North Atlantic in boreal spring and summer, but not in fall and winter. Over the equatorial and South Atlantic, the *intensity* of precipitation is strongly impacted by diabatic forcing from the continents through an adjustment of the full troposphere. Although the top of atmosphere insolation forcing is seasonally symmetric, continental precipitation changes are largest in boreal summer, thus skewing the annual mean response. These results show that it is important to take into account the seasonality of climatic forcings, even when studying annual mean climate change.

Based on: Tigchelaar, M. & Timmermann, A. (2015) Mechanisms rectifying the annual mean response of tropical Atlantic rainfall to precessional forcing. *Climate Dynamics*. DOI: 10.1007/s00382-015-2835-3.

2.1 Introduction

Out of earth's three orbital parameters – eccentricity, obliquity, and precession – responsible for low-frequency climate variability (Milankovitch, 1941), the one with the largest expression in the tropics is precession (Berger, 1978, Laskar et al., 2004). With a period of ~21,000 years (21 ka), the precessional cycle determines at what time of year the earth is closest to the sun. It thus changes the strength of the seasonal cycle in incoming solar radiation at each latitude, and it does so anti-symmetrically across the hemispheres: When the seasonal cycle is stronger in the Northern Hemisphere ('minimum precession', similar to e.g. 11 ka) it is weaker in the Southern Hemisphere, and vice versa ('maximum precession', similar to e.g. present-day). The strength of the precessional cycle is modulated by eccentricity, which describes how elliptical earth's orbit is. When eccentricity is low – i.e. the orbit is close to circular – precession hardly influences seasonality.

Many tropical paleoclimate records display substantial precessional variability, much more so than polar records such as the EPICA and NGRIP ice cores (EPICA Community Members, 2004, North Greenland Ice Core Project Members, 2004). This recorded precessional variability can result from either a physical climate forcing, or from the seasonal bias of climate recorders (Huybers & Wunsch, 2003) as for instance shown for SST reconstructions and the production rates of coccolithophorids and planktonic foraminifera in Timmermann et al. (2014) and Antarctic temperatures and snow accumulation in Laepple et al. (2011). Figure 2.1A shows a compilation of various proxy reconstructions of tropical hydroclimate (smoothed with a 1000-year running mean) over the past 120 ka, contrasted against the precessional forcing. The records are ordered from North to South, with inferred precipitation increasing along the y-axis. All of these records contain some component of precessional variability, with maximum precipitation generally coinciding with maximum local summer insolation. Because precessional forcing of seasonal cycle strength is anti-phased between hemispheres, there is a North to South anti-symmetry in the timing of precipitation maxima. This is also illustrated in Fig. 2.1B, which for each record shows the precessional phase of the 25% highest precipitation values, scaled by amplitude. Clearly the majority of the Northern Hemisphere precipitation maxima

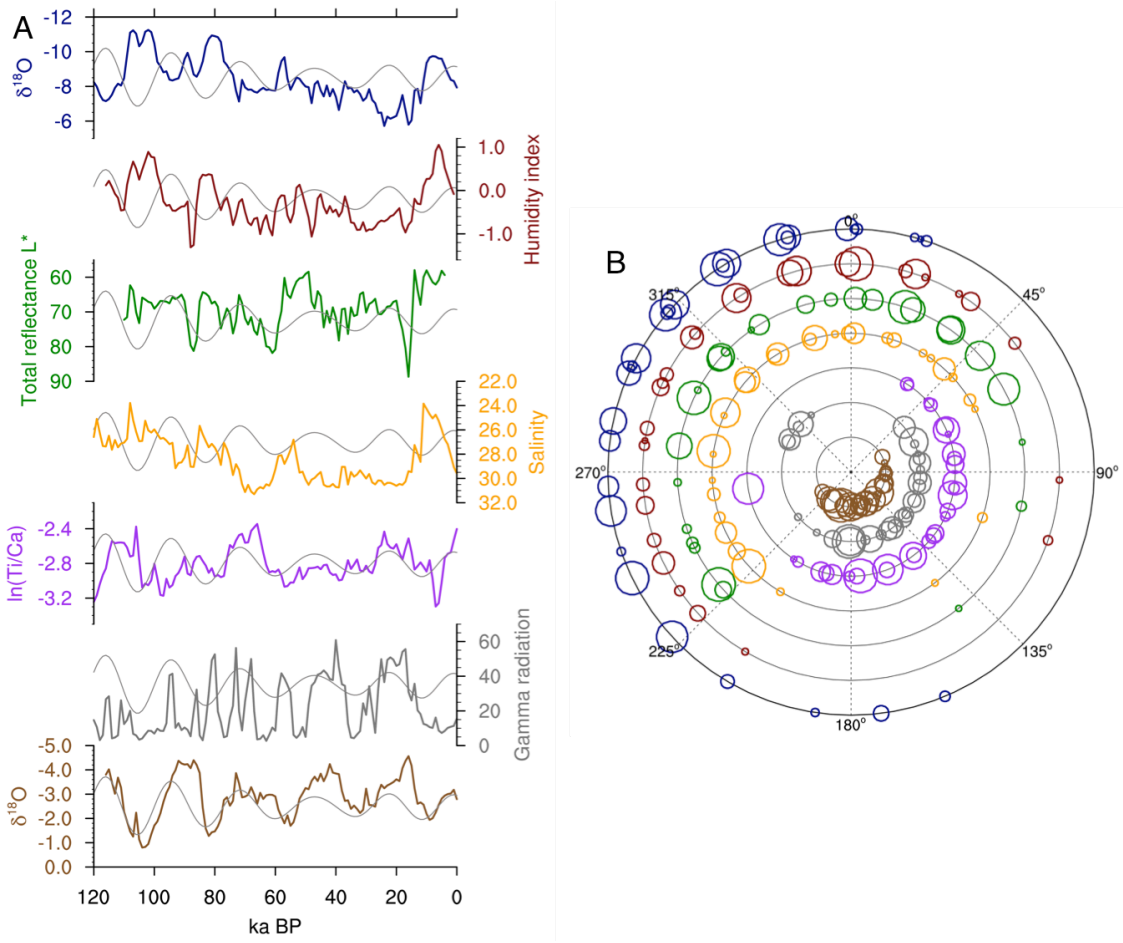

Figure 2.1: (A) Paleorecords of tropical hydroclimate against the precessional cycle ($e\sin(\omega)$, see Methods; grey); from top to bottom: composite of speleothem $\delta^{18}O$ from Chinese caves (25–32°N): Dongge (Dykoski et al., 2005), Hulu (Wang et al., 2004b), Sanbao (Wang et al., 2008); North African humidity index (20.8°N) (Tjallingii et al., 2008); sediment total reflectance in Cariaco Basin (10.7°N) (Deplazes et al., 2013); salinity reconstruction from Ba/Ca in Eastern Atlantic (2.5°N) (Weldeab et al., 2007); ln(Ti/Ca) from West Pacific Warm Pool (2.5°S) (Tachikawa et al., 2014); sediment gamma radiation from Bolivia (20.3°S) (Fritz et al., 2004); speleothem $\delta^{18}O$ from Botuvera cave (Brazil; 27.2°S) (Wang et al., 2004b, Cruz et al., 2005, Wang et al., 2007). Records are ordered from north to south, with inferred precipitation increasing along the y-axis; A 1000-year running mean was applied to each record. (B) Precessional phase ω (see Methods) of the 25% highest values of the records in (A), scaled by amplitude. Colors correspond to the records of (A)

are associated with a precessional phase opposite to that of the Southern Hemisphere precipitation maxima.

The role of precession in driving tropical climate variability has been addressed in a number of modeling studies. Most notably Clement et al. (2004) showed that the (seasonal) response of

tropical climate to precessional forcing can be as large as, and substantially different from, the response induced by the high-latitude climatic forcing usually thought to be the main driver of long-term climate variability. Many studies have particularly focused on the role of precession in driving changes in the South-East Asian and African summer monsoon systems (e.g. Kutzbach & Guetter, 1986, Braconnot & Marti, 2003, Tuenter et al., 2003, Wyrwoll et al., 2007, Kutzbach et al., 2008, Shi et al., 2011). In addition, there are numerous studies focusing on time slice experiments of Pleistocene climates that also involve precessional change, such as the mid-Holocene and the last interglacial (e.g. Kutzbach & Otto-Bliesner, 1982, Kutzbach & Liu, 1997, Zhao et al., 2005, Braconnot et al., 2008, Khon et al., 2010, Bosmans et al., 2012, Khon et al., 2012). These studies emphasize the importance of differential heating of land and ocean in driving seasonal precipitation changes in the continental monsoon regions.

Most of the studies mentioned above have focused on the *seasonal* response to precessional forcing, while the mechanisms driving precessional changes in *annual mean* precipitation have received less attention. This nonetheless poses an interesting question, given the fact that precession only changes the strength of the seasonal cycle, and not annual mean insolation. Any change in annual mean climate on precessional timescales must therefore come about through nonlinear rectification processes (Huybers & Wunsch, 2003, Rial et al., 2004, Laepple & Lohmann, 2009, Merlis et al., 2013). Here we illustrate the concept of nonlinear rectification by looking at the role of clouds in rectifying changes in surface shortwave radiation.

Suppose that we have two realizations of the climate system, whose variables x_1 and x_2 differ both in their annual mean (denoted by a bar) and average seasonal cycle (denoted by angle brackets):

$$x_1(\tau) = \overline{x_1} + \langle x_1 \rangle(\tau)$$

$$x_2(\tau) = \overline{x_2} + \langle x_2 \rangle(\tau), \text{ and} \tag{2.1}$$

$$\delta x(\tau) = x_1(\tau) - x_2(\tau), \tag{2.2}$$

where τ captures the seasonal time-evolution. The variable under consideration is shortwave radia-

tion at the surface, Q_{SW}, which is less than shortwave radiation at the top of the atmosphere (TOA), Q_{IN}, due to reflection by the surface and cloud albedo, α_S and α_C, respectively:

$$Q_{SW,i}(\tau) = (1-\overline{\alpha_S})(1-\alpha_{C,i}(\tau))Q_{IN,i}(\tau), \quad i = 1,2 \tag{2.3}$$

where

$$\alpha_{C,i}(\tau) = \overline{\alpha_{C,i}} + \langle \alpha_{C,i} \rangle(\tau), \tag{2.4}$$

and for simplicity we have assumed that α_S does not change seasonally and between climate states. Here we ignore absorption of shortwave radiation in the atmosphere. The difference in surface shortwave radiation between the two climate states is given by:

$$\begin{aligned} \delta Q_{SW} &= Q_{SW,1}(\tau) - Q_{SW,2}(\tau) \\ &= (1-\overline{\alpha_S})(1-\alpha_{C,1}(\tau))Q_{IN,1}(\tau) \\ &\quad -(1-\overline{\alpha_S})(1-\alpha_{C,2}(\tau))Q_{IN,2}(\tau). \end{aligned} \tag{2.5}$$

In this manuscript we will study two realizations of the climate system in the Community Earth System Model (CESM) 1.0.3: a simulation using maximum precession, P_{MAX}, and a simulation using minimum precession, P_{MIN}. Details of these experiments are described in Section 2.2. Figures 2.2A and 2.2C – for illustrative purposes – show the zonal mean seasonal cycle and annual mean of $Q_{IN,P_{MIN}}$ and $Q_{SW,P_{MIN}}$ respectively. The zonal mean precessionally-induced changes in TOA and surface shortwave radiation, $[\delta Q_{IN}]$ and $[\delta Q_{SW}]$, are shown in Figs 2.2B and 2.2D. While there is no precessional change in zonal annual mean TOA insolation $\left[\overline{\delta Q_{IN}}\right]$ (Fig. 2.2B), there is a substantial non-zero annual mean change in zonal mean surface insolation $\left[\overline{\delta Q_{SW}}\right]$ of more than 10 W/m^2 (Fig. 2.2D).

To assess the contributors to the annual mean surface insolation changes $\left[\overline{\delta Q_{SW}}\right]$ in Fig. 2.2D, we calculate the annual mean of the individual terms contributing to Eq. (2.5). Realizing that $\overline{\overline{x}\langle y \rangle} = \overline{x}\overline{\langle y \rangle} = 0$ and that for precession $\delta\overline{Q_{IN}} = 0$, only four terms contribute to annual mean surface

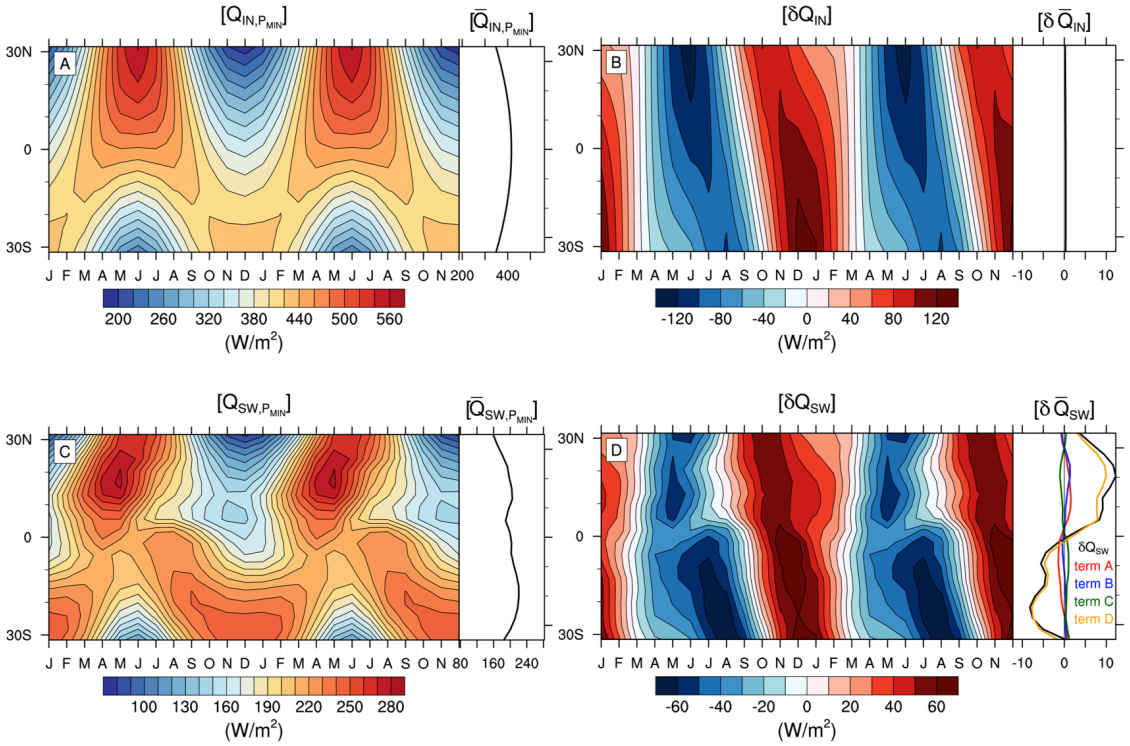

Figure 2.2: Top: Zonal mean shortwave radiation at the top of the atmosphere for (A) P_{MIN} ($[Q_{IN}]$) and (B) P_{MAX}–P_{MIN} ($[\delta Q_{IN}]$); Bottom: Zonal mean surface shortwave radiation for (E) P_{MIN} ($[Q_{SW}]$) and (F) P_{MAX}–P_{MIN} ($[\delta Q_{SW}]$). Insets on the right show the annual mean change. A detailed description of these various terms can be found in Section 2.1

insolation changes:

$$
\begin{aligned}
\left[\overline{\delta Q_{SW}}\right] = &-\left[(1-\overline{\alpha_S})\overline{\langle\alpha_C\rangle_{P_{MIN}}\,\delta\langle Q_{IN}\rangle}\right] && \text{(A)} \\
&-\left[(1-\overline{\alpha_S})\overline{\delta\langle\alpha_C\rangle\langle Q_{IN}\rangle_{P_{MIN}}}\right] && \text{(B)} \\
&-\left[(1-\overline{\alpha_S})\overline{\delta\langle\alpha_C\rangle\,\delta\langle Q_{IN}\rangle}\right] && \text{(C)} \\
&-\left[(1-\overline{\alpha_S})\overline{\delta\alpha_C}\,\overline{Q_{IN}}_{P_{MIN}}\right] && \text{(D)}
\end{aligned}
\tag{2.6}
$$

These terms are shown for the zonal mean in Fig. 2.2D. The dominant contributor to $\left[\overline{\delta Q_{SW}}\right]$ is term D in Eq. (2.6), the combination of annual mean cloud changes ($\delta\overline{\alpha_c}$) and longterm mean insolation ($\overline{Q_{IN}}_{P_{MIN}}$). The other terms, rectification of anomalous insolation by mean clouds (A), rectification of

mean insolation by anomalous clouds (B), and rectification of anomalous insolation by anomalous clouds (C), all contribute several W/m^2 each, but are of opposite sign and thus largely cancel in the zonal mean.

The aim of this paper is to identify the key mechanisms that rectify the zero-annual mean precessional forcing into an annual mean tropical precipitation response. Merlis et al. (2013) previously studied such nonlinear rectification mechanisms using idealized experiments in an aquaplanet model. They found the main nonlinearity to be a thermodynamic one, relating to the covariance of the climatological seasonal cycle of the meridional circulation with the seasonal changes in specific humidity (see their Fig. 1). This study however did not take into account the role of continents, changes in clouds, or ocean circulation. Here we look for nonlinear mechanisms rectifying the response of annual mean precipitation to seasonal precessional forcing in a more realistic modeling framework. We find that the dynamical (mean circulation) response to precessional insolation changes far outweighs the thermodynamic response, suggesting that the Merlis et al. (2013) idealized modeling setup may not translate to the real world. While in our study the zonal annual mean precipitation change follows the traditional view of the summer hemisphere with more insolation getting wetter, regional responses diverge widely. The highly regional nature of tropical hydroclimate processes impedes the identification of a universal tropical rectification mechanism. We therefore focus on a specific region, the Atlantic Intertropical Convergence Zone (ITCZ), which has been the subject of various paleoclimate reconstruction efforts (Arbuszewski et al., 2013, Deplazes et al., 2013).

Previous (paleo-)modeling and observational work has found that the Atlantic ITCZ is highly sensitive to changes in the cross-equatorial sea-surface temperature (SST) gradient (Lindzen & Nigam, 1987, Chiang et al., 2002), and responds to a variety of local and remote forcings. These include diabatic heating over the African continent (Biasutti et al., 2005), interannual variability in the Pacific and North Atlantic (Marshall et al., 2001, Chiang et al., 2002), high-latitude changes in sea ice and ice sheets (Chiang et al., 2003, Chiang & Bitz, 2005, Broccoli et al., 2006, Marzin et al., 2013), and changes in the AMOC (Timmermann et al., 2007, Deplazes et al., 2013). Here we propose that the response of the Atlantic ITCZ to precessional forcing is strongly impacted by changes in temperature

and precipitation over the surrounding continents. The African and South American land surface response to precessional forcing as well as the ability of the continents to alter the oceanic ITCZ are both seasonally dependent and thus serve as important annual rectifying processes of precipitation over the tropical Atlantic.

Section 2.2 gives a detailed description of our modeling setup. In Section 2.3.1 the large-scale patterns of annual mean tropical precipitation change associated with precessional forcing are presented. Section 2.3.2 focuses on the Atlantic ITCZ and discusses how the continental response to precessional forcing rectifies the response of the Atlantic ITCZ. Our results are compared against paleoclimate reconstructions from Cariaco Basin (Deplazes et al., 2013), Brazil (Wang et al., 2004b, Cruz et al., 2005, Wang et al., 2007), and the tropical Atlantic (Tjallingii et al., 2008, Arbuszewski et al., 2013) in Section 2.4, where we will also briefly touch on the role of eccentricity. Section 2.5 summarizes and concludes this work.

2.2 Methods

To study the response of annual mean tropical climate to precessional forcing, we performed two equilibrium simulations with CESM 1.0.3. This is a fully-coupled, global climate model consisting of interactive atmosphere (CAM4), ocean (POP2), sea ice (CICE4) and land (CLM4[1]) components. CESM1 was developed from the Community Climate System Model (CCSM) version 4 (Gent et al., 2011); its enhancements include the incorporation of biogeochemical cycles and atmospheric chemistry (Hurrell et al., 2013, Moore et al., 2013). The atmospheric model was run at T31 resolution, which corresponds to 3.75° by 3.75° horizontal resolution, with 26 vertical levels, while the ocean horizontal resolution is 3° by 3° with 60 vertical levels. This low-resolution version is ideal for performing computationally efficient long equilibrium runs and performs well when compared to higher resolution versions (Shields et al., 2012, Chikamoto et al., 2015, Stevenson et al., 2015). Figure 2.3 compares

[1]The default configuration of CLM4 used here includes a carbon-nitrogen model but does not allow for dynamic vegetation changes.

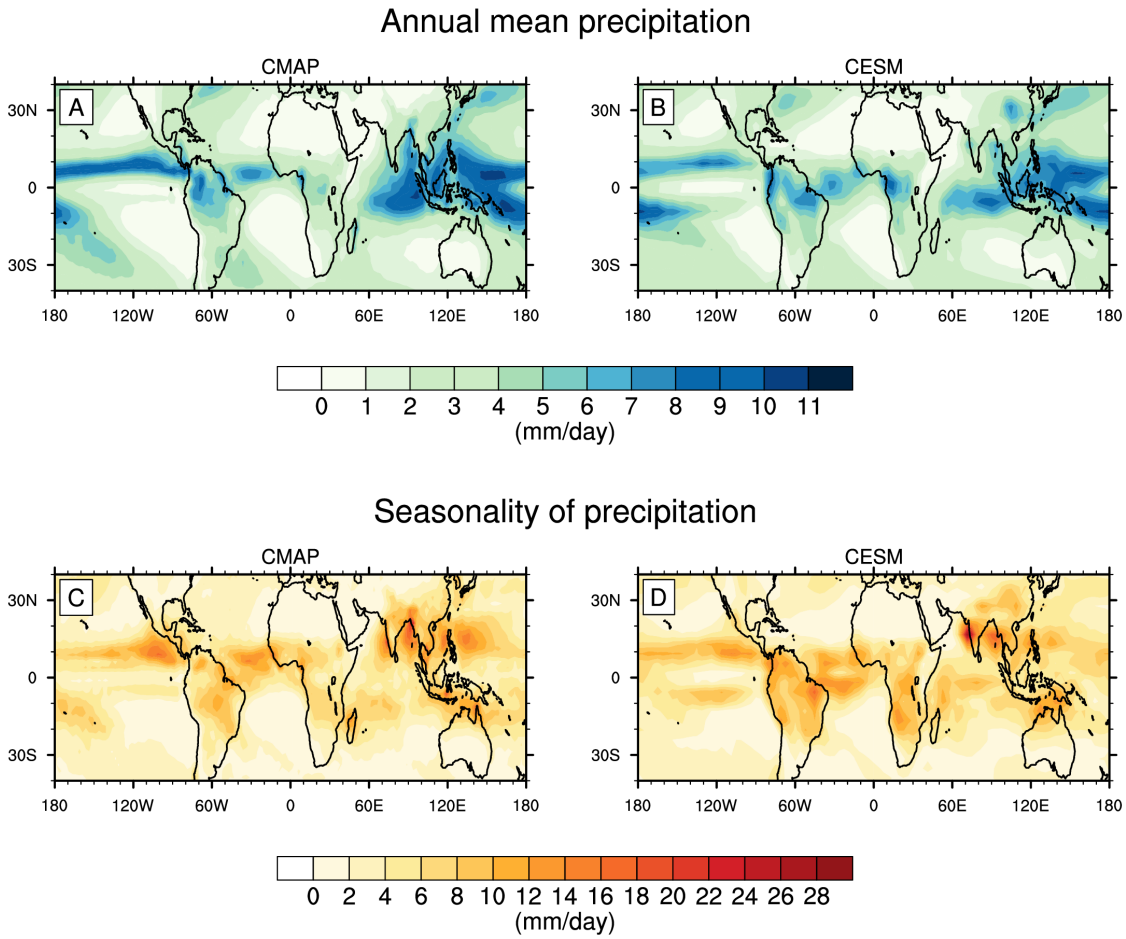

Figure 2.3: Annual mean precipitation (top) and seasonality of precipitation (maximum minus minimum of monthly climatology; bottom) for CMAP monthly climatology (enhanced version, left; Xie & Arkin, 1997) and CESM1.0.3 pre-industrial control run (right; Chikamoto et al., 2015)

tropical annual mean precipitation and seasonality of precipitation of a pre-industrial control run with CESM1.0.3 (Chikamoto et al., 2015) against the CPC Merged Analysis of Precipitation (CMAP) NCEP Reanalysis-enhanced monthly climatology (Xie & Arkin, 1997). CESM captures the dominant features of annual mean precipitation and seasonality; its main deficiencies are an underestimation of the tilt of the South Pacific Convergence Zone and annual mean precipitation over the Indian Ocean. The overestimation of Atlantic precipitation seasonality south of the equator is a result of Atlantic mean state biases common amongst CMIP5 GCMs, which simulate a reversal of the annual mean SST gradient and a boreal spring westerly wind bias (e.g. Richter et al., 2014, Siongco et al.,

2014). Richter et al. (2012) attribute this wind bias to precipitation deficits over the Amazon basin and excess precipitation over the Congo basin, also seen for CESM in Fig. 2.3.

The precessional experiments use two extreme phases of precession: one with perihelion occurring in Northern Hemisphere (NH) winter solstice ('maximum precession', P_{MAX}), and one with perihelion occurring in NH summer solstice ('minimum precession', P_{MIN}). For the precessional parameter we use the definition of precession used by Paillard (2001) and others, where $\omega = \pi + \overline{\omega}$, with $\overline{\omega}$ the angle between the vernal equinox and perihelion. As noted before, the strength of the precessional forcing is modulated by eccentricity e. To maximize the effects of precession on climate we therefore increase the value of eccentricity to e = 0.067, the maximum value during the past 51 million years (51 Ma) (Laskar et al., 2004). Pre-industrial greenhouse gas concentrations and obliquity were used. The simulations were started from an equilibrated pre-industrial control run (Chikamoto et al., 2015) and run for 500 years. The climatologies used in our analysis are linearly detrended averages over

Table 2.1: Overview of the experimental setup for the simulations with CESM1.0.3.

P_{MAX} *Maximum precession*	E_{ZERO} *Zero eccentricity*	P_{MIN} *Minimum precession*
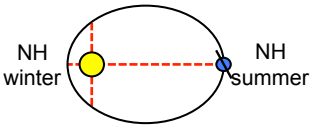	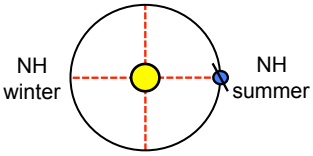	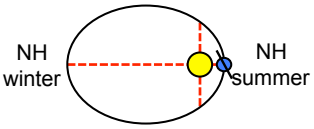
• $\omega = 270°$ • e = 0.067 • NH summer solstice in aphelion	• precession does not matter • e = 0 • aphelion = perihelion	• $\omega = 90°$ • e = 0.067 • NH summer solstice in perihelion

All experiments use pre-industrial CO_2 (284.7 ppmv), and present-day obliquity (23.4°). Simulations were run for 500 years, and climatologies were calculated over the linearly detrended last 300 years of the run

the years 201–500. Results in this paper will generally be presented as maximum minus minimum precession, P_{MAX}–P_{MIN}.

An additional run was performed with eccentricity set to zero (E_{ZERO}). In this run the orbit of the earth around the sun is perfectly circular, and there is thus no hemispheric difference in seasonal cycle strength. The results of this run will be used in Section 2.4 where we discuss rectification due to eccentricity. A summary and illustration of all three runs is given in Table 2.1.

2.3 Results

2.3.1 The tropical precipitation response to precessional forcing

The general picture that emerges from the, essentially terrestrial, proxy-estimates shown in Fig. 2.1 is that maximum precipitation in the tropics follows local maximum summer insolation. When considering the annual, zonal mean change in net precipitation in our model simulations (Fig. 2.4A) a similar view emerges: in the P_{MAX} run the tropical precipitation maximum shifts towards the Southern Hemisphere, which has a stronger SH seasonal cycle than the P_{MIN} run. This is true for precipitation over land as well as over the ocean. While the oceanic precipitation change is mostly confined between 15°S and 15°N, and switches sign roughly at the equator, continental precipitation changes have a larger meridional extent due to the strong contributions of landmasses located away from the equator (e.g. Australia, South Africa, the Himalayas) and (in the zonal mean) switch from positive to negative around 10°S.

A better understanding of regional processes is obtained by studying the spatial distribution of the annual mean precessional precipitation changes (Fig. 2.4B). The regional hydroclimate responses are clearly much more complex than just the summer hemisphere with more insolation (SH, for P_{MAX}) becoming wetter. We find a small intensification of the SH monsoon systems (South America, Southern Africa and Australia), and a decrease in precipitation over the South and East Asian monsoon regions. The annual mean ITCZ over the Atlantic shifts towards the summer hemisphere with more

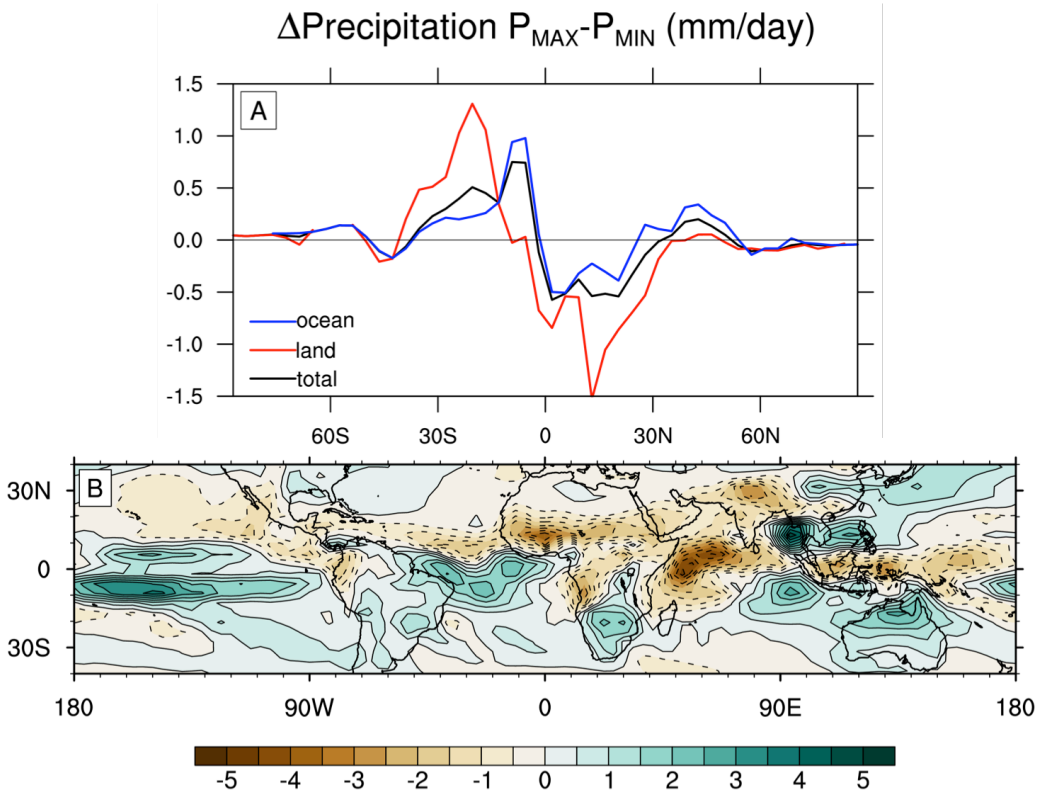

Figure 2.4: Annual mean P_{MAX}–P_{MIN} difference in precipitation (mm/day) for (A) zonal mean, separated by ocean (blue), land (red), and total (black); (B) spatial pattern in the tropics

insolation as well. But over the Pacific, there is an increase in precipitation over the northern equatorial Pacific (dateline to 110°W) in addition to a strong intensification south of the equator. The latter appears to be related to a reduction in the tilt of the South Pacific Convergence Zone. The wettening of the central Pacific is contrasted zonally with a drying of the Western Warm Pool region. Over the Indian Ocean there is a dipole pattern with a meridionally slanted zero-line. Finally there is a strong increase in annual mean precipitation over the Andaman and South China Seas. All together, Fig. 2.4B shows that the simple paradigm of precipitation shifting towards the summer hemisphere with more insolation (SH in P_{MAX}) – although valid in a zonal mean sense – does not apply universally throughout the tropics. Zonal mean frameworks of understanding the ITCZ, such as the ones discussed by Schneider (1977), Lindzen & Hou (1988), Kang et al. (2009) and Schneider

et al. (2014), will therefore not be able to explain the regional changes in tropical precipitation.

2.3.2 The Atlantic ITCZ

Position vs. intensity

The differential response across the tropics of precipitation to precessional forcing suggests that regional dynamics play an important role, and it will not be possible to find a universal mechanism driving this response. In the remainder of this paper we will therefore focus our attention on one specific region, the Atlantic ITCZ. Throughout the literature, different definitions of the ITCZ are used; here we take ITCZ to refer to either the location of maximum precipitation or the location of zero meridional wind (confluence line).

Despite an annual mean insolation profile that is symmetric around the equator, the present-day climatological annual mean ITCZ over the Atlantic Ocean is displaced into the Northern Hemisphere (e.g. Mitchell & Wallace, 1992). While the question of the hemispheric preference of the ITCZ has not been answered definitively, it has been attributed to the existence of the AMOC (e.g. Krebs & Timmermann, 2007, Schneider et al., 2014) as well as the asymmetry of the continents surrounding the Atlantic Ocean and its resulting ocean-atmosphere interactions (Xie, 1996, Xie & Saito, 2001, Xie, 2005). Seasonally the Atlantic ITCZ migrates from a position close to the equator in boreal spring to a maximum northward position around 10°N in late summer (e.g Mitchell & Wallace, 1992). This seasonal march of the ITCZ has been found to be sensitive to remote climate forcing on various timescales, such as the El Niño-Southern Oscillation (Chiang et al., 2002), the North Atlantic Oscillation (Marshall et al., 2001), Northern Hemisphere ice conditions (Chiang et al., 2003, Chiang & Bitz, 2005, Broccoli et al., 2006), the Atlantic meridional mode (Nobre & Shukla, 1996, Chiang et al., 2002, Xie & Carton, 2004), and meltwater pulses and AMOC (Broccoli et al., 2006, Timmermann et al., 2007, Deplazes et al., 2013, Marzin et al., 2013, Menviel et al., 2014).

As noted in Section 2.3.1, the annual mean Atlantic ITCZ responds to precession by shifting towards the summer hemisphere with more insolation (Fig. 2.4B), with more precipitation under

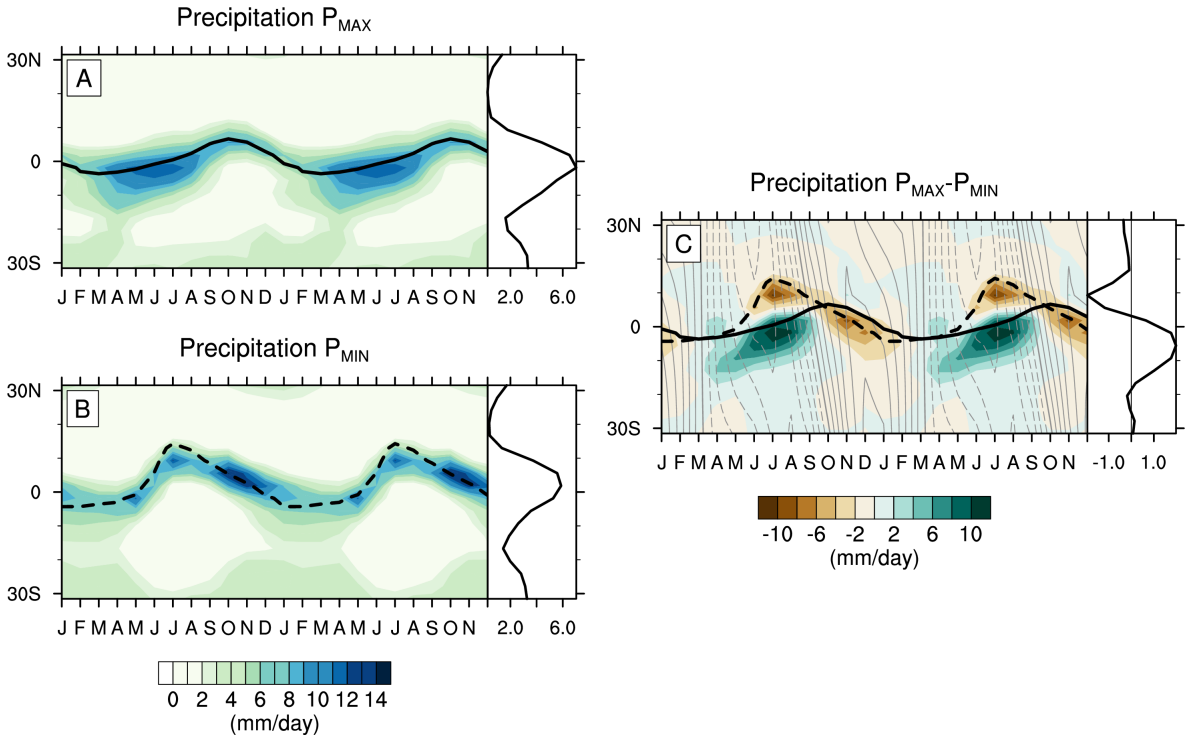

Figure 2.5: Zonal mean precipitation (mm/day) over the Atlantic (40–20°W) for (A) P_{MAX}; (B) P_{MIN}; (C) P_{MAX}–P_{MIN}. The black line indicates the position of the ITCZ as measured by the location of zero meridional wind speed for P_{MAX} (solid) and P_{MIN} (dashed). Insets on the right show the corresponding annual mean. Contours in (C) show P_{MAX}–P_{MIN} TOA insolation, as in Fig. 2.2B

P_{MAX} forcing occurring in the south, and less in the north. The resulting dipole is not centered on the equator, nor is it symmetric around its axis. Rather, the increase in precipitation on the southern side of the dipole is stronger than the decrease on its northern side. In the P_{MAX} run, total annual integrated precipitation over the Atlantic Ocean between 20°S and 20°N increases by 2.28×10^{12} m^3, or 10% (Table 2.2). For comparison, global annual integrated precipitation increases by 2.21×10^{12} m^3, or 0.5%

In the context of the precessional forcing, which has a strong seasonal component but no annual one (Fig. 2.2B), the changes in annual mean precipitation could derive from two components: A change in the seasonal march of the ITCZ (amplitude/position change), or a change in when precipitation occurs along this march (phase change). Fig. 2.5 shows monthly mean precipitation and position of

the Atlantic ITCZ as measured by the location of zero meridional wind, averaged between 40°W and 20°W. (This longitude range was chosen to isolate the oceanic ITCZ response.) In boreal spring and summer, when the P_{MIN} insolation in both hemispheres exceeds that of P_{MAX} (see Fig. 2.2B), the ITCZ travels further north, and at an earlier time of year, in the P_{MIN} simulation (Fig. 2.5B) than in the P_{MAX} simulation (Fig. 2.5A). In boreal fall and winter, when the P_{MAX} insolation exceeds that of P_{MIN}, the reverse does not happen however: The P_{MAX} and P_{MIN} ITCZs reach approximately the same southward extent. This change in seasonal march of the confluence line – even without a change in seasonality – implies a northward shift of the annual mean Atlantic ITCZ in P_{MIN} compared to P_{MAX}.

In addition to a change in meridional position, there is a change in phase of the precipitation: Under maximum precession (Fig. 2.5A), most of the precipitation over the tropical Atlantic falls between April and July, while under minimum precession (Fig. 2.5B) there are two precipitation maxima – a brief one in July and a more extended one between September and December. The oceanic precipitation maxima (Fig. 2.5A,B) thus occur several months after maximum TOA insolation (Fig. 2.2A).

Different mechanisms are thought to be responsible for driving changes in position and intensity of oceanic moisture convergence in the tropics. Changes in *meridional position* are caused by a mechanism originally proposed by Lindzen & Nigam (1987), relating convergence in the boundary layer to surface pressure gradients caused by meridional (cross-equatorial) SST gradients (see also Tomas et al., 1999). We will refer to this process as the 'boundary layer mechanism'. An initial

Table 2.2: Seasonally and annually integrated P_{MAX}–P_{MIN} difference in total precipitation (m^3 and %) over the South American continent (80°W–40°W, 30°S–10°N), Atlantic Ocean (60°W–20°E, 20°S–20°N) and African continent (10°W–30°E, 30°S–30°N)

	South America		Atlantic		Africa	
	m^3	%	m^3	%	m^3	%
DJF	2.29×10^{12}	36.2	-1.91×10^{12}	−32.9	2.69×10^{12}	85.9
MAM	-4.67×10^{11}	−7.0	2.38×10^{12}	47.5	-1.75×10^{12}	−35.2
JJA	-8.46×10^{11}	−22.2	3.48×10^{12}	66.7	-5.51×10^{12}	−81.1
SON	6.81×10^{11}	10.8	-1.66×10^{12}	−24.4	1.92×10^{11}	4.1
Annual	1.66×10^{12}	7.2	2.28×10^{12}	10.0	-4.38×10^{12}	−22.4

meridional displacement can be further amplified by a process known as the Wind-Evaporation-SST (WES) feedback (Xie & Philander, 1994): changes in low-level convergence will affect latent heat fluxes and can feed back positively onto the anomalous SST gradient. Numerous studies have shown that the WES feedback is an important amplifier of meridional ITCZ shifts over the Atlantic Ocean (e.g. Braconnot et al., 2000, Biasutti et al., 2005, Zhao et al., 2005, Bosmans et al., 2012).

On the other hand, Gill (1980) and subsequent studies (e.g. Chiang et al., 2001, Biasutti et al., 2004) looked at the entire troposphere, and found that local diabatic forcing can change the stability profile of surrounding areas and drive anomalous adiabatic vertical motion elsewhere, resulting in divergence changes. We will refer to these processes as the 'full troposphere mechanism'. Biasutti et al. (2004, 2005) showed that the precipitation response to remote diabatic forcing depends heavily on the background stability of the troposphere. Changes in diabatic heating are most likely to induce remote changes in regions where there is already precipitation occurring. The full troposphere mechanism therefore mostly impacts the *intensity* of precipitation.

In the following sections we more closely evaluate the precipitation response in individual seasons to see what drives precessional changes in the intensity and meridional position of the ITCZ. The main results are summarized schematically in Fig. 2.6. We argue that the precessional precipitation response over the Atlantic Ocean is a direct result of continental forcing. The continental response to precessional forcing, and the oceanic response to these continental changes, vary in time and space and thus rectify the annual mean change of the Atlantic ITCZ.

The JJA ITCZ

In JJA, precipitation over the Atlantic Ocean in P_{MAX} increases between 5°S-5°N, while it decreases between 5°N and 10°N (Fig. 2.7A, contours). These simulated changes in precipitation could be driven by temperature-induced changes in specific humidity ('thermodynamics'), by changes in the mean circulation ('dynamics'), by changes in transient eddy moisture convergence or by changes in evaporation. While Merlis et al. (2013) in an aquaplanet simulation attributed precessionally

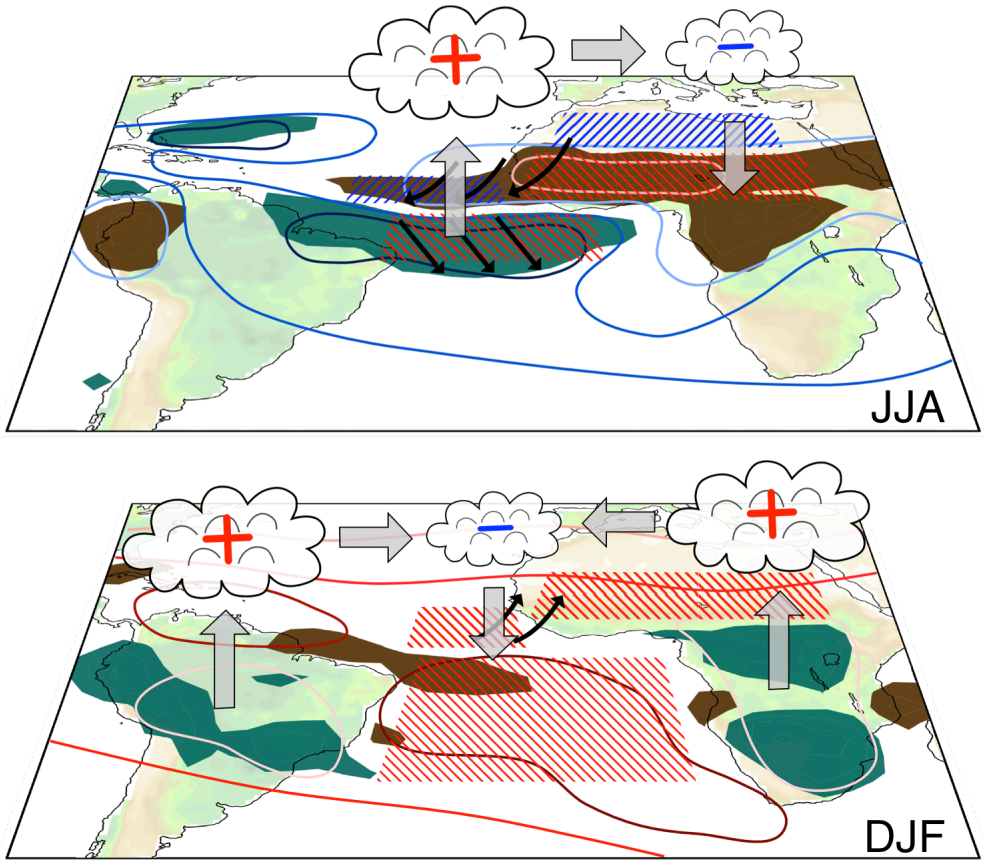

Figure 2.6: Schematic illustrating the main processes affecting the position and intensity of the Atlantic ITCZ for JJA (top) and DJF (bottom), P_{MAX}–P_{MIN}. Changes in precipitation are indicated by green (wetter) and brown (drier) shading; contours indicate changes in surface shortwave radiation, with darker colors representing larger changes; red (left-slanted) and blue (right-slanted) hatching show surface warming and cooling respectively; black arrows indicate changes in surface winds, while grey arrows show changes in vertical circulation

induced changes in the ITCZ mostly to thermodynamic processes, a decomposition of the moisture budget in our simulations (along the lines of e.g. Trenberth & Guillemot, 1995, Clement et al., 2004, Held & Soden, 2006, Seager et al., 2010) indicates that the dominant contribution to JJA precipitation changes over the Atlantic are changes in the mean circulation, in particular its convergence (see Appendix A). We suggest that in this season, the meridional position of the Atlantic ITCZ is impacted by surface temperature changes over Africa, while its intensity is affected by changes in the African summer monsoon.

Between March and August there is a P_{MAX}-induced anomalous reduction in TOA shortwave

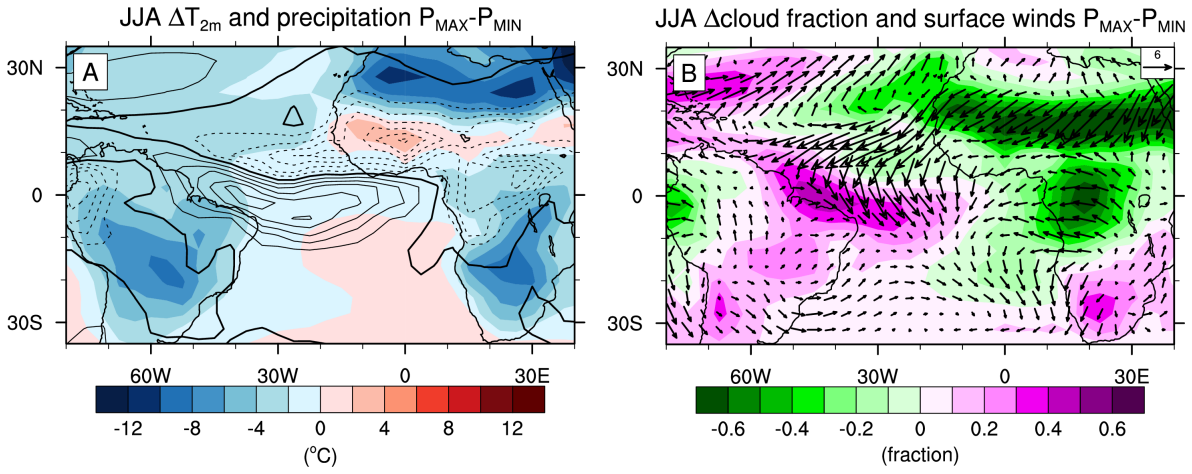

Figure 2.7: JJA P_{MAX}–P_{MIN} change in (A) 2m temperature (°C; colors) and precipitation (contour levels 2 mm/day); and (B) cloud fraction (colors) and surface winds (m/s; vectors)

radiation throughout the entire tropics (Fig. 2.2B). Figure 2.7a shows the resulting changes in JJA 2m temperature and precipitation. Over northern Africa (>20°N), where climatological soil moisture is low, the reduction in insolation leads to strong continental cooling. South of 20°N, it causes a weakening of the climatological African summer monsoon and equatorial precipitation: total precipitation over the African continent in P_{MAX} is reduced by 35% in MAM and 81% in JJA (see Table 2.2; Fig. 2.7A). This weakening is accompanied by a reduction in cloudiness (Fig. 2.7B) and evaporative cooling that creates a net surface forcing opposite in sign to the original TOA forcing. This results in a reduction of the P_{MAX} cooling between 10°S-10°N, and even a slight warming between 10°N-20°N (Fig. 2.7A).

As shown by Chiang et al. (2001), the North Atlantic trade winds strongly respond to remote influences such as ENSO and continental forcing (unlike the Atlantic cross-equatorial winds, which are very sensitive to changes in the cross-equatorial SST gradient). The reduction of continental temperatures over northern Africa drives wind changes that advect dry air southward, and strengthen the North Atlantic trades in P_{MAX} (Fig. 2.7B). This intensification of the trade winds sets up an anomalous meridional SST gradient that alters the meridional position of the Atlantic ITCZ through the boundary layer mechanism.

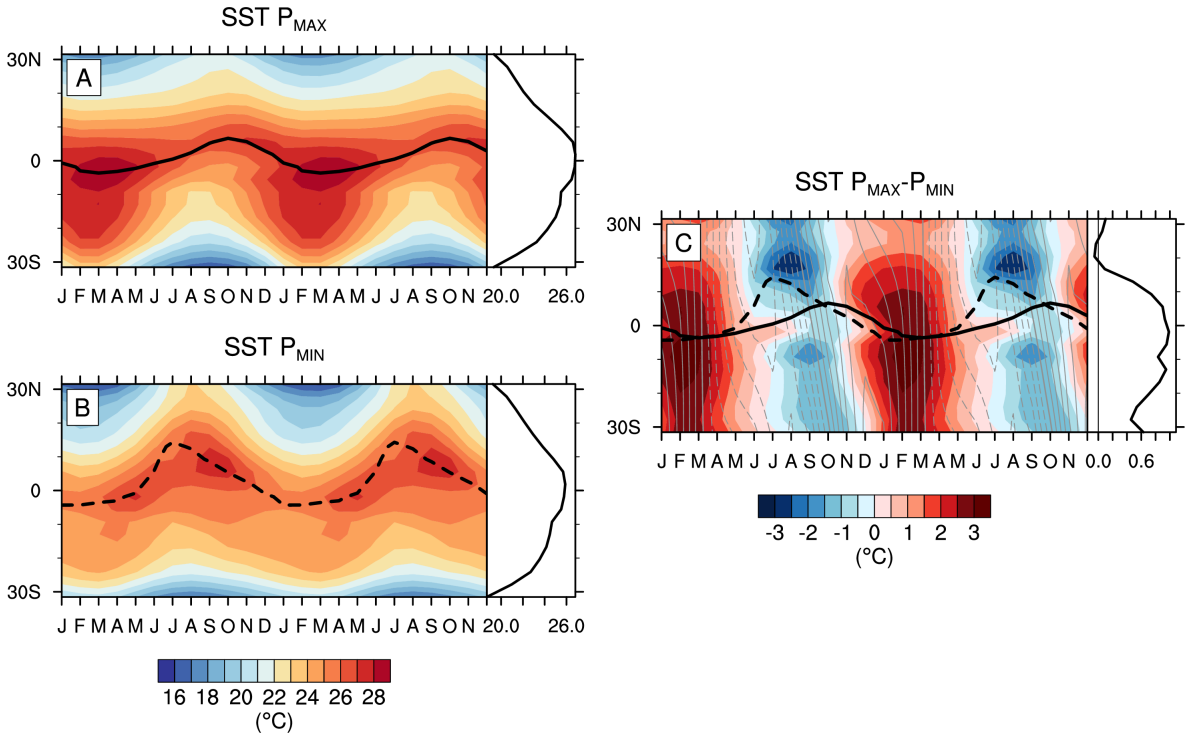

Figure 2.8: Zonal mean SST (°C) over the Atlantic (40–20°W) for (A) P_{MAX}; (B) P_{MIN}; (C) P_{MAX}–P_{MIN}. The black line indicates the position of the ITCZ as measured by the location of zero meridional wind speed for P_{MAX} (solid) and P_{MIN} (dashed). Insets on the right show the corresponding annual mean. Contours in (C) show P_{MAX}–P_{MIN} TOA insolation, as in Fig. 2.2B

Figure 2.8 shows the P_{MAX} and P_{MIN} zonal mean Atlantic SSTs and their difference, averaged between 40°W and 20°W. Generally the maximum precipitation, maximum SST and the confluence line are closely co-located, with the notable exception of P_{MIN} JJA, when the precipitation maximum is located in between the confluence line and SST maximum (Figs. 2.5 and 2.8). Previous work has indicated that SST and precipitation maxima do not co-locate when meridional pressure gradients play an important role in driving moisture convergence (e.g. Tomas & Webster, 1997). Indeed, Fig. 2.8C indicates that the anomalous northward ITCZ shift in P_{MIN} JJA coincides with the onset of an anomalous meridional SST gradient.

The role of the strengthening trade winds in driving the onset of this anomalous meridional SST gradient can be illustrated through a calculation of the mixed layer heat budget. The time evolution

of the vertically integrated mixed layer temperature is given by the SST equation:

$$\begin{aligned} c_p \rho_0 H \frac{\partial T}{\partial t} &= D_o + Q_{net} \\ &= D_o + Q_{SW} + Q_{LW} + Q_{LH} + Q_{SH}. \end{aligned} \tag{2.7}$$

Here T is SST, c_p is the specific heat capacity at constant pressure, ρ_0 the density of seawater, and H the seasonally and spatially varying mixed layer depth. Q_{SW}, Q_{LW}, Q_{LH}, and Q_{SH} are the surface heat fluxes from shortwave and longwave radiation, latent heat and sensible heat respectively. D_o represents the changes in mixed layer temperature due to ocean heat transport (three-dimensional advection and mixing). We can calculate the change in mixed layer heating rate from

$$\begin{aligned} \delta \left(c_p \rho_0 H \frac{\partial T}{\partial t} \right) = \delta Q_{SW} + \delta Q_{LW} + \delta Q_{LH} \\ + \delta Q_{SH} + \delta D_o, \end{aligned} \tag{2.8}$$

which after some manipulation becomes

$$\begin{aligned} \delta \frac{\partial T}{\partial t} = \frac{1}{c_p \rho_0} \frac{1}{H_{P_{MAX}}} \{ \delta Q_{SW} + \delta Q_{LW} + \delta Q_{LH} \\ + \delta Q_{SH} + \delta D_o \} - \frac{\delta H}{H_{P_{MAX}}} \left(\frac{\partial T}{\partial t} \right)_{P_{MIN}}, \end{aligned} \tag{2.9}$$

where δ is the difference operator P_{MAX}–P_{MIN}.

Figure 2.9 shows these various contributions to the change in heating rate. Note that the negative latent heat and sensible heat flux changes are plotted so that blue and red correspond to cooling and heating respectively. The ocean heat transport term in Fig. 2.9F was calculated as the residual from the surface heat fluxes and the $c_p \rho_0 H \frac{\partial T}{\partial t}$ term. Over the ocean, there is generally a 1-2 month lag between insolation forcing and surface temperature changes. In order to understand the onset of the anomalous SST gradient in May, as seen in Fig. 2.8C, we therefore need to understand the contributions to $\delta \frac{\partial T}{\partial t}$ in March (referenced by the solid green line in Fig. 2.9).

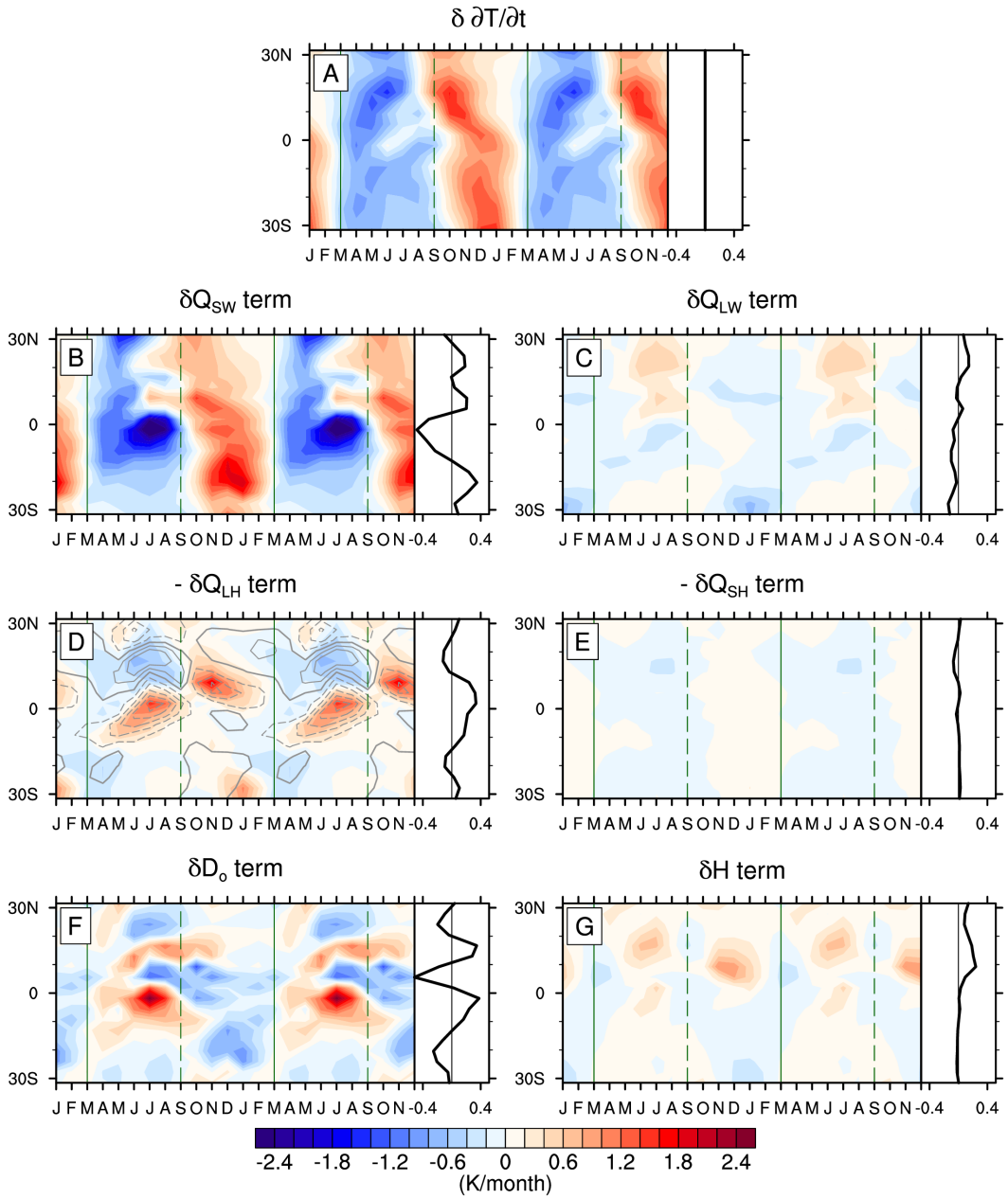

Figure 2.9: Zonal mean contributions to the P_{MAX}–P_{MIN} change in heating rate (°C/month) of the Atlantic Ocean (40–20°W) mixed layer (A), from (B) a change in shortwave radiation; (C) a change in longwave radiation; (D) a change in latent heat flux (negative plotted); (E) a change in sensible heat flux (negative plotted); (F) changes in advection and mixing; (G) changes in mixed layer depth; see Eq. (2.9). Insets on the right show the corresponding annual mean; green lines indicate the March (solid) and September (dashed) months for reference. Contours in (D) show P_{MAX}–P_{MIN} wind speed

The TOA insolation forcing shown in Fig. 2.2B shows little meridional gradient in boreal spring. At the surface, net shortwave radiation δQ_{SW} (Fig. 2.9B) shows a strong cooling between 20°S and 10°N which is due to a P_{MAX} increase in cloudiness over these latitudes (Fig. 2.7B) following the precipitation changes of Fig. 2.5C. By contrast, the total anomalous heating rate plotted in Fig. 2.9A shows strongest cooling in boreal spring over the North Atlantic. This cooling is the result of an anomalous P_{MAX} increase in the surface latent heat flux (Fig. 2.9D) which cools the North Atlantic starting in March, while a decrease in latent heat flux warms the Atlantic just south of the equator. Throughout boreal spring and summer, the changes in latent heat flux continue to warm the Atlantic south of 5°N and cool it north of that in P_{MAX}. The dipole in latent heat flux changes is formed by the P_{MAX} strengthening of the trade winds over the North Atlantic, and a weakening of the cross-equatorial winds in boreal spring and summer (Fig. 2.7B and contours in Fig. 2.9D). It is a clear indication that the WES feedback is at work: The P_{MAX} cooling of the North Atlantic caused by the boreal spring strengthening of the trades reduces the meridional SST gradient, which keeps the region of convergence close to the equator, weakening the cross-equatorial winds, and warming the equatorial region (Fig. 2.9D). This warming further reduces the meridional SST gradient (Fig. 2.8C) and keeps the ITCZ south. The opposite is the case in the P_{MIN} simulation, where an increased meridional SST gradient pushes the Atlantic ITCZ north (Fig. 2.5C).

Coincident with the latent heat flux anomalies, changes in ocean heat transport warm the Atlantic south of 5°N in P_{MAX} (Fig. 2.9F). They further contribute to the P_{MAX} weakening of the meridional SST gradient in boreal spring and summer. The longwave, sensible heat, and mixed layer terms of Eq. (2.9), shown in Figs. 2.9C, E, and G respectively, contribute little to these heating rate changes. These results thus indicate that through the boundary layer mechanism and amplified by the WES feedback, precessional changes in African temperature and resulting surface wind changes alter the meridional position of the Atlantic ITCZ. While the entire South American continent cools in response to the P_{MAX} forcing (Fig. 2.7A), this cooling does not induce surface wind changes that can impact the ITCZ position (Fig. 2.7B).

Figure 2.10 shows JJA cross-sections of vertical velocity changes averaged over various latitude

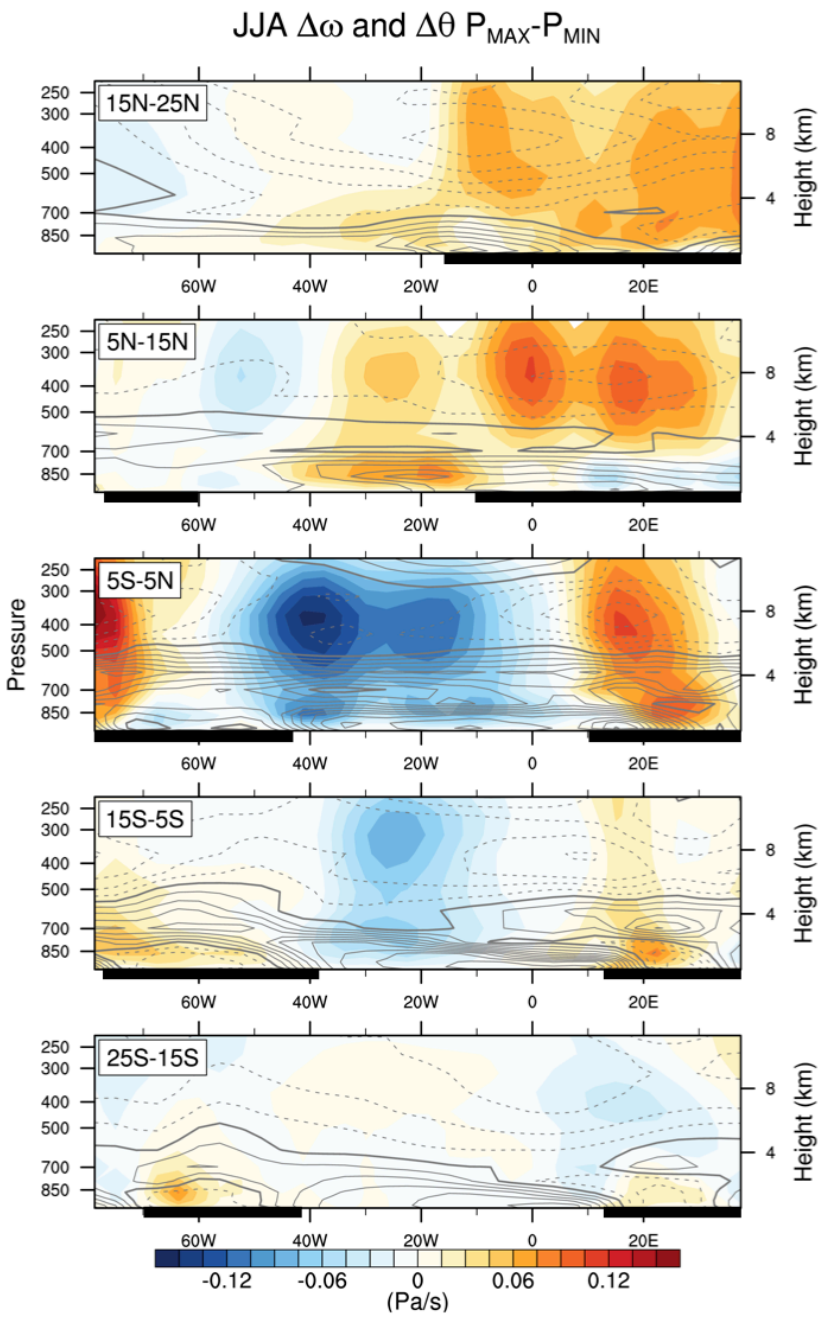

Figure 2.10: JJA P_{MAX}–P_{MIN} change in vertical velocity (Pa/s; colors) and potential temperature anomalies with respect to the vertical average (contour levels 0.5°C) for various latitude bands across the tropical Atlantic: (A) 15°N–25°N; (B) 5°N–15°N; (C) 5°S–5°N; (D) 15°S–5°S; (E) 25°S–15°S. Black bars indicate land

bands. Between 15°S and 5°N, vertical velocity changes over the ocean are opposite in sign to those over the continents (esp. Africa), showing that convection over the ocean decreases when it increases over land. The vertical profile of change in this area is very different from that north of 5°N, where over the Atlantic Ocean (50°W–20°W) the response is mostly limited to the boundary layer. Contours in Fig. 2.10 show potential temperature anomalies with respect to vertical mean changes. Throughout the tropics, the upper troposphere cools compared to the lower troposphere, indicating reduced stability. Together, the vertical velocity and potential temperature changes suggest that the mechanisms described by Biasutti et al. (2004) are at work: the decrease in continental precipitation cools the upper troposphere due to a reduction in diabatic heating, which then reduces the large-scale stability profile and increases convection in areas where the background stability is weak. Between 5°S and 5°N, the diabatic heating (not shown) resulting from the continentally-driven increase in oceanic precipitation partially offsets the large-scale cooling in the upper troposphere. Because climatological precipitation over South America is low in this season, and precessional changes in precipitation are small (Fig. 2.7A, Table 2.2), continental changes on the western side of the Atlantic hardly impact the Atlantic ITCZ.

The mechanisms described above are illustrated in the top panel of Fig. 2.6. The *position* of the Atlantic ITCZ is affected by P_{MAX} continental cooling over northern Africa, which increases the North Atlantic trades, and through the WES-feedback and wind-induced changes in ocean heat transport reduces the cross-equatorial SST gradient, keeping the P_{MAX} ITCZ south. A P_{MAX} weakening of the African summer monsoon affects the large-scale stratification profile by cooling the upper troposphere, increasing precipitation in areas that are already unstable, thus changing the *intensity* of the Atlantic ITCZ. As we shall see in the next section, the magnitude of the processes described above is not seasonally symmetric, thus rectifying the precipitation response in the annual mean.

The DJF ITCZ

The response of the Atlantic ITCZ to DJF forcing is markedly different from the JJA changes described above. As seen in Fig. 2.5, the P_{MAX} rainfall maximum attains the same southernmost position as that of P_{MIN}. Figure 2.11A shows that in DJF P_{MAX} precipitation decreases over much of the Atlantic, except close to the African continent. The magnitude of the DJF precipitation response is smaller than that in JJA. An analysis of the DJF moisture budget components indicates that again, the precipitation changes over the ocean are dominated by changes in wind convergence rather than specific humidity (Appendix A, Fig. A.2). Our coupled model simulations suggest that in this season, changes in continental temperature fail to alter trade winds significantly (Fig. 2.11) and initiate the WES feedback. Changes in precipitation over both Africa and South America affect the intensity of precipitation over the Atlantic but not its location.

The TOA P_{MAX}–P_{MIN} shortwave forcing in boreal winter (Fig. 2.2B) is almost the exact mirror image of the boreal summer forcing. From approximately October to March, incoming shortwave radiation in P_{MAX} exceeds that in P_{MIN} throughout the entire tropics, with the strongest forcing over the Southern Hemisphere. In response to this anomalous P_{MAX} increase in insolation in boreal fall and winter (Fig. 2.2B), the entire African continent warms up, as shown in Fig. 2.11A for DJF. Between 10°N-20°N the increase in insolation is amplified by an increase in downward longwave radiation (not shown). South of 10°N, the increase in shortwave radiation leads to an increase in precipitation over the African continent (by as much as 86% in DJF (Table 2.2)). As for JJA, precipitation changes over continental Africa in DJF mostly derive from changes in tropospheric convergence, with smaller contributions from evaporation changes and, over southern Africa, a nonlinear and surface term (Fig. A.2; see explanation in Appendix A). The resulting increase in cloudiness (Fig. 2.11B) and evaporative cooling partially (but not entirely) offset the expected warming (compare Fig. 2.7A and Fig. 2.11A).

The positive P_{MAX} shortwave forcing enhances the austral summer monsoon over South America. Total precipitation over the South American continent increases by 36% in DJF (Table 2.2). The

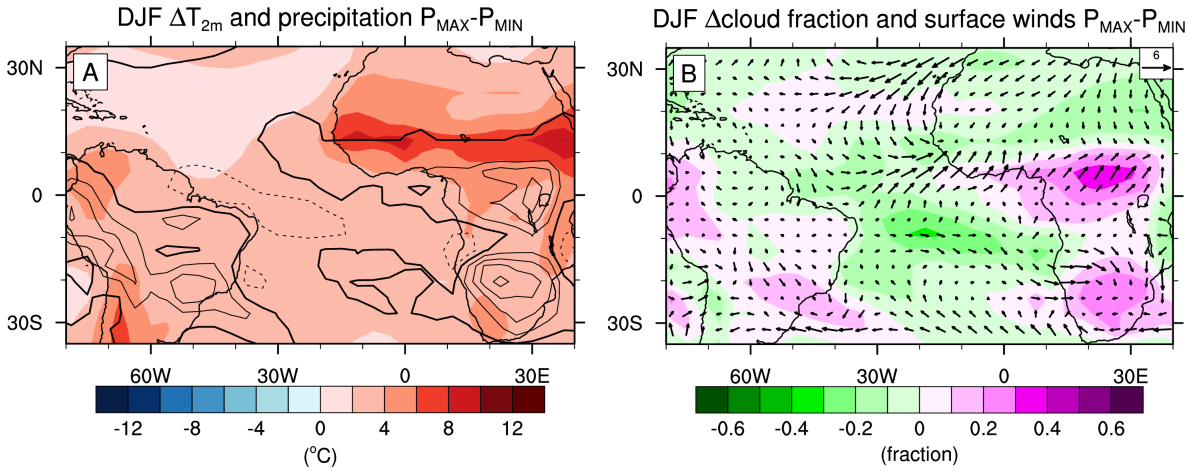

Figure 2.11: DJF P_{MAX}–P_{MIN} change in (A) 2m temperature (°C; colors) and precipitation (contour levels 2 mm/day); and (B) cloud fraction (colors) and surface winds (m/s; vectors)

increase in precipitation largely derives from an increase in wind convergence, but is partially offset by a decrease in moisture advection as increased evaporation over the continent decreases the land-ocean humidity gradient (see Appendix A, Fig. A.2). The entire South American continent warms in response to the positive shortwave forcing (Fig. 2.11A), although here as well, continental warming is limited by increased cloudiness (Fig. 2.11B) and latent heat flux.

Even though the P_{MAX} increase in TOA insolation is strongest over the Southern Hemisphere (Fig. 2.2B), continental warming is most pronounced over northern Africa (Fig. 2.11A). This warming causes a thermal low that slightly weakens the P_{MAX} North Atlantic trades (Fig. 2.11B). As evidenced by the heat flux analysis in Fig. 2.9, this weakening leads to a reduction in oceanic latent heat flux (Fig. 2.9D) and shallowing of the mixed layer (Fig. 2.9F) that warm the North Atlantic . This keeps the P_{MAX} ITCZ *north* (Fig. 2.5) at a time when the climatological ITCZ is moving south. At the same time, the southern tropical Atlantic is warming (Fig. 2.9A) due to the P_{MAX} increase in shortwave radiation (Fig. 2.9B). As a result, no meridional heating gradient develops, and the WES-feedback cannot enhance the meridional shift; between December and May the entire tropical Atlantic warms up (Fig. 2.8C). The overall warming is opposed by ocean heat transport changes (Fig. 2.9E) that cool the equatorial and South Atlantic. Changes in longwave radiation and sensible heat flux (Figs. 2.9C

and e respectively) again play a negligible role. The boundary layer mechanism that was shown to be essential for the JJA meridional ITCZ shift is thus of minor importance in DJF. This is also shown in Fig. 2.12 which shows that there is very little boundary layer response in this season, indicating that a full troposphere response to diabatic heating dominates over the boundary layer mechanism.

Figure 2.12 shows DJF cross-sections of vertical velocity changes in various latitude bands over the tropical Atlantic. Much like in JJA, vertical velocity changes between 15°S and 5°N over the Atlantic ocean are opposite in sign to those over the continents. The strengthening of the austral summer (DJF) South American and African monsoon systems under maximum precession is associated with increased upward motion over land, in particular over Africa between 5°S and 5°N (Fig. 2.12). The associated convective heating (not shown) warms the upper troposphere (contours in Fig. 2.12), making it more stable and reducing convection over the ocean in P_{MAX} (Figs. 2.5, 2.11A). Biasutti et al. (2004) showed that convection changes over South America and southern Africa play comparable roles in driving precipitation anomalies in the Atlantic ITCZ. The precipitation changes over the South American and African continents in DJF are smaller than those in JJA (Table 2.2; Figs. 2.7A and 2.11A) so the full troposphere response in this season is weaker as well (compare Figs. 2.10 and 2.12).

Even though the DJF P_{MAX}-P_{MIN} change in TOA shortwave forcing is almost the exact mirror image of the JJA forcing (Fig. 2.2B), the ITCZ response to this forcing is markedly different. The mechanisms described in this section are summarized in the bottom panel of Fig. 2.6. Despite stronger shortwave forcing in the Southern Hemisphere, the strongest continental heating is found over Northern Africa, leading to a slight weakening of the North Atlantic trades and warming of the North Atlantic. Because the South Atlantic is warming at the same time, meridional SST gradients are muted and the WES feedback does not operate. The net effect is that the *position* of the ITCZ does not change. Atlantic precipitation is mostly impacted by an increase in continental precipitation, which through diabatic heating and resulting changes in large-scale stratification decreases the *intensity* of oceanic precipitation.

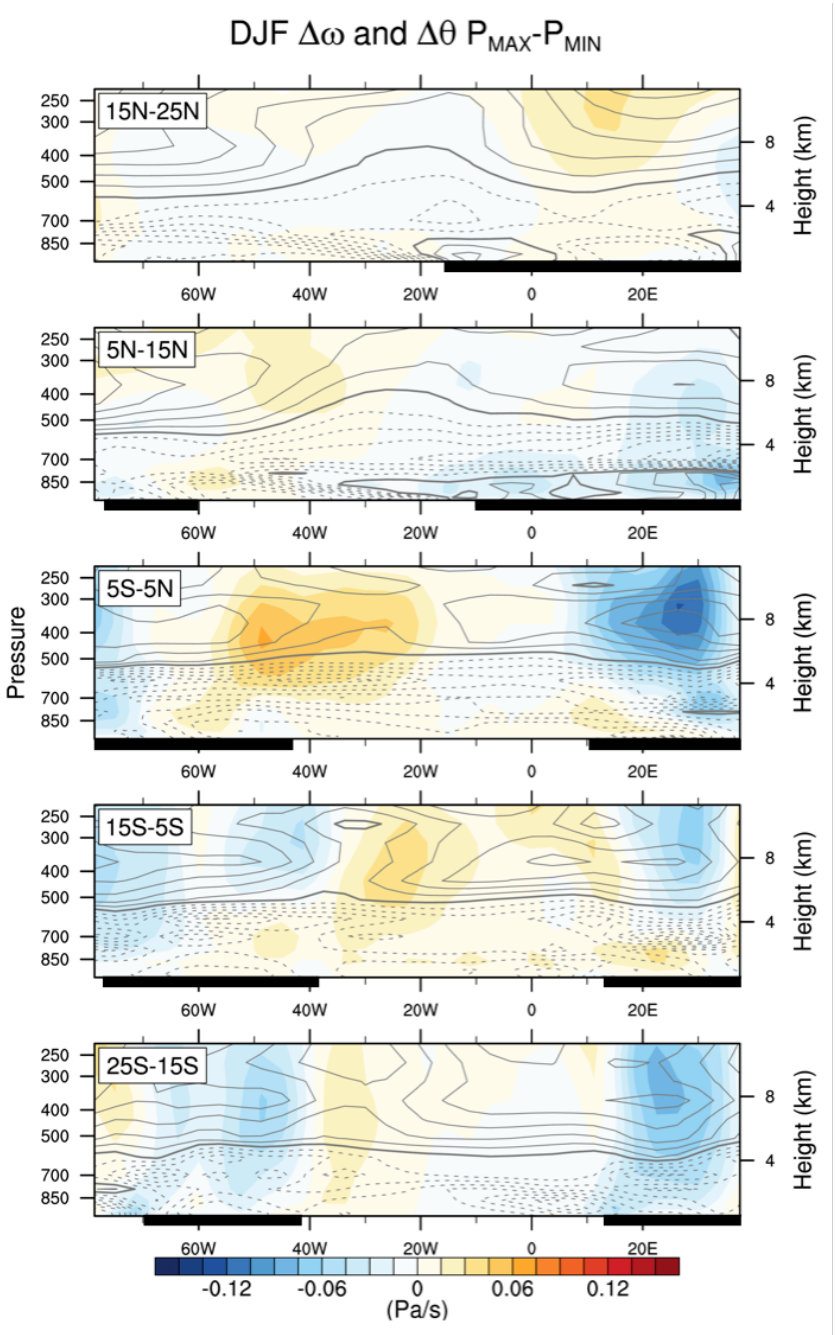

Figure 2.12: DJF P_{MAX}–P_{MIN} change in vertical velocity (Pa/s; colors) and potential temperature anomalies with respect to the vertical average (contour levels 0.5°C) for various latitude bands across the tropical Atlantic: (A) 15°N–25°N; (B) 5°N–15°N; (C) 5°S–5°N; (D) 15°S–5°S; (E) 25°S–15°S. Black bars indicate land

2.4 Discussion

2.4.1 Nonlinear rectification of the annual mean response

In this study we analyze the response of annual mean precipitation over the Atlantic Ocean to precessional forcing. In an annual mean sense, the precipitation change over the tropical Atlantic (Fig. 2.4B) seems to be in accordance with the paradigm of the summer hemisphere with more insolation getting wetter. However, looking at the seasonal response in Fig. 2.5C, we see that Atlantic precipitation actually *decreases* in the season with more insolation. Section 2.3.2 showed that the response of the Atlantic ITCZ to seasonally symmetric precessional forcing is strongly seasonally asymmetric. We propose that the continents bordering the Atlantic Ocean play a key role in creating this asymmetry (see Fig. 2.6). The following processes are identified as being responsible for rectifying the annual mean response of the Atlantic ITCZ to precessional forcing:

- The differential continental response to seasonal TOA insolation forcing:
  - The response of the continental monsoon to seasonal insolation changes is much larger in JJA than in DJF (see Table 2.2; compare Fig. 2.7A to Fig. 2.11A and Fig. 2.10 to Fig. 2.12). As a result, the continental diabatic forcing affecting the *intensity* of oceanic precipitation will be stronger in JJA as well, skewing the annual mean response. Biasutti et al. (2004) showed that an increase in insolation affects precipitation over different parts of the African continent in different ways: Over southern Africa, it lowers atmospheric stability by causing low-level warming; over North Africa the atmosphere becomes more unstable because increased monsoon flow brings more low-level moisture. Hence, a strengthening of the seasonal cycle in the Northern Hemisphere affects precipitation over Africa differently than a strengthening of the seasonal cycle in the Southern Hemisphere.
  - Figs. 2.7A and 2.11A show that the strongest continental temperature response is always found somewhere over northern Africa, even though in DJF the strongest shortwave forcing

is over southern Africa. This differential response relates to climatological differences in soil moisture, ground evaporation, and monsoon location.

- The boundary layer mechanism and WES feedback:
  - Chiang et al. (2001) and Xie & Saito (2001) argued that surface winds over the northern tropical Atlantic are more sensitive to continental forcing than winds over the equatorial and southern tropical Atlantic. Under precessional forcing the boundary layer response and resulting WES feedback (Fig. 2.9D) are therefore stronger in JJA, when the largest shortwave forcing is located in the Northern Hemisphere (Fig. 2.2B). The right-hand panel of Fig. 2.9D shows that the latent heat flux contribution to SST changes is strongly rectified in the annual mean, in particular over the North Atlantic.
  - The boundary layer mechanism, shifting the position of the oceanic ITCZ in response to a *seasonally rectified* SST gradient, will also lead to a rectification of the annual mean ITCZ position.

In recent years a framework has emerged in which changes in zonal mean ITCZ position can be diagnosed by looking at inter-hemispheric energy changes and cross-equatorial energy transport. Extratropical heating anomalies in particular, even when zonally bound (Kang et al., 2014), are found to be able to impact the ITCZ position globally, with the ITCZ shifting away from the cooling hemisphere (Broccoli et al., 2006, Kang et al., 2008, 2009, Chiang & Friedman, 2012, Donohoe et al., 2013, Schneider et al., 2014). Evidence for a high-latitude forcing of tropical climate comes from numerous modeling and observational studies which suggest that changes in land and sea ice cover, AMOC strength and meltwater pulses all can impact the meridional position of the ITCZ (Chiang et al., 2003, Chiang & Bitz, 2005, Timmermann et al., 2007, Deplazes et al., 2013, Fučkar et al., 2013, Marzin et al., 2013, Marshall et al., 2014, Menviel et al., 2014, Deser et al., 2015). Especially sea ice cover is known to be strongly rectified by precessional forcing (Tuenter et al., 2005). In our model simulations we find a strong increase in Northern Hemisphere annual mean sea ice extent under

maximum precession, which in this framework would imply a southward shift of the ITCZ.

Kang et al. (2014) recently argued that while regional extratropical cooling can shift the entire ITCZ south, regional heating anomalies in the tropics cause a much more localized ITCZ response. The zonal asymmetry of the tropical precipitation changes shown in Fig. 2.4B therefore suggests that in response to precession, regional tropical dynamics have a stronger impact on annual mean precipitation than extratropical processes (Clement et al., 2004). Without additional sensitivity experiments however it is not possible to conclusively quantify the relative importance of tropical and extratropical forcings, which in the real climate might well be time-evolving (see discussion below).

Previous studies have suggested that dynamical vegetation changes can amplify the (continental) precipitation response to precession by altering surface albedo and soil moisture (Tuenter, 2004, Claussen et al., 2006, Timm et al., 2010, Koenig et al., 2011). The land component in our modeling experiments, CLM4, includes a carbon-nitrogen model, but does not calculate dynamical changes in plant biogeography. We find that surface albedo changes in the land model do indeed amplify the TOA insolation forcing in JJA. However, these changes are small compared to cloud changes (Fig. 2.7B), so vegetation feedbacks play only a secondary role in our experiments.

2.4.2 Comparison with proxy records

A comparison of our modeling results against reconstructions of past precipitation on precessional time scales is hampered by a number of caveats:

- Precession is not the sole driver of climate variability on long time scales. In addition to the other orbital forcings (eccentricity, obliquity), the glacial cycles of the Pleistocene also saw substantial variations in high latitude (sea) ice volume and extent and atmospheric greenhouse gas concentrations.

- The strength of the precessional forcing is modulated by eccentricity. Over the last glacial cycle, precessional forcing was strongest during MIS 5, while it was weakest during MIS 2 and 3, at the same time when global ice volume was nearing its peak. The relative importance of

precessional forcing will thus vary over the course of the last glacial cycle, while the amplitude of the forcing is always smaller than the idealized forcing applied in this study.

- Reconstructions of past precipitation are not straightforward and all indirect. It is therefore not guaranteed that the proxy records of Fig. 2.1A all represent *annual mean* precipitation, and not a seasonally weighted signal (e.g. Huybers & Wunsch, 2003, Laepple & Lohmann, 2009, Timmermann et al., 2014, for more discussion on seasonal biases), net precipitation, or information about moisture source rather than amount.

Our modeling experiments found an enhancement of the summer monsoon systems with increased summer insolation, as did numerous previous studies of past monsoons (e.g. Kutzbach & Otto-Bliesner, 1982, Tuenter et al., 2003, Braconnot et al., 2008). This enhancement is also found in records from northern Africa and South America and shown in Fig. 2.1A by the anti-phasing of the north African humidity index of Tjallingii et al. (2008) and Gulf of Guinea sea surface salinity reconstruction of Weldeab et al. (2007) with the South American cave records of Wang et al. (2004b), Cruz et al. (2005) and Wang et al. (2007) and Bolivian salt flat sediment core of Fritz et al. (2004). The much-studied African Humid Period, during which grass and low shrub vegetation expanded northward into the Sahel-Sahara region, coincides with a maximum in NH summer insolation (Gasse, 2000, DeMenocal et al., 2000). The precessional response of the north African summer monsoon is limited during MIS 2 and 3, when eccentricity is low, and the high latitude ice sheets impact atmospheric circulation over northern Africa (Weldeab et al., 2007, Tjallingii et al., 2008, Timm et al., 2010, Kuechler et al., 2013). This can be seen in Fig. 2.1B, where the phase relationship between precipitation maxima and precession varies between precessional cycles.

Reconstructions of oceanic precipitation, i.e. position and intensity of the Atlantic ITCZ, are scarce. Deplazes et al. (2013) argue that changes in sediment reflectance in Cariaco Basin (10°N) are indicative of meridional ITCZ shifts. Their record mainly shows variability on millennial time-scales, while variability on precessional time-scales is limited; maximum precipitation is not in phase with maximum summer insolation (Fig. 2.1). In our modeling study, there is very little change in

annual mean precipitation over Venezuela and the Cariaco Basin in response to precession (Fig. 2.4B), suggesting that precipitation over this area might have a different seasonal sensitivity to precession. Arbuszewski et al. (2013) inferred information about the timing and magnitude of meridional ITCZ shifts since the LGM from a compilation of terrestrial and marine paleorecords. They find that the ITCZ shifted southward during the LGM, and subsequently shifted northward during the Holocene. While the southward shift at the LGM was likely strongly influenced by high-latitude processes (see discussion above), the Holocene northward shift lends support to our finding that enhancement of the terrestrial summer monsoon over north Africa (P_{MIN}) is accompanied by a northward shift of the ITCZ (Figs. 2.5 and 2.7A). Unfortunately this reconstruction barely spans a precessional cycle, making it difficult to assess the consistency of the response to precessional forcing throughout the Pleistocene. To our knowledge there are no reconstructions of paleo-precipitation from the central tropical Atlantic that could be used for a more robust comparison with our modeling results over the ocean. The general agreement between our model simulations and paleo-reconstructions of tropical precipitation give confidence that our results are robust, in spite of Atlantic mean state biases common in GCMs (Section 2.2).

2.4.3 Eccentricity as a rectifier

As was noted before, the strength of the precessional cycle is strongly modulated by eccentricity: The influence of precession is strong for high values of eccentricity, while it would be non-existent if earth's orbit were perfectly circular. In this study we therefore used a high value of eccentricity (0.067, the highest value over the past 51 Ma (Laskar et al., 2004)) to have the most pronounced signal.

The eccentricity cycle itself is only associated with a small change in annual mean insolation. Yet numerous records from the Pleistocene, Pliocene, and earlier times show substantial variability on eccentricity time scales, in particular its strongest periodicity, 400,000 years (e.g. Tiedemann et al., 1994, Herbert, 1997, Tian et al., 2002, Wang et al., 2010). This variability must therefore come about

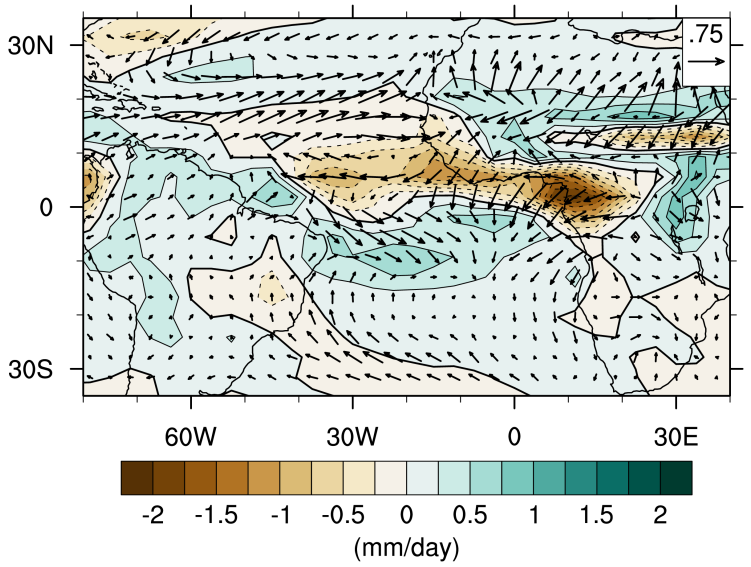

Figure 2.13: Eccentricity rectification of annual mean precipitation (mm/day; colors) and surface winds (m/s; vectors); see Eq. (2.10)

through nonlinear rectification of the precessional cycle. A measure of this rectification is the degree to which the mean between maximum (P_{MAX}) and minimum (P_{MIN}) precession deviates from the zero eccentricity state (E_{ZERO}):

$$x_{rect} = \frac{x_{P_{MAX}} + x_{P_{MIN}}}{2} - x_{E_{ZERO}} \tag{2.10}$$

This eccentricity rectification is shown for precipitation and surface winds in Fig. 2.13. The precipitation and wind changes shown in this figure are quite substantial. They amount to ~10–20% of our modeled precessional changes (Figs. 2.7 and 2.11).

Eccentricity rectification over the continents is especially apparent over northern Africa, where there might be strong soil moisture and vegetation feedbacks rectifying the response, and equatorial Africa, suggesting interactions with the Atlantic cold tongue. Over the ocean, there is a meridional shift of the ITCZ that is associated with strong wind changes over the Atlantic and near the coast of Africa. These wind changes imply changes in upwelling and hence productivity changes that could be reflected in the $\delta^{13}C$ records containing 400 ka eccentricity variability (Tiedemann et al., 1994, Herbert, 1997, Tian et al., 2002, Wang et al., 2010).

2.5 Summary & Conclusion

A simplified view of the response of tropical hydroclimate to precessional forcing is that precipitation increases with local summer insolation (Masson-Delmotte et al., 2013). Many previous modeling studies have therefore focused on the seasonal response of tropical precipitation to precession. Here we compare two idealized experiments with the earth system model CESM1.0.3 to address the mechanisms that rectify the *annual mean* precipitation response to precessional forcing. The model simulations are run with maximum precession P_{MAX} and minimum precession P_{MIN}; eccentricity is set to 0.067 to maximize the response (see Table 2.1).

In the zonal annual mean, the tropical precipitation response follows the expected pattern of the summer hemisphere with more insolation getting wetter (Fig. 2.4A). However, the regional characteristics of annual mean precipitation changes (Fig. 2.4B) are much more complex, especially over the oceans. This suggests that classical zonal mean frameworks of understanding the ITCZ are not able to explain regional changes. In our analysis we focus on the Atlantic Ocean, which displays a meridional dipole response in precipitation with its axis north of the equator. The dipole is asymmetric, with an annual mean ocean precipitation response that is stronger south of its axis than north of it. Although the annual mean precipitation response over the Atlantic seems to follow the paradigm of summer hemisphere with more insolation getting wetter, a closer examination of its phase reveals that this is not true on an instantaneous basis. Figure 2.5C shows that Atlantic precipitation actually *decreases* in the season with more TOA insolation.

The simulated seasonal precipitation response mostly derives from changes in the mean circulation, in particular changes in atmospheric divergence (see Appendix A). This is in contrast to the findings of Merlis et al. (2013), who in an aquaplanet simulation with slab ocean and fixed clouds attributed a precessionally induced ITCZ shift to thermodynamic processes. Our results therefore show the importance of continents, dynamic ocean processes and cloud changes in driving the tropical precipitation response to precession. In our simulations, seasonal temperature and precipitation changes over the continents play a key role in driving precipitation changes over the Atlantic ocean

(Fig. 2.6).

Temperature changes over northern Africa in boreal spring and summer (Fig. 2.7A) lead to wind changes over the North Atlantic (Fig. 2.7B), which through changes in the latent heat flux (Fig. 2.9D) set up an anomalous SST gradient (Fig. 2.8C) that affects the *position* of the ITCZ (Fig. 2.5C). This boundary layer mechanism is amplified by the WES-feedback (Fig. 2.9D) and changes in equatorial ocean heat transport (Fig. 2.9F). Under maximum precession, continental temperatures in boreal spring and summer decrease in response to a reduction in TOA insolation, strengthening the trades, reducing the meridional SST gradient, and keeping the ITCZ south. These processes are illustrated in the upper panel of Fig. 2.6. Similar mechanisms do not operate in boreal fall and winter, when TOA insolation forcing is stronger over the Southern Hemisphere (Fig. 2.2B). This is because continental temperatures over southern Africa show a weaker response to insolation forcing (compare Fig. 2.7A to 2.11B) and oceanic winds are particularly sensitive to continental forcing over the North Atlantic (Chiang et al., 2001, Xie & Saito, 2001). This asymmetric seasonal change in ITCZ position leads to an annual mean change in Atlantic ITCZ position.

Continental monsoon changes and their associated diabatic forcing alter the stability of the troposphere and impact the *intensity* of precipitation over the ocean. Figure 2.6 shows schematically how under maximum precession, precipitation over the African continent decreases in boreal spring and summer (Fig. 2.7B), increasing precipitation over the Atlantic ocean (Fig. 2.10). In boreal fall and winter, P_{MAX} precipitation over southern Africa and South America increases (Fig. 2.11B), leading to a reduction in oceanic precipitation (Fig. 2.12). Because the continental precipitation response to precessional forcing is stronger in JJA than in DJF (Table 2.2), the annual mean response is skewed towards this season. It should be noted that we are analyzing a strongly coupled system, which means that without additional sensitivity experiments we cannot conclusively prove our proposed path of causality. However, further diagnosis using the F_{NET} framework of Neelin & Held (1987) (not shown) supports the idea that changes in moisture convergence over the continent are a direct response to shortwave forcing, unlike oceanic precipitation changes which are indirectly forced.

Direct comparison of our modeling results with paleoproxies is precluded by the fact that there

are no long proxy records representing oceanic precipitation over the Atlantic. Reconstructions of continental precipitation over Africa and South America confirm our finding that continental precipitation follows the summer hemisphere with more insolation (Gasse, 2000, DeMenocal et al., 2000, Fritz et al., 2004, Wang et al., 2004b, Cruz et al., 2005, Wang et al., 2007, Weldeab et al., 2007, Tjallingii et al., 2008). A sediment record from Cariaco Basin (Deplazes et al., 2013) is interpreted as reflecting shifts in ITCZ, but these occur mostly on millennial timescales. In our model, Cariaco Basin is not very sensitive to the phases of precessional forcing compared here. A reconstruction of ITCZ position by Arbuszewski et al. (2013) suggests that the ITCZ shifted northward during the mid-Holocene, which would be in line with our findings. However, their reconstruction only goes back to the LGM, so further comparisons cannot be made. During MIS 2 and 3, when precessional forcing was weak, and the climate system was in a glacial state with strong global cooling, high-latitude (millennial) forcing likely dominated over the local precessional response.

Our results show that while orbital TOA insolation forcing is the same at all longitudes, regional responses are strongly zonally asymmetric as a result of interactions between terrestrial processes, oceanic changes and remote influences. They illustrate the importance of considering the seasonality of climatic forcings, even when studying annual mean climate change.

Part II

Rectification mechanisms at high latitudes

CHAPTER 3

Nonlinear response of the Antarctic ice sheet to Quaternary sea level and climate forcing

The Antarctic ice sheet (AIS) has varied substantially during the Late Quaternary, contributing more than 10 m to glacial sea level drop and losing an estimated 3–6 m sea level equivalent (SLE) ice volume during warm interglacials. With its large marine margins, the AIS is sensitive to oceanic as well as atmospheric forcing, but the relative contributions of Quaternary climate forcings remain poorly constrained, with previous modeling studies relying heavily on parameterizations of past climate evolution. Here we present results from simulations with an Antarctic ice sheet model over the past 408,000 year, forced with spatially and temporally varying climate anomalies from a transient climate simulation, in addition to reconstructions of global sea level change. The simulated AIS variability has a glacial-interglacial amplitude of 10–12 m SLE. Sensitivity experiments in which atmospheric, ocean temperature and sea level forcing are applied individually show that the full ice sheet response is a non-linear superposition of the individual drivers. Sea level and atmospheric temperature changes are the most important pacemakers of glacial inception and termination, with both atmospheric greenhouse gases and precessionally-driven long summer lengths contributing to deglacial surface melt peaks. When we include a number of recently proposed instability mechanisms to our model simulations, parts of the AIS collapse during warm interglacials such as Marine Isotope Stage (MIS) 5e and MIS 9. In this case, atmospheric pre-conditioning from CO_2 and precessional forcing enhances calving rates and grounding line retreat. Whereas the validity and sensitivity of these mechanisms still requires further investigation, our study demonstrates that the seasonal and spatial evolution of various types of climate forcings are important in determining the overall ice sheet response.

Based on: Tigchelaar, M., Timmermann, A., Pollard, D., Friedrich, T. & Heinemann, M. (in preparation) Nonlinear response of the Antarctic ice sheet to Quaternary sea level and climate forcing. *The Cryosphere*.

3.1 Introduction

Recent observations of accelerated Antarctic mass loss (Rignot et al., 2011, Paolo et al., 2015) have raised concerns over the future stability of the Antarctic Ice Sheet (AIS) and its contribution to future global sea level rise (Joughin & Alley, 2011). But the opposing effects of rising temperatures on accumulation and oceanic melt rates (Hellmer et al., 2012, Frieler et al., 2015), combined with uncertainties in projected climate change and ice sheet dynamics, create widely ranging sea level rise estimates (Church et al., 2013). Studying the past evolution of the AIS advances our understanding of the sensitivity of the Antarctic mass balance to various climatic forcings, i.e., changes in atmospheric temperature, accumulation rates, oceanic conditions and sea level. Reconstructions of ice sheet extent indicate a diachronous retreat of the AIS after the Last Glacial Maximum (LGM) ~20,000 years ago (20 ka), when the grounding line of much of the AIS extended to the continental shelf break (Bentley et al., 2014). This implies that spatial differences in climatic drivers and ice sheet dynamics were important for the Quaternary evolution of the AIS (Golledge et al., 2012). However, due to the nature of geological and glaciological methods, reconstructions of AIS evolution are limited in spatial extent and temporal resolution. Other studies have tried to deduce Antarctic ice volume changes from far-field sea level records, but the Antarctic contribution to interglacial sea level highstands (Dutton et al., 2015) and rapid sea level rise during deglaciations (Carlson & Clark, 2012) – and thus its sensitivity to external forcing – remains poorly constrained. Modeling past AIS variability can help provide such constraints and address how different forcing agents interact on centennial to multi-millennial time scales.

Unlike the Greenland ice sheet, the Antarctic ice sheet has large marine-based margins, meaning that it interacts with the marine as well as the atmospheric environment. The accelerated mass loss of Pine Island Glacier during the past few decades for instance, has been attributed to enhanced sub-shelf melting in response to warming oceans and changing ocean circulation (Jacobs et al., 2011, Pritchard et al., 2012). The collapse of the Larsen B ice shelf in 2002 on the other hand, is thought to be the result of pre-conditioning by a warming atmosphere (van den Broeke, 2005). The Antarctic

ice shelves have a buttressing effect on the grounded ice sheet, and thus play an important role in determining the stability of the AIS. Disintegration of ice shelves can lead to rapid discharge from and acceleration of the grounded ice sheet, in particular when the bed deepens towards the ice sheet interior (a process referred to as 'marine ice sheet instability') (Schoof, 2007, Joughin & Alley, 2011). At the same time, future projections of AIS evolution suggest that in a warming world, accumulation rates will increase as a result of increased atmospheric moisture content, leading to growth of in particular the East Antarctic ice sheet (EAIS) (Huybrechts et al., 2004, Frieler et al., 2015). During the glacial cycles of the Late Quaternary, an additional driver was at play: Changes in eustatic sea level (Fig. 3.1C) affect the ice flux at the grounding line, turning grounded ice into floating ice for rising sea level, and vice versa. Previous modeling studies of Quaternary AIS evolution have identified global sea level as an important pacemaker, especially for the West Antarctic ice sheet (WAIS) (Ritz et al., 2001, Huybrechts, 2002, Pollard & DeConto, 2009).

Quaternary climate change is driven by variations in earth's axial tilt and orbit around the sun (Milankovitch, 1941) – precession, eccentricity and obliquity (Fig. 3.1A,B) – and changes in atmospheric greenhouse gas concentrations, primarily CO_2 (Fig. 3.1C) (Shackleton, 2000). Different climate variables respond differently to each of these forcings, resulting in a rich spectrum of Southern Hemisphere climate variability in both reconstructions (e.g., Steig et al., 2000, Gersonde et al., 2005, Cortese et al., 2007, Jouzel et al., 2007, Ho et al., 2012) and modeling studies (e.g., Huybers & Denton, 2008, Menviel, 2008, Timmermann et al., 2009, He et al., 2013, Timmermann et al., 2014). Until now however, efforts to model the long-term evolution of the Antarctic ice sheet have included climate information of limited detail. Previous studies have either used heavily parameterized climate forcing (Ritz et al., 2001, Huybrechts, 2002, Pollard & DeConto, 2009) or simplified climate and ice sheet configurations (de Boer et al., 2012, Stap et al., 2014); have focused on equilibrium simulations of specific time periods (Golledge et al., 2012); or apply indexed interpolations of extreme climate states (Maris et al., 2015). All of these studies assume that Southern Hemisphere climate variables vary in pace with either Antarctic temperature reconstructions (Petit et al., 1999) or the benthic oxygen isotope record (Lisiecki & Raymo, 2005). They thus ignore the spatial and temporal heterogeneity of Quater-

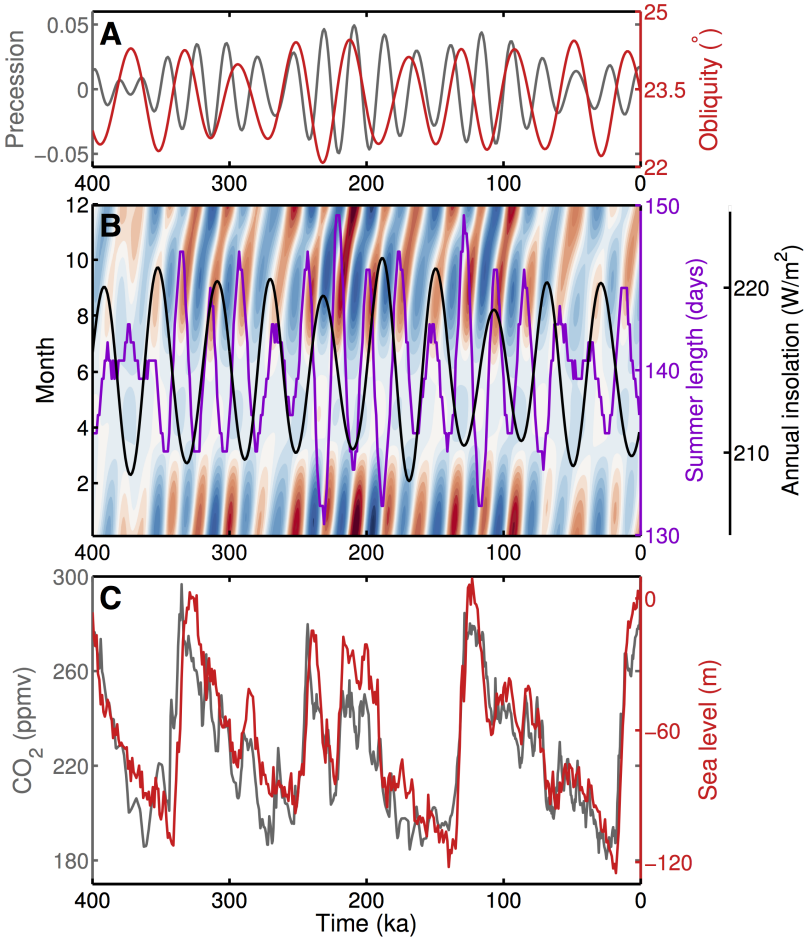

Figure 3.1: Climate drivers over the last 400 ka – (A) precession ($e\sin(\omega)$, where e is eccentricity, $\omega = \pi + \tilde{\omega}$ and $\tilde{\omega}$ is the angle between the vernal equinox and perihelion (Paillard, 2001); grey) and obliquity (red) (Laskar et al., 2004); (B) monthly insolation anomalies (colors, contours ranging from ±65 W m^{-2}), annual mean insolation (black) and summer length (days with insolation >250 W m^{-2} (Huybers & Denton, 2008); purple) at 65 °S as a result of the orbital forcing in (A) (Laskar et al., 2004); (C) atmospheric CO_2 concentration (grey; Lüthi et al., 2008) and global sea level (m) scaled from Lisiecki & Raymo (2005) according to Eq. 3.4.

nary climate variability, and show a high dependency on the details of the forcing parameterizations (e.g., Pollard & DeConto, 2009).

The aim of this study is to better understand the roles of sea level and climate variability in driving Antarctic ice sheet evolution during the Late Quaternary. To that end we have forced a state-of-the-art Antarctic ice sheet model with spatially-varying and time-evolving atmospheric temperature, precipitation and ocean temperature fields from a climate model simulation over the last four glacial

cycles, as well as changes in eustatic sea level from Northern Hemisphere ice sheets. In addition, we conduct a number of sensitivity experiments exploring the isolated role and superposition of individual forcings and mechanisms contributing to past ice sheet instabilities. Section 3.2 provides a detailed overview of our climate and ice sheet modeling setup. In Sect. 3.3 the main results are presented, with Sect. 3.3.1 discussing Quaternary climate variability, Sect. 3.3.2 showing the contributions from individual drivers and Sect. 3.3.3 discussing contributions to interglacial ice sheet retreat. Section 3.4 concludes this paper with a discussion and summary of our main findings.

3.2 Methods

The Late Quaternary orbital and greenhouse gas forcing shown in Fig. 3.1 is used to drive a transient simulation with an Earth system model of intermediate complexity (EMIC) over the last four glacial cycles (Sect. 3.2.1). Climate anomalies from this simulation together with time-varying global sea level (Fig. 3.1C) are then used as boundary conditions for various sensitivity experiments (Sect. 3.2.2) with the Penn State University Antarctic ice sheet model (Sect. 3.2.2) according to the equations outlined in Sect. 3.2.2. Figure 3.2 shows a schematic illustrating this modeling setup.

3.2.1 Climate model

Our ice sheet model experiments are driven with transient climate anomalies spanning the last four glacial cycles (408 ka to present; Timmermann et al., 2014), derived from a simulation with the Earth system model of intermediate complexity (EMIC) LOVECLIM (Goosse et al., 2010), which consists of coupled atmospheric, ocean-sea ice and vegetation components. The atmospheric component of LOVECLIM, ECBILT, is a spectral T21 (~5.625°×5.625°), three-level model based on the quasi-geostrophic equations extended by estimates of the ageostrophic terms (Opsteegh et al., 1998). The model contains a full hydrological cycle and includes physical parameterizations of diabatic processes (radiative fluxes, sensible and latent heat fluxes) in the thermodynamic equation.

CLIO, the ocean sea-ice component, is a 3°×3°primitive equation ocean general circulation model with twenty vertical levels, coupled to a thermodynamic-dynamic sea ice model (Goosse & Fichefet, 1999). It uses parameterizations to compute mixing along isopycnals, the effect of mesoscale eddies on diapycnal transport and downsloping currents at the bottom of continental shelves. Finally VECODE is a terrestrial vegetation model that consists of two plant functional types and non-vegetated desert zones (Brovkin et al., 1997). Each grid cell is assumed to be partially covered by these three land cover types, based on annual mean temperature and rainfall amount and variability.

For the transient climate model simulation, LOVECLIM was forced with time-evolving orbital parameters (Berger, 1978) and reconstructed atmospheric greenhouse gas concentrations (CO_2, CH_4 and N_2O) (Lüthi et al., 2008). The corresponding orbital forcing, annual mean and seasonal insolation changes and CO_2 time series are shown in Fig. 3.1. In addition, Northern Hemisphere ice sheet conditions were obtained from a transient experiment conducted with the Climate and Biosphere Model, version 2 (CLIMBER-2), coupled to the Northern Hemisphere Simulation Code for Polythermal Ice Sheets (SICOPOLIS) ice sheet model (Ganopolski & Calov, 2011). Orography, albedo and ice mask variations from this simulation are interpolated onto the LOVECLIM grid, where in the presence of land ice, the grid point albedo is set to 0.7 and the vegetation mask is modified. The orography, albedo and ice mask of the Antarctic ice sheet remain constant throughout the simulation.

The orbital, greenhouse gas and ice sheet conditions are applied with a boundary acceleration factor of 5 (Timm & Timmermann, 2007, Timmermann et al., 2014). This means that 200 model years correspond to 1000 calendar years. The LOVECLIM simulation is conducted using Last Glacial Maximum (LGM) ocean bathymetry (Roche et al., 2007) in order to avoid the internally generated Atlantic meridional overturning circulation oscillations described in Friedrich et al. (2010). The present-day climate sensitivity of the model version used here is 2 °C per CO_2 doubling. Our climate modeling strategy is illustrated in the top half of Fig. 3.2.

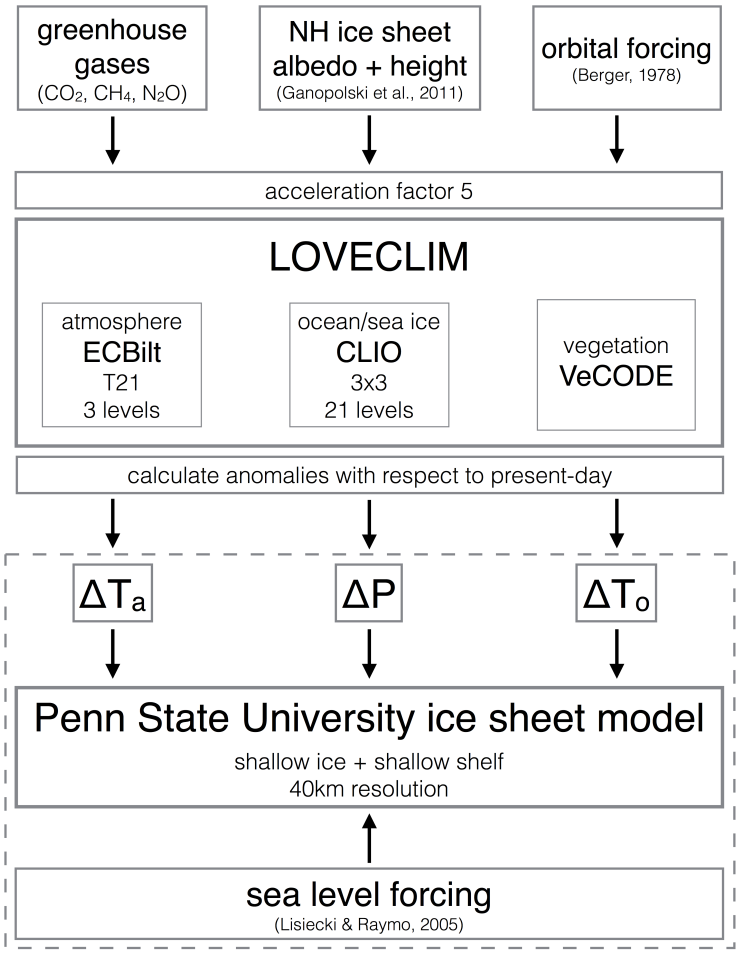

Figure 3.2: Schematic illustrating the modeling setup as described in Sect. 3.2.

3.2.2 Ice sheet model

The 408 ka climate anomalies from LOVECLIM are used to force a number of sensitivity experiments with an Antarctic ice sheet model developed at Penn State University (Fig. 3.2; Pollard & DeConto, 2012b, Pollard et al., 2015). This model is based on a combination of the scaled shallow ice and shallow shelf approximations, and calculates the position of the grounding line using an ice flux parameterization (Schoof, 2007). Basal sliding is calculated using a standard drag law, with the basal sliding coefficients derived from a simple inverse method (Pollard & DeConto, 2012a). Bedrock deformation is modeled as an elastic lithospheric plate above local isostatic relaxation; the equilib-

rium bedrock state is taken to be modern observed (Bedmap2; Fretwell et al., 2013). The model is discretized on a polar stereographic grid, which for our long sensitivity experiments has a 40 km resolution.

Present-day climate forcing

For modern climate, surface input fields are obtained from the ALBMAP v1 database at 5 km resolution (Le Brocq et al., 2010). First, annual mean atmospheric temperature T_a^{obs} (Fig. 3.3A; van de Berg et al., 2006) and accumulation P^{obs} (Fig. 3.3B; Comiso, 2000) are interpolated onto the ice model grid. Then a lapse rate correction of $\gamma = 0.008$ °C m^{-1} is applied to the atmospheric temperature to correct for differences between observed (z^{obs}; Le Brocq et al., 2010) and model (z) surface elevation. The seasonal cycle in atmospheric temperature is parameterized as a sinusoidal cycle with a range of 20 °C at sea level, increasing linearly with elevation to 30 °C at 3000 m and above (Pollard & DeConto, 2012b), giving $T_a^{obs}(\tau)$. Surface melt rates are calculated using a positive degree-day (PDD) scheme (Reeh, 1991) that uses different coefficients for ice (8 kg m^{-2} °C^{-1}) and snow (3 kg m^{-2} °C^{-1}) and allows for seasonal refreezing as well as diurnal and synoptic variability (Pollard & DeConto, 2012b). Present-day accumulation rates in the model do not contain a seasonal cycle, but are split into rain and snow based on monthly temperatures.

While in reality melting at the ice shelf-ocean interface is a function of ocean temperature, salinity and circulation in the ice shelf cavity (Jacobs et al., 1992), most ice sheet models used for long-term simulations make use of parameterizations based on sub-surface ocean temperatures alone. This ice model follows the parameterization developed by Martin et al. (2011) for the PISM-PIK model, where oceanic melt is a function of the difference between ocean temperature and the depth-varying freezing temperature of ocean water. Unlike Martin et al. (2011), the melt rate dependency on this temperature difference is quadratic (Holland et al., 2008, Pollard & DeConto, 2012b). For modern conditions, the model interpolates annual mean 400 m-depth ocean temperatures T_o^{obs} from the World Ocean Atlas (Locarnini et al., 2010) onto the ice sheet model grid (Fig. 3.3C). In areas outside the range of the

Locarnini et al. (2010) dataset, ocean temperatures are propagated underneath the ice shelves using a nearest neighbor interpolation. In addition, melt rates at vertical ice faces in direct contact with the ocean are calculated by multiplying the area of each vertical face with the oceanic melt rates at that grid point. Calving rates at the ice shelf edge are parameterized based on the large-scale stress field, represented by the horizontal divergence of the ice shelf (Pollard & DeConto, 2012b, Nick et al., 2013).

Recently a new set of parameterizations was introduced to the ice sheet model representing sub-grid scale processes that have been hypothesized to significantly increase the sensitivity of the Antarctic ice sheet to climatic forcing (Pollard et al., 2015). These parameterizations include increased calving due to hydrofracture by surface melt and rainfall draining into crevasses (Nick et al., 2013), as well as structural failure at the grounding line when the vertical face of ice cliffs is too tall ('cliff failure') (Bassis & Walker, 2012). Combined, these two mechanisms have the potential to significantly reduce ice shelf extent and buttressing in warm climates. Because these parameterizations still require further validation against physical process studies, they are not included in our main simulations. However, we have performed a sensitivity experiment with these mechanisms to test their possible contribution to past interglacial sea level high stands (Dutton et al., 2015) (see Table 3.1; Sect. 3.2.2).

The mass balance terms in this study are calculated from a file written at run time that stores accumulation (snow+rain), total ablation (abl), oceanic melt (ocn), melting at vertical ocean faces (face) and calving (calv), averaged over the entire ice sheet area. The residual ablation, i.e., abl - ocn - face - calv, represents the combined contributions of evaporation at the surface, melting at the base of the ice sheet, and percolation of rain, surface melt water and frictional melt water to the base of the ice sheet, minus refreezing in the ice column. Evaporation and basal melting are both very minor, and surface melt dominates the percolation term; therefore we refer to the residual ablation term as 'surface melt'.

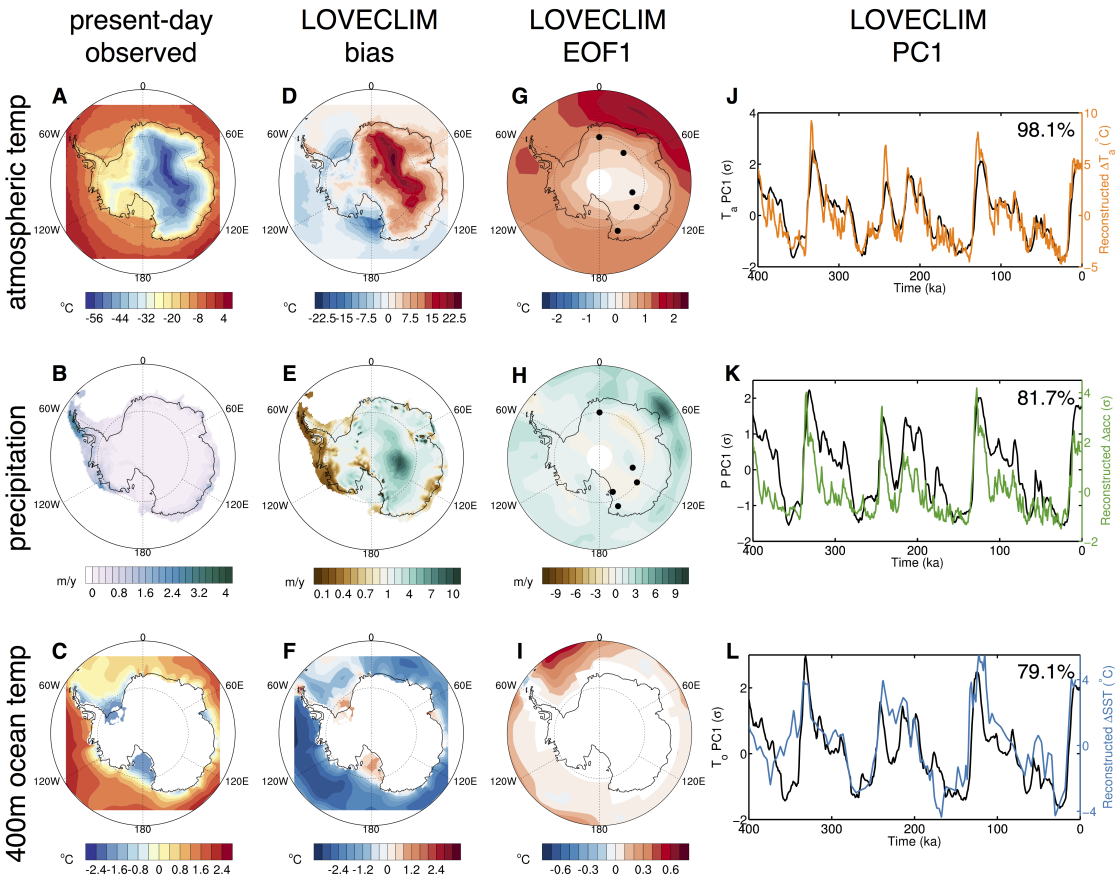

Figure 3.3: Climate forcing on the ice model grid – (left) Present-day climate conditions (Locarnini et al., 2010, Le Brocq et al., 2010), (second from left) LOVECLIM bias with respect to present-day climate, (third from left) first EOF and (right) first PC1 in LOVECLIM for (top) annual mean atmospheric temperature, (middle) annual mean accumulation (observed) and precipitation (LOVECLIM) and (bottom) annual mean ocean temperature at 400 m depth. For annual mean temperature the LOVECLIM temperatures were first adjusted to observed elevations (Le Brocq et al., 2010) using a lapse-rate correction of 0.008 °C m^{-1}. The atmospheric and ocean temperature biases are plotted as LOVECLIM–observed, while the precipitation bias is plotted as LOVECLIM/observed. In addition, (J) shows a composite of reconstructed temperature anomalies from ice cores (°C, orange; locations indicated by black dots in (G); Parrenin et al., 2013), (K) shows a composite of reconstructed accumulation anomalies from ice cores (σ, green; locations indicated by black dots in (H); Steig et al., 2000, Bazin et al., 2013, Vallelonga et al., 2013) and (L) shows reconstructed SST anomalies at 80 °W, 54 °S (°C, blue; Ho et al., 2012). Percentages in (J)-(L) indicate percent variance explained by the first principal component.

Climate and sea level forcing over the last 408 ka

Previous simulations of Antarctic ice sheet evolution through the Late Quaternary with the Penn State ice sheet model have used spatially homogeneous parameterizations of paleo-climate based on

the benthic oxygen isotope record of Lisiecki & Raymo (2005) and 80 °S summer insolation (Pollard & DeConto, 2009, 2012b). These parameterizations thus assume that atmospheric temperature, precipitation and ocean temperature all vary in concert with each other and global climate, with summer insolation pacing seasonal variability. While these simulations have helped to reveal the range of past Antarctic variability, their strong assumptions about the timing of climate forcing preclude an evaluation of the contribution of individual drivers to the global sea level record. For this reason, instead of parameterizing the paleo-climate forcing of the Late Quaternary, we force the Penn State ice sheet model with climate anomalies from the 408 ka transient experiment described in Sect. 3.2.1.

The climate anomalies are calculated with respect to the LOVECLIM climatology over the last 200 model years (representing 1000 calendar years) and are applied and updated every 1000 ice sheet model years. For atmospheric temperature T_a, a lapse rate correction of $\gamma = 0.008$ °C m^{-1} is applied to correct for differences between LOVECLIM orography z^{LC} and present-day Antarctic elevation (z^{obs}; Le Brocq et al., 2010), in addition to differences between present-day elevation and elevation at time t (z(t)). Subsequently, monthly temperature anomalies are added to the present-day temperature field (Fig. 3.3A; Sect. 3.2.2):

$$\begin{aligned} T_a(t,\tau) = {} & T_a^{obs}(\tau) - \gamma \times \left(z(t) - z^{obs} \right) \\ & + \left(T_a^{LC}(t,\tau) - T_a^{LC}(0,\tau) \right) - \gamma \times \left(z^{LC} - z^{obs} \right), \end{aligned} \tag{3.1}$$

where t indicates time in years, τ represents month of year, γ is the lapse rate and superscripts 'obs' and 'LC' indicate present-day and LOVECLIM climatologies respectively.

Because the ice sheet model does not include a seasonal cycle for present-day precipitation, precipitation anomalies are calculated with respect to annual mean precipitation. Instead of adding the anomalies to the present-day field, as done for atmospheric temperature, present-day precipitation (P^{obs}) is multiplied with the ratio of monthly LOVECLIM precipitation at time t ($P^{LC}(t,\tau)$) to present-

day LOVECLIM precipitation ($P^{LC}(0)$):

$$P(t,\tau) = P^{obs} \times \left(\frac{P^{LC}(t,\tau)}{P^{LC}(0)} \right). \tag{3.2}$$

This is done to ensure that precipitation rates do not go below zero. Annual mean ocean temperature anomalies from the 400 m depth level in LOVECLIM are added to the ice model field as

$$T_o(t) = T_o^{obs} + \left(T_o^{LC}(t) - T_o^{LC}(0) \right). \tag{3.3}$$

The ocean temperature is set not to decrease below the freezing temperature of sea water, which is -2.18 °C at 400 m depth with a salinity of 34.5 psu (Beckmann & Goosse, 2003).

Figures 3.3D-F show the differences between LOVECLIM and observed present-day climate. Modeled atmospheric temperatures over the Antarctic ice sheet are too high, even when corrected for differences in observed surface elevation and the T21 spectral representation of Antarctic orography in LOVECLIM (Fig. 3.3D). Present-day Antarctic precipitation is characterized by a temperature-driven low accumulation regime (<50 mm y^{-1}) over the Antarctic interior and much higher precipitation rates in coastal areas (>1000 mm y^{-1}) as a result of cyclonic activity and topographic uplift. LOVECLIM does not capture the complex coastal topography of Antarctica well, and therefore underestimates coastal precipitation, distributing it over the ice sheet interior instead (Fig. 3.3E; Maris et al., 2012).

Table 3.1: Overview of the sensitivity experiments described in Sect. 3.2.2

experiment	description
full	all forcings (Eqs.3.1, 3.2, 3.3, 3.4)
atm	only atmospheric forcing (Eqs. 3.1 & 3.2)
ocn	only ocean temperature forcing (Eq. 3.3)
sl	only sea level forcing (Eq. 3.4)
sl+atm	sea level and atmospheric forcing (Eqs. 3.1, 3.2, 3.4)
sl+ocn	sea level and ocean temperature forcing (Eqs. 3.3 & 3.4)
atm+ocn	atmospheric and ocean temperature forcing (Eqs. 3.1, 3.2, 3.3)
cliff+hydro	as 'full', but with cliff and hydrofracture instabilities (Sect. 3.2.2)
param	climate forcing parameterized as in Pollard & DeConto (2012b) (Eq. 3.5)

Sub-surface ocean temperatures in LOVECLIM are generally too low in the Southern Ocean, except underneath the shelves, where they are higher than in the World Ocean Atlas climatology. The lower LOVECLIM temperatures might be related to the fact that for present-day climate, minimum sea ice extent is overestimated (Roche et al., 2012). It should also be noted however that the observed climatology in the Southern Ocean is based on a relatively low number of observations, especially close to the Antarctic continent (Locarnini et al., 2010). In any case, LOVECLIM climate anomalies rather than the full fields are applied to the ice sheet model to avoid the propagation of LOVECLIM biases into the ice sheet evolution. As will be discussed in Sect. 3.3.1, in spite of climate model biases, LOVECLIM simulates the Quaternary climate evolution reasonably well.

In addition to climate anomalies, the ice sheet model is forced with time-evolving sea level. Sea level variations are derived from the linearly interpolated benthic δ^{18}O record of Lisiecki & Raymo (2005), where δ^{18}O at the LGM (20 ka) is taken to equal a sea level drop of 120 m:

$$z_{sl}(t) = \frac{-120}{\delta^{18}O(LGM) - \delta^{18}O(0)} \times \left(\delta^{18}O(t) - \delta^{18}O(0)\right) \tag{3.4}$$

The resulting sea level time series is plotted in Fig. 3.1C. While the climate fields are updated every 1000 years, sea level evolves continuously. The bottom half of Fig. 3.2 illustrates how the climate anomalies and sea level are used to drive the ice sheet model.

Sensitivity experiments

The main ice sheet model simulation is run for 408 ka and includes all drivers described in Sect. 3.2.2 (experiment 'full'). In order to isolate the effects of these individual external forcings on Antarctic ice sheet variability and their interaction, we have performed an additional series of sensitivity experiments that include only one or multiple drivers. The individual drivers are either the atmospheric forcing described by Eqs. 3.1 and 3.2, the ocean temperature forcing of Eq. 3.3 or the sea level variations from Eq. 3.4 (experiments 'atm', 'ocn' and 'sl', respectively). In addition to these singular forcing experiments, the model is forced with combinations of two of these three forcings (experiments

'sl+atm', 'sl+ocn' and 'atm+ocn').

To compare the performance of the ice sheet model forced with spatially-varying model-derived climate anomalies against the original paleo-climate parameterization schemes (Sect. 3.2.2) we have also conducted a 408 ka experiment using the climate parameterizations of Pollard & DeConto (2012b) (experiment 'param'). In this simulation, surface temperature anomalies are based on the Lisiecki & Raymo (2005) benthic oxygen isotope record, with an additional influence of 80 °S annual mean insolation, Q^{80}_{ann}. Precipitation anomalies are directly scaled to changes in temperature:

$$T_a(t,\tau) = T_a^{obs}(\tau) - \gamma \times \left(z(t) - z^{obs}\right) - 10 \times \left(\frac{\delta^{18}O(t)}{\delta^{18}O(0)}\right) + 0.1 \times \left(Q^{80}_{ann}(t) - Q^{80}_{ann}(0)\right) \tag{3.5a}$$

$$P(t) = P^{obs} \times 2^{0.1\times(T_a(t)-T_a(0))} \tag{3.5b}$$

Ocean temperatures at 400 m in this run derive from a deglaciation run using the Community Climate System Model (Liu et al., 2009). In addition, ocean temperatures are increased by up to 2 °C when 80 °S summer insolation is high, and melt rates are strongly reduced when benthic $\delta^{18}O$ is close to the LGM value. See Pollard & DeConto (2012b) for more details.

Finally, we run an experiment 'cliff+hydro' with all of the external drivers (as in 'full') that includes the cliff and hydrofracture mechanisms of Pollard et al. (2015) (Sect. 3.2.2). All sensitivity experiments are summarized in Table 3.1.

3.3 Results

3.3.1 Late Quaternary climate forcing

The spatial and temporal evolution of atmospheric temperature, precipitation and sub-surface ocean temperatures is characterized by the first principal component (PC1) and the corresponding spatial pattern (EOF1) as shown in Fig. 3.3G-L. As can be seen in Fig. 3.3J, annual mean surface temperatures

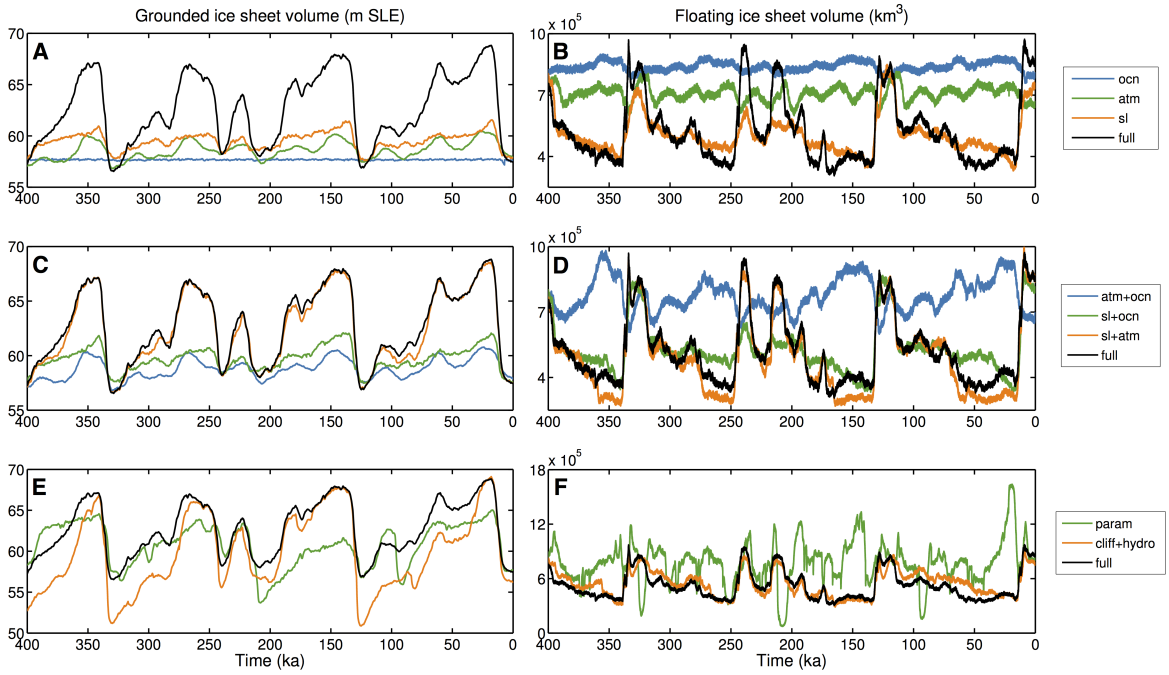

Figure 3.4: Ice sheet evolution over the last 400 ka in the various experiments listed in Table 3.1 – (left) grounded ice sheet volume in m SLE; (right) floating ice sheet volume in km^3; for (top) 'ocn' (blue), 'atm' (green), 'sl' (orange) and 'full' (black); (middle) 'atm+ocn' (blue), 'sl+ocn' (green), 'sl+atm' (orange) and 'full' (black); and (bottom) 'param' (green), 'cliff+hydro' (orange) and 'full' (black).

over Antarctica are predominantly paced by changes in atmospheric CO_2 (Fig. 3.1C). Timmermann et al. (2014) showed that obliquity also contributes to annual mean temperature changes, by affecting annual mean insolation (Fig. 3.1B) and modulating the strength of the Southern Hemisphere westerlies. The dominant pattern of annual mean temperature changes is homogenous, with higher amplitudes towards the equator, especially over the Indian Ocean sector of the Southern Ocean (Fig. 3.3G). When compared to a composite of temperature reconstructions from ice cores (Parrenin et al., 2013), the temporal evolution of the LOVECLIM PC1 is very similar, but the amplitude is underestimated by a factor of ~2. This is due to the fact that the LOVECLIM climate sensitivity is too low (Tachikawa et al., 2014). In addition to annual mean temperatures, surface ablation rates are sensitive to changes in seasonal insolation, either through maximum summer insolation or the length of the summer season (Huybers & Denton, 2008, Huybers, 2009). Both of these variables are

precessionally driven and shown in Fig. 3.1B.

Precipitation changes display a time evolution very similar to that of the atmospheric temperature PC1 (Fig. 3.3K), confirming that temperature is the dominant driver of precipitation over Antarctica. When compared to a composite of ice core accumulation reconstructions (Steig et al., 2000, Bazin et al., 2013, Vallelonga et al., 2013), LOVECLIM is shown to overestimate precipitation rates during early glacial times. Steig et al. (2000) describe how when the Antarctic ice sheet is expanding, the coastal ice core locations switch from a cyclonic-driven precipitation regime to one driven by temperature with increasing distance from the ice edge. The local precipitation evolution captured by the ice cores thus differs from the large-scale evolution captured by the principal component analysis. This ice sheet-climate feedback is not included in our LOVECLIM simulations.

The temporal evolution of sub-surface ocean temperatures in LOVECLIM (Fig. 3.3L) is similar to that of surface (not shown) and atmospheric temperatures (Fig. 3.3J). To our knowledge no reconstructions of intermediate water temperatures in the Southern Ocean exist, so we compare against a long sea surface temperature (SST) record from 54 °S (Ho et al., 2012). Both in our model simulation as well as in reconstructions, Southern Ocean SST variability is closely related to changes in sea ice area and production, explaining why there is substantial precessional variability in these time series (Timmermann et al., 2009). The LOVECLIM-simulated ocean temperature anomalies close to the Antarctic continent are very small, with the exception of the Weddell sector. The effect of this possible underestimation of ocean forcing on ice sheet evolution will be discussed further below.

3.3.2 Response to individual drivers

Figure 3.4 shows the simulated response of Antarctic grounded and floating ice volume to the individual and combined Late Quaternary forcings over the last four glacial cycles. With all forcings combined ('full'), the glacial-interglacial difference in ice volume is 10–12 m sea level equivalent (SLE) (Fig. 3.4A). Interglacial floating ice volume is more than double the glacial value (Fig. 3.4B). In our simulations, previous interglacials only contribute 1–2 m to global sea level, with the deepest

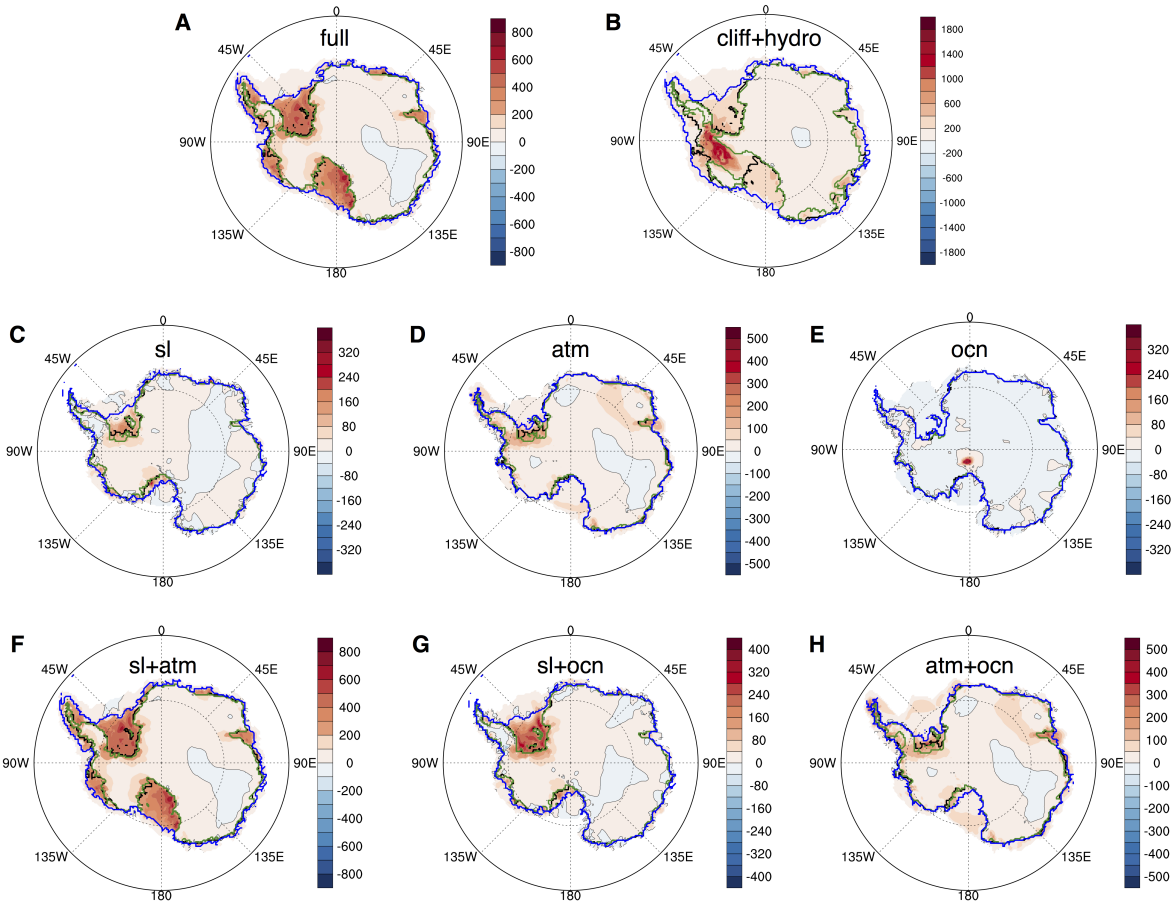

Figure 3.5: Dominant spatial pattern (first EOF) of ice sheet thickness variability (m) and minimum (green), maximum (blue) and present-day (black) grounding line extent for (A) 'full', minimum at 331 ka, maximum at 18 ka; (B) 'cliff+hydro', minimum at 125 ka, maximum at 18 ka; (C) 'sl', minimum at 121 ka, maximum at 18 ka; (D) 'atm', minimum at 331 ka, maximum at 350 ka; (E) 'ocn', minimum at 7 ka, maximum at 156 ka; (F) 'sl+atm', minimum at 331 ka, maximum at 20 ka; (G) 'sl+ocn', minimum at 122 ka, maximum at 140 ka; (H) 'atm+ocn', minimum at 330 ka, maximum at 354 ka.

interglacial occurring at 330 ka (MIS 9).

The dominant spatial pattern of ice sheet thickness variability in the 'full' simulation, along with minimum (331 ka) and maximum (18 ka) grounding line extent, are shown in Fig. 3.5A. At its maximum extent, the grounding line reaches to the continental shelf break in all areas except a small section of the Bellingshausen sea. The minimum grounding line extent over the last 408 ka is very similar to present-day, with retreat mostly in the West Antarctic Peninsula. Changes in ice sheet thickness

are most pronounced in those regions where the grounded ice sheet expands, in particular the Ross and Weddell sectors, Amundsen Sea and Amery shelf. In the interior of the AIS, thickness changes are generally smaller, but mostly of the same sign, with the exception of a small region of the East Antarctic ice sheet (EAIS) where ice sheet thickness decreases during glacial times.

Not one of the individual drivers of Quaternary AIS variability – sea level, atmospheric temperature and precipitation, ocean temperatures – can single-handedly explain the full ice volume evolution (Fig. 3.4A, B). Moreover, all of the individual forcings combined only account for about two thirds of the total changes, suggesting that the drivers add nonlinearly. The largest contribution in terms of grounded ice volume comes from the sea level forcing (Fig. 3.4A), closely followed by the atmospheric forcing. When individual forcings are combined, sea level and atmospheric forcing together explain most of the changes in grounded ice volume (Fig. 3.4C). The situation is different for floating ice, where sea level changes are responsible for most of the variability (Fig. 3.4B).

Sea level forcing

Sea level changes drive changes in Antarctic ice volume by affecting the ice sheet thickness at the grounding line, thus altering the outflow of ice and converting grounded to floating ice or vice versa (Schoof, 2007). In addition to the ~100 ka glacial period, the sea level curve over the past 400 ka (Fig. 3.1C) shows substantial orbital variability. However, when sea level is the only forcing, little of this sub-100ka variability is found in the ice sheet response (Fig. 3.4A,B). As seen in Fig. 3.5C, the AIS predominantly responds to sea level forcing in the Weddell sector, where the glacial maximum grounding line attains almost its full extent. In the Ross sector on the other hand, the sea level forcing alone is not sufficient to significantly move the grounding line towards the continental shelf break. The expansion of grounded ice happens at the cost of floating ice (Fig. 3.4A,B). Figure 3.6 plots grounded ice sheet volume in the Ross and Weddell sectors against the sea level forcing. In the 'sl' run, the grounding line in both sectors is sensitive to sea level changes from 0-20 m, after which the sensitivity strongly reduces. The Weddell sector in this run shows additional grounding line

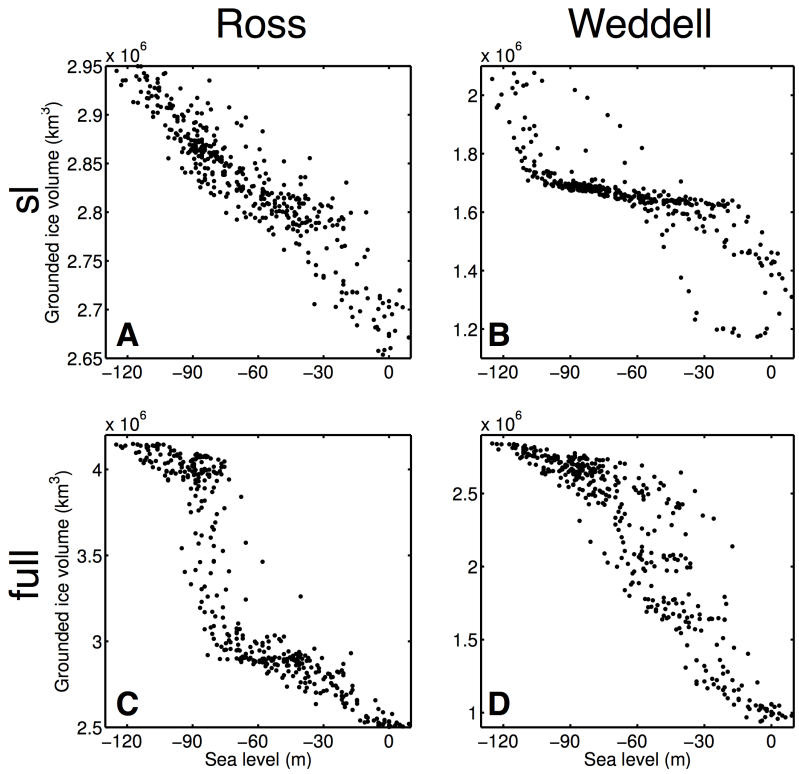

Figure 3.6: Grounded ice volume (km^3) vs. sea level forcing (m) for (top) 'sl' experiment; (bottom) 'full' experiment; in (left) Ross sector; and (right) Weddell sector.

sensitivity when sea level drops below 110 m (Fig. 3.6B). It is interesting to note that the ice sheet response to sea level forcing in this region shows strong hysteresis: during retreat, the grounding line mostly responds in the 40–80 m sea level drop range.

Figure 3.7 shows the various ice sheet averaged mass balance terms for the full and individual forcing simulations. With sea level as the only driver, the climate-driven mass balance terms (accumulation, ablation, melt at the ice-ocean interface) all act as feedback terms. As the primary ice sheet response to sea level drop is to convert floating ice to grounded ice, ice sheet average oceanic melt reduces during glacial times (Fig. 3.7C), with melt rates underneath the floating ice staying roughly the same (not shown). This provides a positive feedback on equatorward grounding line migration, allowing the ice sheet to thicken and grow. The resulting areal expansion pushes the ice sheet into regions where on average temperatures (Fig. 3.3A) and precipitation rates (Fig. 3.3B) are

higher. Consequently, ice sheet averaged accumulation (Fig. 3.7A) and surface melt rates (Fig. 3.7B) increase, acting as positive and negative feedbacks respectively. Overall the accumulation increase and ocean melt decrease are larger than the increase in surface melt, explaining why ice sheet thickness increases during glacial times in response to sea level forcing alone (Fig. 3.4D).

Atmospheric forcing

In response to isolated atmospheric forcing, grounded ice sheet volume increases during glacial maxima (Fig. 3.4A-B; Fig. 3.5D). The main driver for this is a sharp reduction in ice sheet average ablation rates (Fig. 3.7B) that results from a glacial decrease in annual mean temperature (Fig. 3.3D). In addition to annual mean temperature, changes in seasonal temperatures driven by the precessional cycle (Fig. 3.1A-B) strongly affect surface melt rates. When the summer season is long, there is more energy available for surface melt (Huybers & Denton, 2008), leading to sharp ablation peaks during these times (Fig. 3.7B). This precessional forcing is most notable in the evolution of the floating ice volume (Fig. 3.4B), which fringes the Antarctic perimeter where average temperatures are higher (Fig. 3.3A) and most of the surface melt occurs. As a result, most of the thickness changes in the 'atm' run happen in these coastal areas as well (Fig. 3.5D).

Strikingly, the ice volume changes in the 'atm' run contain substantially more variability at the 41 ka obliquity period than the first principal components of the atmospheric drivers (Fig. 3.3D,H). This obliquity variability originates from a strong obliquity pacing of ice sheet averaged accumulation rates, as seen in Fig. 3.7A. Although not picked out by the EOF analysis, a similar obliquity component is found in the ice sheet averaged precipitation forcing from LOVECLIM (not shown), and is probably related to changes in moisture convergence resulting from changes in the Southern Hemisphere westerlies (Timmermann et al., 2014). As surface melt rates drop in response to decreasing CO_2 levels (Fig. 3.7B), the ice sheet margins expand into regions that have climatologically higher precipitation (Fig. 3.3B), while over the rest of the ice sheet accumulation rates decrease in response to changing climate (Fig. 3.3H). The opposing effects of this areal expansion and climate forcing on ice sheet

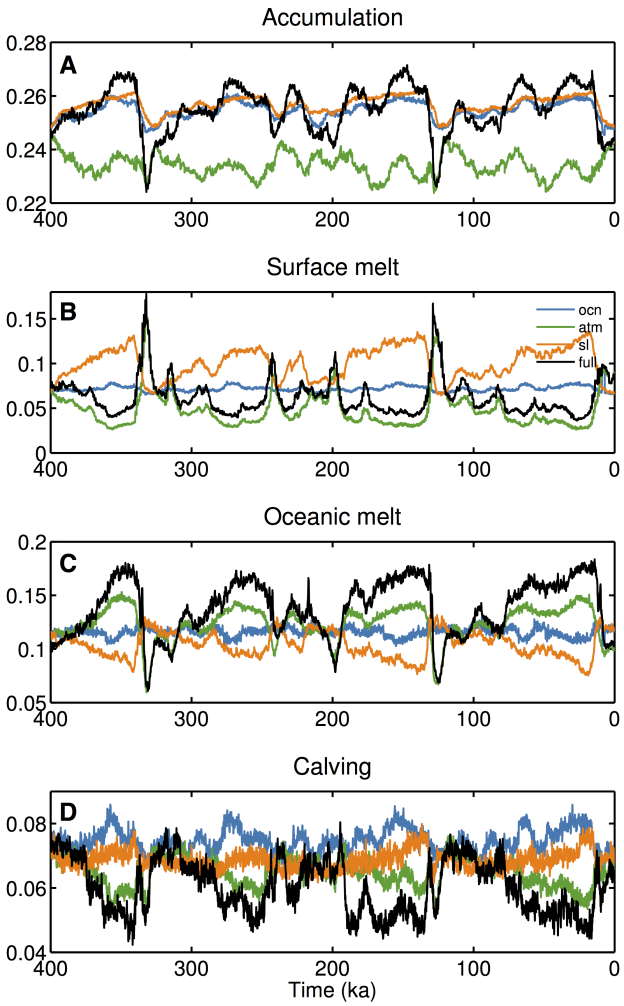

Figure 3.7: Ice sheet averaged mass balance terms (m y^{-1}) for experiments 'ocn' (blue), 'atm' (green), 'sl' (orange) and 'full' (black) – (A) accumulation, (B) surface melt, (C) oceanic melt and (D) calving.

average accumulation rates nearly balance, leading to the absence of strong 100 ka variability from the accumulation time series in Fig. 3.7A. Without ocean temperature forcing, ice sheet average ocean melt rates (Fig. 3.7C) vary in response to surface melt driven changes in floating ice volume (Fig. 3.4B) and changing proximity to warm Circumpolar Deep Water (CDW) (Fig. 3.3C).

Ocean temperature forcing

Out of the three individual drivers, the ocean temperature forcing by itself is the least effective, as evidenced by the minimal response in grounded and floating ice sheet volume resulting from this forcing (Fig. 3.4A,B). In fact, the dominant spatial pattern of ice thickness variability for the 'ocn' simulation is not driven by external forcing, but rather displays internally generated ice sheet variability in the Siple Dome region (Fig. 3.5E) with a period of ~10 ka (not shown). The reduction in glacial ocean temperatures does contribute to a small increase in floating ice (Fig. 3.4B), primarily in the Weddell sector (Fig. 3.5E), that again leads to a positive area-accumulation feedback, as described for other simulations above (Fig. 3.7A).

Combined forcing

The discussion above has indicated that the response of the AIS to (individual) external drivers is a nonlinear superposition of a direct mass balance response to climatic change, and internal feedbacks related to areal expansion and the conversion between grounded and floating ice. When forcings are combined, the seasonal temperature changes resulting from orbital and greenhouse gas forcing have the dominant impact on surface melt rates (Fig. 3.8B). Both the glacial drop in sea level and reduction in surface melt are necessary to allow glacial grounding lines to fully migrate to the continental shelf break (Fig. 3.5F). This is also illustrated by Fig. 3.6C and D, which shows that in the 'full' experiment, most of the ice sheet growth now happens between 70-90 m sea level drop in the Ross sector, and 40-60 m sea level drop in the Weddell region, coincident with reduced CO_2 levels (Fig. 3.1C) and annual mean temperatures (Fig. 3.3J). The relatively narrow range of sea level sensitivity in Fig. 3.6C and D is a result of the close co-evolution of the sea level and CO_2 forcing (Fig. 3.1C).

As evidenced by the similarity between ocean melt rate evolution in the 'full', 'atm' and 'sl+atm' runs (Figs. 3.7C and 3.8C), changes in melting at the ice-ocean interface are predominantly a result of the fact that the 'full' glacial ice sheet front is bathing in warmer ocean water (Fig. 3.3C). Therefore generally in our simulations, evolving ocean temperatures contribute little to ocean melt rate changes

(Fig. 3.8C), except in the Weddell sector, where decreasing ocean temperatures allow for further areal and grounding line migration during glacial times (Figs. 3.4D; 3.5). This low sensitivity to oceanic forcing is likely a result of the small range of LOVECLIM ocean temperature anomalies over the continental shelf (Fig. 3.3I), although a similar dependence of glacial oceanic melt rates on grounding line position rather than climate forcing was also found by Kusahara et al. (2015). During deglaciations, there are sharp peaks in ocean melt rates in all multiple forcing simulations, with the exception of the one excluding sea level forcing ('atm+ocn'; Fig. 3.8C). This is due to the fact that rising global sea level during deglaciations converts grounded ice to floating ice, leading to an increase in the overall contribution of oceanic melting to the total mass balance (as evidenced for sea level forcing alone ('sl') in Fig. 3.7C). Accumulation changes in the 'full' simulation (Fig. 3.7A) are opposite in trend to the precipitation forcing (Fig. 3.3K), which means that the climatic forcing – with the exception of the obliquity component described above – is secondary to the internal area-accumulation feedback described above.

Calving in the ice sheet model is a function of ice shelf divergence (Pollard & DeConto, 2012b, Pollard et al., 2015) and only responds indirectly to external forcing. It therefore shows the greatest nonlinearity with regard to individual Quaternary ice sheet drivers (Figs. 3.7D, 3.8D). Calving rates tend to be higher in ice shelves that are bound by coasts or pinned by islands versus ice shelves that are laterally unbound. This can be seen in the 'full' simulation, where calving rates are generally higher during warm periods, when most of the ice shelves are located in coastal embayments, and lower during cold periods, when they fringe the continental perimeter. The deglacial calving peaks that can be seen in the 'full' simulation are only found in experiments that include atmospheric forcing (Figs. 3.7D, 3.8D) and result from thinning of the ice shelves due to strong surface melt (Fig. 3.7B, 3.8B).

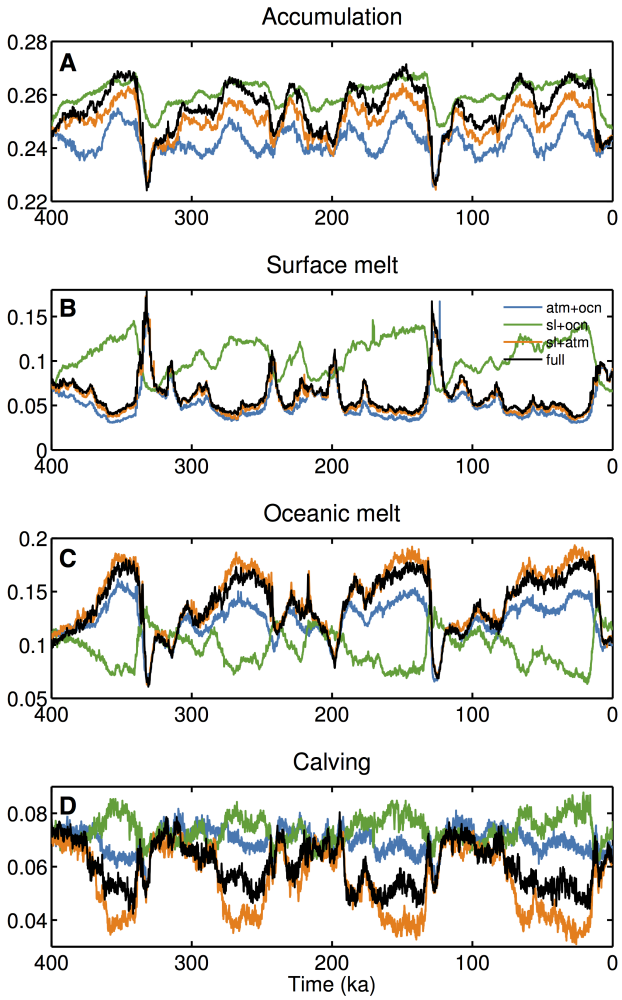

Figure 3.8: Ice sheet averaged mass balance terms (m y^{-1}) for experiments 'atm+ocn' (blue), 'sl+ocn' (green), 'sl+atm' (orange) and 'full' (black) – (A) accumulation, (B) surface melt, (C) oceanic melt and (D) calving.

3.3.3 Ice shelf instabilities

It has been suggested that the simplified or hybrid treatments of ice dynamics used in studies of ice sheet evolution on time-scales of 10^3–10^6 year do not sufficiently capture the processes leading to a strongly reduced AIS in warm climates (Alley et al., 2005). Pollard et al. (2015) therefore applied a set of parameterizations that simulate hydrofracturing due to surface melt and structural failure at the grounding line (Sect. 3.2.2, Table 3.1). Using these parameterizations the authors were able to generate substantial grounding line retreat for very warm climates. Here we test how these

mechanisms might have contributed to interglacial sea level highstands in the Late Quaternary by adding these parameterization to the standard 'full' run.

As can be seen in Figs. 3.4E and 3.5B, the glacial AIS in this 'cliff+hydro' simulation is very similar to that in the 'full' experiment. During MIS 5e and 9 on the other hand, grounded ice volume is reduced by 5–6 m SLE as a result of substantial grounding line retreat in both the East and West Antarctic ice sheet. The hydrofracturing parameterization increases calving of floating ice when surface melt rates are high (Nick et al., 2013, Pollard et al., 2015). This means that calving rates in the 'cliff+hydro' simulation increase during periods of high CO_2 and long summer length, in line with the discussion on surface melt rates above. The ensuing removal of buttressing ice shelves causes a rapid acceleration of the grounded ice sheet and wide-spread retreat of the grounding line due to marine ice sheet instability. This grounding line retreat is accelerated by the cliff instability mechanism. Figure 3.9 shows the accumulated calving flux and grounding line retreat over the period 133–127 ka (MIS 5e). The additional parameterizations in the 'cliff+hydro' run do not alter the evolution of the Ross and Weddell shelves much, but have significant impact in the Bellingshausen and Amundsen sectors, as well as in the Wilkes Land area. Retreat beyond the 'full' interglacial grounding line occurs rapidly (<2,000 year), and slightly earlier in the EAIS than in the WAIS.

3.3.4 Climate forcing vs parameterization

The results presented in this study differ from earlier long-term modeling studies of the Antarctic ice sheet in that they use two-dimensional, temporally evolving forcing fields for atmospheric temperature, precipitation and sub-surface ocean temperatures. Previous work used spatially homogeneous forcing based on paleoclimatic reconstructions for at least one, if not all, of these fields. To assess the effects of changing the climate forcing methodology, we compare our results against a simulation ('param') with the same ice sheet model, forced with the parameterizations described in Pollard & DeConto (2012b) (Sect. 3.2.2, Table 3.1).

The glacial Antarctic ice sheet is between 3 (350 ka) and 7 (140 ka) m SLE smaller in the 'param'

run than in the 'full' one (Fig. 3.4E). At certain times, in particular at 325 ka, 210 ka and 90 ka the 'param' grounded ice volume is much reduced compared to the 'full' simulation, accompanied by strong reductions in floating ice volume (Fig. 3.4F). These periods of reduced ice volume are indicative of a partial collapse of the WAIS (not shown). Overall, the floating ice volume using parameterized climate is more variable, and generally higher during cold climate periods (Fig. 3.4F).

These pronounced differences between the 'full' and 'param' simulations are the result of three main differences between the forcing functions. Firstly, in the run with parameterized climate forcing, changes in precipitation rates are exponentially scaled to temperature anomalies (Eq. 3.5) that are larger than the temperature anomalies simulated by our climate model (Fig. 3.3D). As a result, ice sheet averaged accumulation rates in 'param' decrease during cold climates, leading to a smaller glacial grounded ice sheet (not shown). Secondly, glacial oceanic melt rates are much lower in 'param' than in 'full' due to lower ocean temperatures and an artificial cold climate melt rate reduction (Sect. 3.2.2), leading to an increase in glacial floating ice volume (Fig. 3.4F). Most of this floating ice however does not buttress the grounded ice sheet, so the peaks in floating ice volume are not matched by peaks in grounded ice volume. Both of these differences are examples of situations where in the 'full' simulation internal feedbacks outweighed the climate forcing, but where in the 'param' run the opposite is the case. Finally, Pollard & DeConto (2012b) hypothesized a strong dependency of in particular ocean melt rates on 80 °S summer insolation, i.e., precession. Indeed, the grounded and floating ice volume reductions in Fig. 3.4E,F correspond to periods of high precession (Fig. 3.1A,B). As a result, the 'param' ice sheet minima are not in phase with those in the 'full' simulation, in which interglacials are jointly paced by long summer length and Northern Hemisphere ice sheet evolution.

3.4 Discussion and Conclusions

In this study we presented results from simulations of Antarctic ice sheet evolution over the past 408 ka. In contrast to previous work, which used parameterized forcing, climate anomalies (atmospheric temperature, precipitation and sub-surface ocean temperatures) were directly derived from

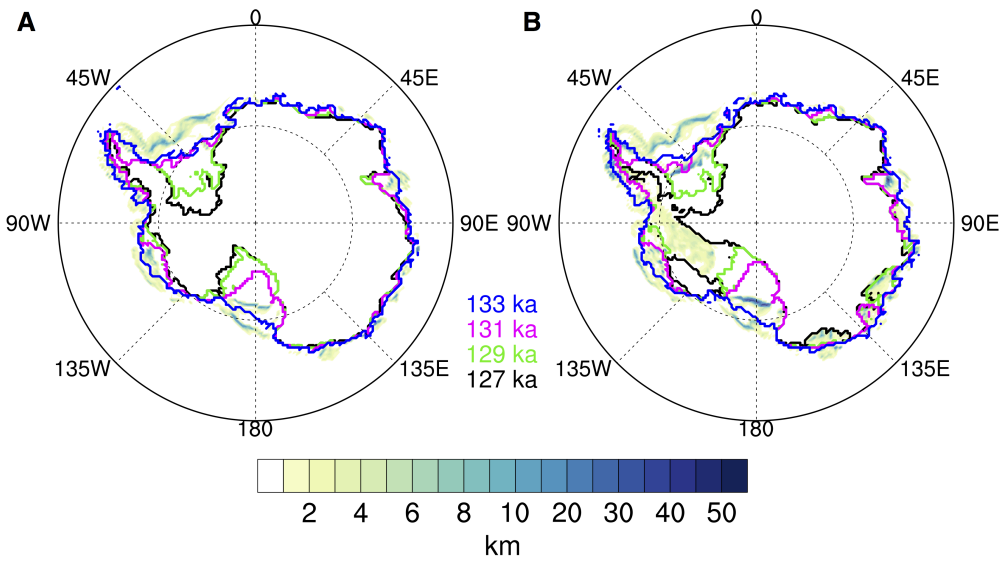

Figure 3.9: Total ice loss as a result of calving over the period 133–127 ka (km; shading) and grounding line position at 2 ka intervals (lines) for (A) 'full' simulation, and (B) 'cliff+hydro' simulation.

a transient simulation with the EMIC LOVECLIM. The simulated AIS has a glacial-interglacial amplitude of 10–12 m SLE, with the glacial grounding line extending almost entirely to the continental shelf break, and past interglacials showing limited retreat of 1–2 m SLE. Sensitivity experiments where atmospheric, oceanic and sea level forcing were applied in isolation or in pairs, showed that the combined effect of individual forcings is strongly nonlinear. In our simulations, sea level and atmospheric forcing together explain most of the full response, both in terms of amplitude and pacing. Partial or full retreat of the WAIS is only attained when additional instability mechanisms are included.

One of our main findings is that the evolution of the AIS mass balance is a combination of a direct response to external drivers and internal regulating mechanisms based on grounding line position and ice sheet area. The most direct response to climatic forcing is found for the surface melt term: reduced surface melt rates in response to reduced annual mean temperatures allow for glacial expansion, while surface melt peaks at times of high CO_2 and long summer length contribute substantially to deglaciations, in phase with Northern Hemisphere summer insolation and global sea level rise. Such

an important role for summer length was also postulated by e.g., Huybers & Denton (2008). Previous studies however did not find a strong surface melt contribution to glacial terminations, because they did not include the seasonal evolution of Late Quaternary surface temperatures, or because they interpolated climate forcing between extreme climate states with little precessional forcing (the LGM, used e.g., by Maris et al. (2014), has a precessional value very similar to that of present-day (Fig. 3.1A). Pollard & DeConto (2009) and Pollard & DeConto (2012b) hypothesized a dependence on 80 °S summer insolation, which put their WAIS retreat out of phase with global interglacials. Our climate anomaly forcing method did not have to make such assumptions, and was thus able to independently confirm the role of summer length as a pacemaker of Antarctic deglaciation.

In the case of accumulation, our simulations found internal feedbacks to dominate over climatic forcing: as the glacial grounding line migrates towards regions with higher average accumulation, ice sheet averaged accumulation rates increase, despite the fact that precipitation rates decrease locally. This contrasts previous modeling studies of AIS evolution that generally find accumulation changes to contribute negatively to ice sheet growth (Ritz et al., 2001, Huybrechts, 2002, Pollard & DeConto, 2009, Maris et al., 2014). The EMIC LOVECLIM, with its low atmospheric horizontal and vertical resolution and simplified dynamics, does not represent precipitation over Antarctic very well, particularly the circulation over the complex coastal topography. Furthermore, our climate simulations did not included time-evolving orographic and albedo boundary conditions for the Antarctic continent. It might thus be that the amplitude of precipitation changes in LOVECLIM is underestimated. On the other hand, previous modeling studies that parameterized accumulation changes based on surface temperatures (Ritz et al., 2001, Huybrechts, 2002, Pollard & DeConto, 2009) also do not include climate-ice sheet feedbacks and contain a certain degree of arbitrariness. Verification against ice core reconstructions is precluded by the fact that no long-term accumulation records exist for regions that were grounded ice sheet in the past, but are floating ice shelf presently. Maris et al. (2014) calculated the surface mass balance over the AIS at the LGM using a regional climate model forced with LGM boundary conditions and ICE-5G topography. In that study the surface mass balance over the grounded ice sheet is reduced during glacial times, suggesting our study might have underestimated

the effect of climatic forcing on accumulation.

Similar to the passive evolution of accumulation rates, the contribution of melting at the ice-ocean interface to the total ice sheet mass balance opposes the climatic forcing, increasing during glacial times as a result of the grounding line being closer to warm CDW. This finding might be due to the generally low climate sensitivity in LOVECLIM, although a study by Kusahara et al. (2015) with a much more advanced and high-resolution ocean-ice sheet model also found increased oceanic melt rates during the LGM. Mackintosh et al. (2013) in a reconstruction of the deglacial history of the EAIS attribute much of the EAIS retreat to rising ocean temperatures. An additional caveat to our findings is that in reality, melting at the ice-ocean interface depends on much more than sub-surface ocean temperatures alone. The blocking effects of sea ice formation (Hellmer et al., 2012), the role of winds in pushing warm waters onto the continental shelf (Thoma et al., 2008, Steig et al., 2012) and the complex geometry of ice shelf cavities (Jacobs et al., 2011, De Rydt et al., 2014) have all been found to be important in observational and modeling studies of current and future oceanic melting of the WAIS ice shelves. These processes can only be captured in fully coupled ocean-atmosphere-ice sheet simulations at high resolution, something that is currently not feasible for the long timescales of Quaternary climate evolution.

Periods of high global mean sea level during the Quaternary have been used to estimate future sea level projections (Overpeck et al., 2006, Dutton et al., 2015). In that context it is important to quantify the contribution of the AIS to past sea level highstands and the mechanisms driving retreat. Sea level budgets suggest that the AIS contributed several meters to global sea level during e.g., MIS 5e and MIS 11, but evidence for Quaternary AIS collapse is unfortunately scarce and the timing poorly constrained (Scherer et al., 1998). Pollard & DeConto (2009) simulated past WAIS collapse by imposing elevated ocean temperatures during periods of high CO_2 and 80 °S summer insolation (see Sect. 3.2.2), but the timing of their modeled collapse is out of phase with the global sea level record and the imposed ocean temperature anomaly might be unrealistically high (Ho et al., 2012). In our 'full' experiment, grounding line retreat is simulated during global interglacials in response to atmospheric greenhouse gases, precessionally extended summer length and Northern Hemisphere

sea level forcing. The resulting sea level contribution of 1–2 m for MIS 5e and MIS 9 is however less than estimated from sea level budgets. When the hydrofracturing and cliff instability mechanisms suggested by Pollard et al. (2015) are included, grounded Antarctic ice sheet volume is reduced by 5–6 m SLE during these interglacials, well within the range suggested by Dutton et al. (2015). In this case, grounding line retreat is the result of enhanced calving and accelerated flow that are driven by surface melt induced hydrofracturing, the collapse of unsupported cliffs and marine ice sheet instability. This scenario suggests atmospheric pre-conditioning rather than ocean temperature forcing could have driven Quaternary AIS collapse, much like the collapse of the Larsen A and Larsen B ice shelves in recent decades. The validity and sensitivity of these proposed mechanisms still needs to be tested using ice sheet models of higher complexity. Our results show that such studies – when used for past climates – should include seasonal as well as annual mean climate forcing.

The Antarctic ice sheet has the potential to contribute significantly to sea level rise in the future, as it might have in the past. We have forced an Antarctic ice sheet model with two-dimensional atmospheric temperature, precipitation and sub-surface ocean temperature anomalies over the last 408 ka together with global sea level forcing to assess the response of the AIS to past external forcing. Overall the AIS evolution is a balance between a direct response to external forcing and internal feedbacks dependent on grounding line position and ice sheet area. From a series of sensitivity experiments we find that the combined response to atmospheric, ocean and sea level forcing is highly non-linear, with sea level and atmospheric temperature forcing acting as the most important pacemakers. Substantial grounding line retreat of more than 2 m SLE in past warm climates does not occur with the current model setup, but interglacial grounded ice volume is reduced by 5–6 m SLE when additional instability mechanisms are included. Using climate forcing derived from a transient climate simulation rather than a homogeneous parameterization has highlighted the important role of summer length in driving past surface melt peaks, providing a physically based mechanism for atmospheric pacing of Antarctic ice sheet evolution.

CHAPTER 4

Mechanisms of Late Quaternary bipolar ice sheet synchronization

A growing body of evidence highlights the important contribution of the Antarctic ice sheet to the glacial cycles of the Late Quaternary. There is a remarkable synchronicity between Northern and Southern Hemisphere ice sheet changes, yet much debate remains regarding the origins of this bipolar coupling. To better understand the drivers of Antarctic ice sheet variability and the mechanisms linking ice sheet evolution in both hemispheres, we have forced an Antarctic ice sheet model with time-evolving sea level and climate anomalies over the last 800,000 years. The Northern Hemisphere sea level forcing strongly impacts Antarctic ice volume by driving changes in the grounding line position. This grounding line migration modulates the Antarctic response to other climatic drivers: for both accumulation and oceanic melt rates the changes in configuration of the grounded ice sheet dominate over the glacial-interglacial climate forcing. Surface melt rates peak when austral summers are long, especially during periods of high annual mean temperature corresponding to high CO_2. These melt peaks provide a critical contribution to Antarctic deglaciation and are in phase with Northern Hemisphere summer insolation. Our results show that on glacial timescales, Antarctica and the Northern Hemisphere ice sheets vary in unison, through their respective orbital forcings, changes in global sea level, and CO_2.

Based on: Tigchelaar, M., Timmermann, A., Pollard, D., Friedrich, T. & Heinemann, M. (in preparation) Mechanisms of Late Quaternary bipolar ice sheet synchronization. *Nature Communications*.

4.1 Introduction

The glacial cycles of the Late Quaternary, with their characteristic period of ~100,000 years (100 ka) (Shackleton, 2000, Lisiecki & Raymo, 2005) and corresponding global sea level changes of more than 120 m (Waelbroeck et al., 2002) remain one of the most elusive examples of climate dynamical behavior. They are marked by ice sheets growing and sea level dropping incrementally over 80–100 ka, followed by rapid ice sheet disintegration with the rate of global sea level rise at times exceeding 10 mm y^{-1} (Carlson & Clark, 2012). During some previous warm periods (interglacials) the polar ice sheets were smaller than present by 6–9 m sea level equivalent (SLE) ice volume (Dutton et al., 2015). While much of past glacial research has focused on the Northern Hemisphere, recent work attributes parts of these past sea level changes to variability of the Antarctic ice sheet (AIS) (Carlson & Clark, 2012, Golledge et al., 2014, Dutton et al., 2015, Marino et al., 2015). For instance, reconstructions of past AIS extent indicate that during cold periods (glacials), much of the grounding line extended to the continental shelf break and Antarctica contributed more than 10 m to glacial sea level drop (Denton & Hughes, 2002, Bentley et al., 2014) . During certain interglacials, the West Antarctic ice sheet (WAIS) collapsed partially or in its entirety (Scherer et al., 2008, McKay et al., 2012). Like the Northern Hemisphere ice sheets, the WAIS oscillated in the past with a periodicity of approximately 100 ka (Davies et al., 2012, McKay et al., 2012), pointing at a joint driver of high latitude ice sheet variability.

Despite this increasing appreciation for the Antarctic contribution to glacial cycles, much uncertainty remains regarding the precise timing and amplitude of AIS changes and their synchronicity with Northern Hemisphere ice sheet changes. In particular, there is an ongoing discussion whether Antarctic climate and the AIS have evolved mostly in response to local forcing or whether they are forced by the remote northern high latitudes (Huybers, 2009, Timmermann et al., 2009, Denton et al., 2010, He et al., 2013). Several mechanisms have been put forward that couple the two hemispheres: Changes in *eustatic sea level* that result from Northern Hemispheric ice sheet evolution strongly impact the grounding line position of the Antarctic ice sheet (Ritz et al., 2001, Huybrechts, 2002,

Schoof, 2007, Pollard & DeConto, 2009). At the same time, meltwater fluxes associated with northern ice sheet retreat alter the *global ocean circulation* and cause surface warming in the Southern Hemisphere (Huybers, 2009, Denton et al., 2010, He et al., 2013). *Atmospheric greenhouse gases* are well-mixed in the atmosphere and orchestrate synchronous climate variability in both hemispheres (Huybers, 2009, He et al., 2013). Finally, northern and southern polar climate respond differentially to *seasonal insolation* changes, with Northern Hemispheric ice sheets responding strongly to summer insolation, while Antarctic climate variables might be more sensitive to (fixed season) austral spring insolation (Timmermann et al., 2009) or, equivalently, summer length (Huybers & Denton, 2008). Northern Hemisphere summer insolation and Southern Hemisphere spring insolation/summer length vary in phase (Huybers & Denton, 2008, Huybers, 2009), resulting in locally forced but synchronous bipolar climate variability. The relative importance of these various mechanisms remains a topic of debate.

To better understand the drivers of AIS variability and bipolar linkages, we force a state-of-the-art Antarctic ice sheet model with realistic atmospheric temperature, precipitation and ocean temperature fields from climate model simulations of the last eight glacial cycles, as well as with changes in eustatic sea level from Northern Hemisphere ice sheets (see Methods). We identify the main drivers of Quaternary climate variability in the Southern Hemisphere and determine the dominant contributors to changes in the Antarctic mass balance. Sea level, CO_2 and summer length are all found to exert strong influence on AIS evolution, leading to bipolar ice sheet synchronicity through both remote and local forcing.

4.2 Methods

4.2.1 Transient climate model experiments

The climate model simulations of the last eight glacial cycles (784 ka to present) have been performed with LOVECLIM (Goosse et al., 2010), a three-dimensional Earth system model of intermediate

complexity (EMIC) that has been used extensively for simulations of present-day and paleo-climate. LOVECLIM consists of a quasi-geostrophic three-level atmospheric model at T21 spectral resolution, coupled to an ocean general circulation model with 3°x3°horizontal resolution and twenty vertical levels. The model includes a thermodynamic-dynamic sea ice model and terrestrial vegetation component. The transient experiments used here are an extension of experiments previously done for the last four glacial cycles (Timmermann et al., 2014). Using an acceleration factor of five (Timm & Timmermann, 2007), the climate model is forced with time-evolving orbital parameters (Berger, 1978), reconstructed atmospheric greenhouse gas concentrations (Lüthi et al., 2008) (CO_2, CH_4 and N_2O) and time-evolving ice sheets in the Northern Hemisphere (Ganopolski & Calov, 2011). The present-day climate sensitivity of the model version used here is 2 °C per CO_2 doubling.

4.2.2 Ice sheet model experiments

Climate anomalies from the LOVECLIM simulations are added onto the observed climatology to force an established ice sheet-shelf model that has been used for long-term simulations of past and future evolution of the Antarctic ice sheet (Pollard & DeConto, 2012b, Pollard et al., 2015). This model uses a hybrid combination of the scaled shallow ice and shallow shelf approximations, and calculates the position of the grounding line using an ice flux parameterization (Schoof, 2007). The model is run at 20 km resolution, and initialized by running it to equilibrium with present-day climate conditions (Locarnini et al., 2010, Le Brocq et al., 2010, Pollard & DeConto, 2012b). After initialization, the model is forced with time-evolving sea level scaled to the benthic $\delta^{18}O$ record (Lisiecki & Raymo, 2005) (where the Last Glacial Maximum at 20 ka corresponds to a sea level drop of 120 m) along with anomalies of monthly-mean atmospheric temperature and precipitation fields and annual mean 400 m ocean temperatures. These anomalies are calculated with respect to the climatology over the last 200 LOVECLIM model years (representing 1000 climate years), interpolated to the ice sheet model grid. The atmospheric and ocean temperature anomalies from the climate model are added directly to the present-day fields in the ice sheet model (Locarnini et al., 2010, Le Brocq et al.,

2010, Pollard & DeConto, 2012b), while for precipitation the present-day ice sheet model values (Le Brocq et al., 2010) are multiplied with the ratio of past to present-day precipitation in the climate model. For atmospheric temperatures, a lapse-rate correction of 0.008 °C m^{-1} is applied to correct for differences between LOVECLIM orography and present-day Antarctic elevation (Le Brocq et al., 2010). The climate fields are updated every 1000 years, while sea level evolves continuously.

The mass balance terms in this study are calculated from a file written at run time that stores accumulation (snow+rain), total ablation (abl), oceanic melt (ocn), melting at vertical ocean faces (face) and calving (calv), averaged over the entire ice sheet area. The residual ablation, i.e., abl - ocn - face - calv, represents the combined contributions of evaporation at the surface, melting at the base of the ice sheet, and percolation of rain, surface melt water and frictional melt water to the base of the ice sheet, minus refreezing in the ice column. Evaporation and basal melting are both very minor, and surface melt dominates the percolation term; therefore we refer to the residual ablation term as 'surface melt' in this manuscript.

4.3 Late Quaternary Antarctic climate variability

Changes in climate on glacial-interglacial time scales are externally driven by variations in earth's axial tilt and orbit around the sun (Milankovitch, 1941) – precession, eccentricity and obliquity – and further amplified by internal changes in atmospheric greenhouse gas concentrations, primarily CO_2 (Shackleton, 2000). Together these affect seasonal and annual mean insolation and radiative forcing (Fig. 4.1A) and drive long-term changes in global climate. To quantify their role in driving Antarctic ice sheet variations we conducted an 800 ka transient climate model simulation using the earth system model LOVECLIM (Goosse et al., 2010, Timmermann et al., 2014). The simulated Southern Hemisphere climate variations, along with estimates of paleo-sea level changes (Lisiecki & Raymo, 2005), were then used to force the Penn State ice sheet model (Pollard & DeConto, 2012b, Pollard et al., 2015).

Ice sheets gain mass at the surface, and lose it through melting at the surface, at the ice-ocean

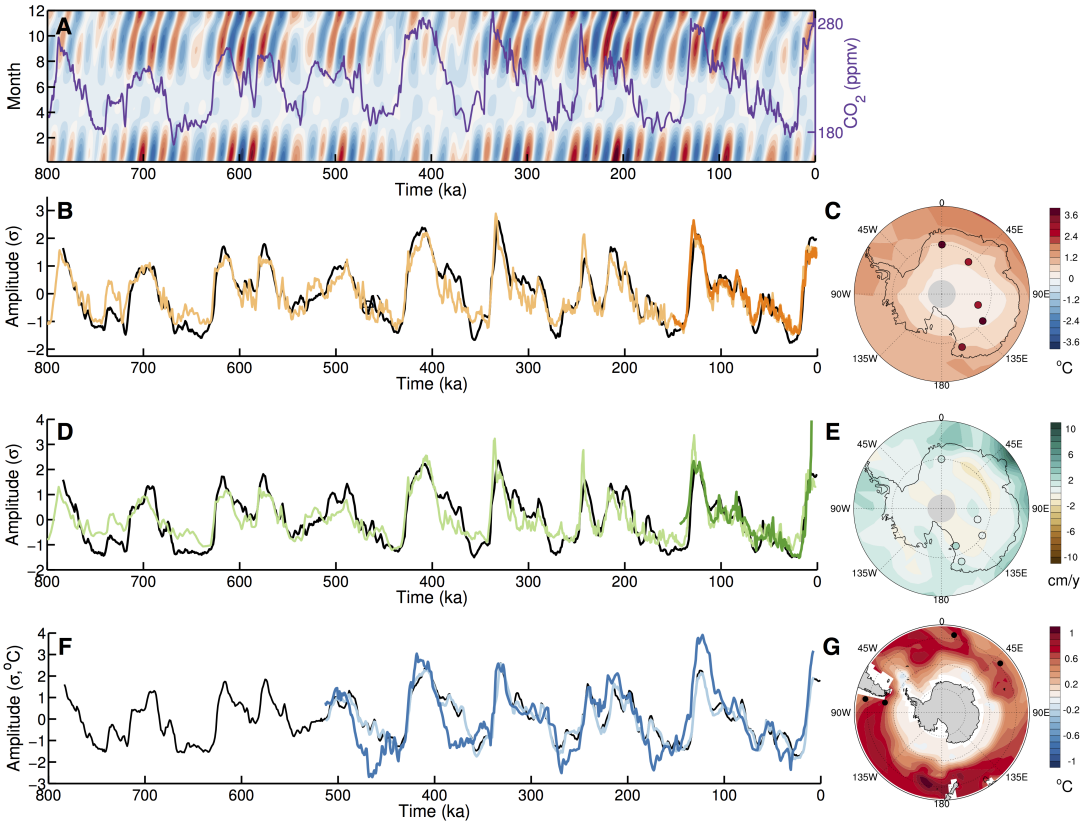

Figure 4.1: Southern Hemisphere climate response to Late Quaternary forcing – (A) daily insolation anomalies at 65 °S as a result of orbital forcing (Laskar et al., 2004) (shading; colors range from -65 to +65 W m^{-2}) and CO_2 concentrations (Lüthi et al., 2008) (purple) over the last 800 ka; (B) normalized PC1 of modeled annual mean atmospheric temperatures (black), normalized PC1 of reconstructed atmospheric temperatures at five ice core locations (Parrenin et al., 2004, EPICA Community Members, 2006, Jouzel et al., 2007, Kawamura et al., 2007, Stenni et al., 2011, Uemura et al., 2012) (dark orange) and normalized composite of Antarctic temperature reconstructions (Parrenin et al., 2013) (light orange); (C) EOF1 of modeled annual mean atmospheric temperatures (shading) and reconstructed atmospheric temperatures at five ice core locations (Parrenin et al., 2004, EPICA Community Members, 2006, Jouzel et al., 2007, Kawamura et al., 2007, Stenni et al., 2011, Uemura et al., 2012) (dots); (D) normalized PC1 of modeled annual mean precipitation (black), normalized PC1 of reconstructed accumulation at five ice core locations (Steig et al., 2000, Bazin et al., 2013, Vallelonga et al., 2013) (dark green) and normalized composite of Antarctic accumulation reconstructions (Steig et al., 2000, Bazin et al., 2013, Vallelonga et al., 2013) (light green); (E) EOF1 of modeled annual mean precipitation (shading) and reconstructed accumulation at five ice core locations (Steig et al., 2000, Bazin et al., 2013, Vallelonga et al., 2013) (dots); (F) normalized PC1 of modeled 400 m ocean temperatures (black), composite of modeled sea surface temperature anomalies (light blue) and composite of reconstructed sea surface temperature anomalies (dark blue) at four locations (Nürnberg & Groeneveld, 2006, Cortese et al., 2007, Martínez-Garcia et al., 2009, Ho et al., 2012); (G) EOF1 of modeled 400 m ocean temperatures (shading) and locations of sea surface temperature reconstructions in (F) (black dots).

or ice-bedrock interface, or through calving. Melting of ice at the surface only occurs when temperatures are above freezing, and therefore depends on annual mean and seasonal atmospheric temperatures (Reeh, 1991). Annual mean surface temperatures over Antarctica over the last eight glacial cycles are predominantly driven by changes in CO_2, with smaller contributions from obliquity (Timmermann et al., 2014). In the transient LOVECLIM simulation, the dominant spatial pattern of temperature variability is one where temperatures change uniformly over the Southern Hemisphere, with the lowest simulated amplitude over the interior of the ice sheet (Fig. 4.1C). The modeled timing of Antarctic temperature changes compares well to temperature reconstructions from ice cores (Parrenin et al., 2004, EPICA Community Members, 2006, Jouzel et al., 2007, Kawamura et al., 2007, Stenni et al., 2011, Uemura et al., 2012) (Fig. 4.1B), but the model underestimates the amplitude of observed changes, as characterized by the leading EOF mode of temperature anomalies (Fig. 4.1C). This is partially due to the fact that the earth system model experiment does not include Antarctic elevation gains during glacial times, but primarily because the model's climate sensitivity is known to be too low (Maris et al., 2012, Timmermann et al., 2014).

Present-day accumulation over the AIS is characterized by two regimes: In the interior of the ice sheet, snow-fall rates are low ($<$50 mm y^{-1}) and driven by temperature-induced changes in atmospheric moisture content (following Clausius-Clapeyron). Precipitation rates are much higher in coastal areas ($>$1000 mm y^{-1}), where they are related to cyclonic activity and topographic uplift (Bromwich, 1988). Reconstructions of past accumulation rates indicate that they closely follow atmospheric temperature changes (Fig. 4.1B,D), decreasing during glacial times, with higher glacial-interglacial amplitudes in coastal regions (Fig. 4.1E) (Steig et al., 2000, Bazin et al., 2013, Vallelonga et al., 2013). While our climate model simulation captures the timing of Antarctic precipitation changes well (Fig. 4.1D), this pattern of uniformly changing precipitation is not fully reproduced by the model, which simulates increased precipitation over parts of the Antarctic interior during glacial times (Fig. 4.1E). We attribute this model-data mismatch to the relatively low horizontal and vertical resolution and quasi-geostrophic physics of the atmospheric model, as well as to the fact that the topography of the AIS is not time-evolving in the atmosphere model (Maris et al., 2012).

Melting at the ice-ocean interface is a function of ocean temperature, salinity and circulation in the ice-shelf cavity at depths of 200-1000 m (Jacobs et al., 1992). However, both our climate and ice sheet model lack the required resolution and detailed physics to properly capture these processes, and most ice sheet models used for long simulations calculate oceanic melt rates as a function of sub-surface ocean (200-1000 m) temperature alone (Pollard & DeConto, 2012b). To our knowledge, no reconstructions of intermediate water temperatures close to Antarctica exist for model-data comparison, but in our model, temperature changes at intermediate depth closely follow those at the surface (Fig. 4.1F). Reconstructions of past sea surface temperatures (SSTs) show glacial-interglacial amplitudes of 8-10 °C at mid-latitudes, with lower amplitudes towards the pole and equator (Gersonde et al., 2005, Ho et al., 2012). As with atmospheric temperatures, our earth system model simulation underestimates the amplitude of Late Quaternary SST changes, but captures the timing well. In both reconstructions (Ho et al., 2012) as well as our climate simulation, Southern Ocean SST variability is closely related to sea ice variability, which responds to both changes in atmospheric greenhouse gases and spring insolation (i.e., precession) (Timmermann et al., 2009). The amplitude of temperature changes at intermediate depth is strongly reduced poleward of 60 °S due to the insulating effect of sea ice cover, as illustrated by the leading EOF pattern of simulated temperature changes at 400 m depth (Fig. 4.1G).

Late Quaternary annual mean climate in the Southern Hemisphere is thus predominantly driven by changes in CO_2, but with important differences between the various climate variables. The next section discusses how this climate variability combines with eustatic sea level forcing to drive Antarctic ice sheet evolution over the last 800 ka.

4.4 Climatic drivers of AIS evolution

Analyzing our ice sheet model simulation forced with climate anomalies and paleo-sea level, we find that the simulated glacial-interglacial difference in AIS volume over the last eight glacial cycles ranges from 8.7 m (Termination VIII, 710 ka) and 5.6 m (Termination VI, 520 ka) to 11.4 m (Termination

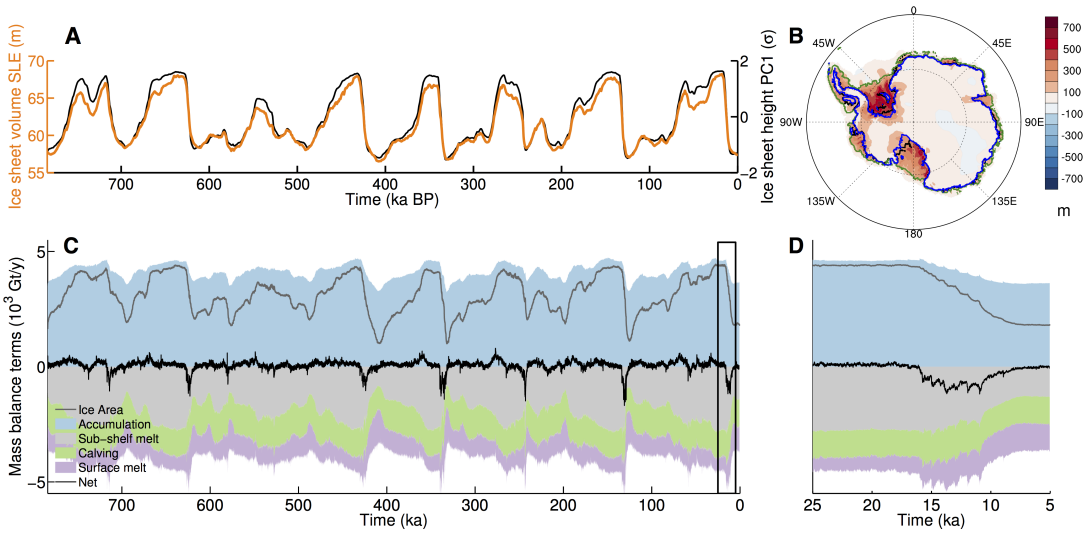

Figure 4.2: Evolution of the Antarctic ice sheet over the last eight glacial cycles – (A) normalized PC1 of ice sheet height (black) and ice sheet volume in meters sea level equivalent (orange); (B) EOF1 of modeled ice sheet height (shading), present-day (black), minimum (blue; 330 ka) and maximum (green; 20 ka) grounding line extent; (C) ice sheet integrated mass balance terms (shading; accumulation in blue, oceanic melt in grey, calving in green, residual ablation (see Methods) in purple) and net mass balance (black) in 10^3 Gt y^{-1}(10^3 Gt y^{-1}~ 0.03 Sv) and ice sheet area ranging from 14.2 to 17.5×10^6 km^2 (grey line); (D) same as (C), zoomed in on Termination I.

V, 420 ka) SLE (Fig. 4.2A). This compares well to previous model estimates of glacial-interglacial AIS volume change (Ritz et al., 2001, Huybrechts, 2002, Pollard & DeConto, 2009, Maris et al., 2015). The Antarctic ice sheet clearly evolves with a ~100 ka periodicity, with the largest variability in ice sheet height occurring over the WAIS, especially in the Weddell sector and the western part of the Ross embayment (Fig. 4.2B). Maximum glacial-interglacial ice thickness differences in these areas are >2000 m. By comparison, elevation changes over the interior East Antarctic ice sheet (EAIS) are very small and in some locations even of opposite sign.

During glacial maxima the grounding line extends to the continental shelf break almost everywhere (Fig. 4.2B). The Last Glacial Maximum grounding line position is generally in close agreement with reconstructions, though the latter place the grounding line in the Bellingshausen Sea and Wilkes Land areas somewhat further equatorward (Bentley et al., 2014). The minimum extent of the simulated grounding line over the eight glacial cycles is found at 330 ka and is very similar to present-day

grounding line extent. Antarctic ice volume decreased by only 1–2 m SLE during past warm interglacials, placing our simulations on the lower end of estimates of AIS contributions to interglacial sea level highstands (Dutton et al., 2015) (Fig. 4.2A).

The evolution of Antarctic ice volume is the sum of ice sheet integrated mass balance terms (Fig. 4.2C), with the net mass balance resulting from a delicate balance between generally large accumulation and ablation terms (see Methods for how these mass balance terms were calculated). Despite generally reduced precipitation rates in colder climates, ice sheet integrated accumulation increases towards glacial maxima as the area of the ice sheet increases. Remarkably, this increase in glacial accumulation is partially offset by a simultaneous increase in glacial oceanic melt rates: For present-day conditions, 37% of the negative mass balance terms derive from melt at the ice-ocean interface, 35% from calving and 26% from surface melt, but averaged over all glacial cycles this division is 52%, 33% and 15% respectively. Melting at the surface thus generally decreases during glacial build-up, and is marked by sharp peaks during terminations (Fig. 4.2D for Termination I). Rapid increases in calving rates also contribute to periods of deglaciation (Figs. 4.2D, B.1 & B.2). We now assess how these mass balance changes relate to the climatic drivers discussed previously.

Changes in eustatic sea level exert a substantial influence on the position of the grounding line (Ritz et al., 2001, Huybrechts, 2002, Pollard & DeConto, 2009). Dropping sea level converts floating ice to grounded and causes the grounded area of the AIS to expand until the limit of the continental shelf break is reached (Fig. 4.3A). While the impact of sea level on grounding line position does not directly appear in one of the mass balance terms (Schoof, 2007), it becomes apparent from the ice sheet average calving rate (Fig. 4.3B). Calving in the ice sheet model is primarily a function of the divergence of the ice shelf (Pollard & DeConto, 2012b, Pollard et al., 2015), which tends to be lower in ice shelves that are laterally unbound. Therefore calving is generally reduced during periods when the grounded ice sheet area is large – and ice shelves fringe the ice sheet along the continental shelf break – and enhanced during periods when the grounding line is much retreated – and most of the ice shelves are located in embayments such as the Ross and Weddell seas (Figs. 4.2B, 4.3B). Periods of rapid sea level rise furthermore are associated with sharp spikes in the calving rate

(Fig. B.2). As will be discussed below, the sea level induced migration of the grounding line is a strong modulator of the ice sheet response to climatic forcing.

In our simulation, the mass balance of the AIS most strongly responds to climatic forcing through changes in the surface melt rate. Surface ablation is calculated using the widely-used positive degree day (PDD) parameterization, in which melt rates are a function of both annual mean and seasonal temperatures (Reeh, 1991). As annual mean temperatures over Antarctica decrease with decreasing greenhouse gas concentrations (Fig. 4.1B), surface melt rates are reduced and contribute to ice sheet growth (Fig. 4.3D). The number of PDDs in our model strongly increases when high CO_2 combines with long summer length during periods of low precession and high eccentricity (Fig. 4.1A). This leads to high interglacial surface melt rates, in particular around the ice sheet perimeter, with some interglacials showing ice sheet average melt rates almost double those of present-day (Fig. 4.3D). Because Southern Hemisphere summer length is in phase with Northern Hemisphere summer insolation (Huybers & Denton, 2008, Huybers, 2009), surface melt peaks and global sea level rise contribute to Antarctic deglaciation at the same time.

In contrast to the climatic forcing discussed above (Fig. 4.1D), ice sheet averaged accumulation rates *increase* during glacial times (Fig. 4.3E). The reason for this is that accumulation rates are near-zero over much of the interior of the AIS and much higher towards its edges. As the grounding line expands equator-ward due to lower glacial sea level and surface melt, more of the AIS area lies in regions with accumulation rates that are higher on average, despite the glacial drop in precipitation. This is illustrated by comparing the accumulation rates averaged over the evolving ice sheet area to those averaged over the present-day ice sheet area. In the latter case, accumulation rates decrease during glacial periods, in accordance with the climatic forcing. Different from previous studies using temperature-based precipitation parameterizations (Ritz et al., 2001, Huybrechts, 2002, Pollard & DeConto, 2009), Antarctic accumulation changes in our simulation are thus found to be a response to, rather than a driver of, Antarctic ice sheet evolution.

Similar to the changes in accumulation rates, the changes in ice sheet averaged oceanic melt rates also oppose the climatic forcing. Circum-Antarctic ocean temperatures decrease during glacial

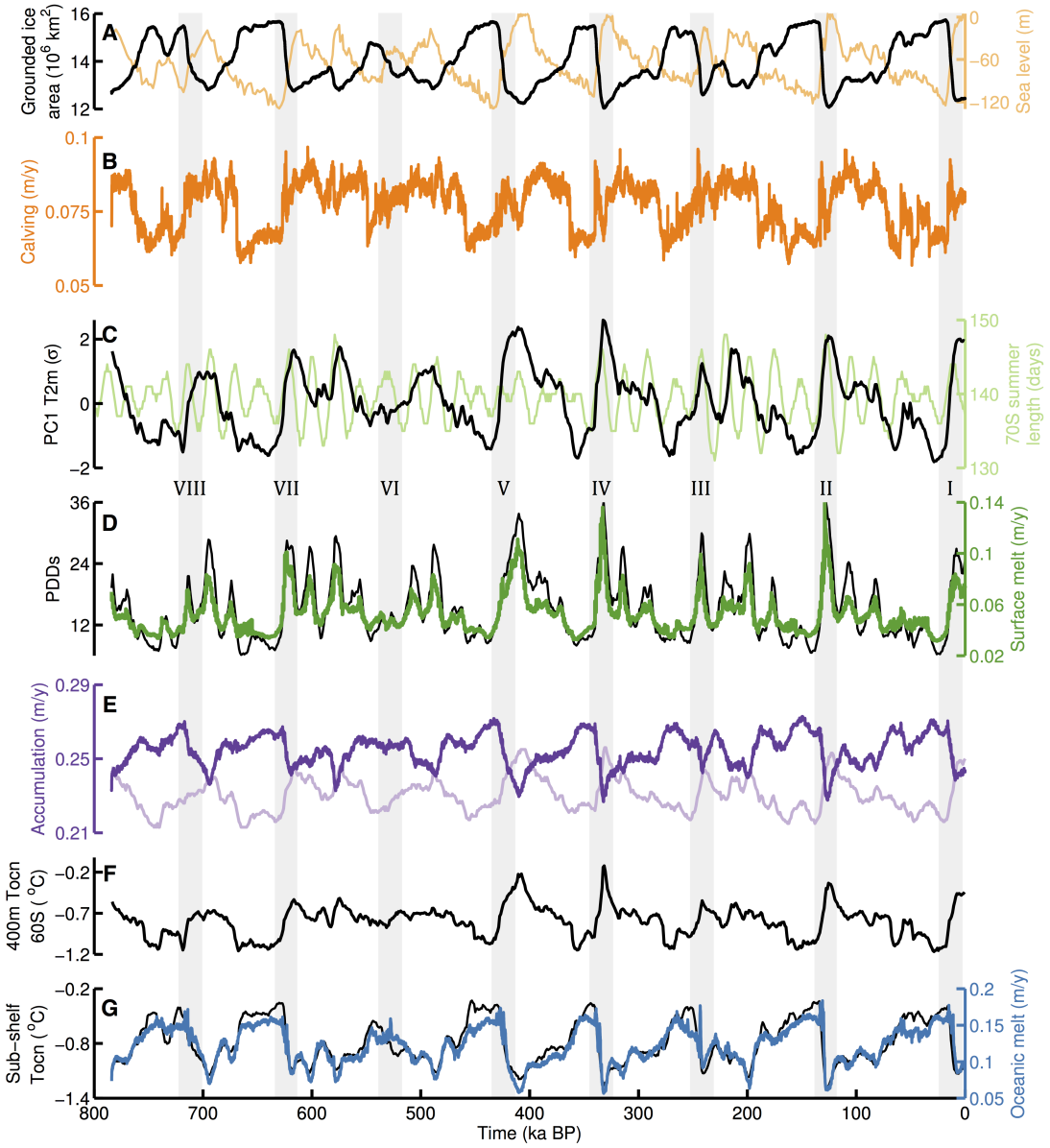

Figure 4.3: Climatic drivers of Antarctic mass balance terms – (A) grounded ice sheet area (black) and sea level forcing from δ^{18}O (light orange) (Lisiecki & Raymo, 2005); (B) 50 y mean ice sheet averaged calving rate; (C) normalized PC1 of modeled annual mean atmospheric temperatures (black) and 70 °S summer length (light green); (D) ice sheet averaged PDDs (black) and 50 y mean ice sheet averaged residual ablation (green; see Methods); (E) accumulation rate averaged over time-evolving ice sheet area (annual mean; dark purple) and present-day ice sheet area (1000-y mean; light purple); (F) zonally averaged 60 °S 400 m ocean temperatures; (G) average ocean temperatures underneath the ice shelves (black) and 50 y mean ice sheet averaged oceanic melt rate (blue). Terminations I-VIII are indicated by grey shading.

periods, with an amplitude of ∼1 °C (Figs. 4.1F-G, 4.3F). Oceanic melt rates on the other hand *increase* during glacial times (Fig. 4.3G). The equator-ward expansion of the Antarctic grounding line in response to dropping sea level causes the glacial ice shelves to reside closer to Circumpolar Deep Water. Even though the glacial ocean is colder than the interglacial ocean, the equator-ward positioned glacial ice shelves thus effectively feel warmer waters (Fig. 4.3G) (Kusahara et al., 2015). Brief peaks in oceanic melt rates occur during deglaciations (Fig. S3), when sea level rise increases the volume of floating ice. The role of warming oceans at the end of glacial periods, found to be important in previous studies (Mackintosh et al., 2011), might be underestimated in our study due to the relatively low climate sensitivity of our climate model.

4.5 Conclusions

We have presented results from an ice sheet model simulation over the last 784 ka, forced with eustatic sea level changes and climate anomalies from an intermediate complexity climate model. Over these last eight glacial cycles, the simulated Antarctic ice sheet contributes between 6–12 m to glacial sea level drop, and up to 2 m to interglacial sea level high stands. Rates of global sea level rise during terminations as a result of AIS retreat are up to 0.3 m per 100 yr. Our findings suggest that southern ice sheet variability is strongly coupled to changes in Northern Hemisphere ice sheets and climate. Eustatic sea level change as a result of northern ice sheet evolution is an important driver of Antarctic grounding line migration. The AIS response to sea level changes modulates its response to other climatic drivers – for both accumulation and oceanic melt rates the changes in ice sheet configuration dominate over the glacial-interglacial climate forcing. Changes in atmospheric CO_2 and precession-driven summer length jointly drive changes in surface melt rates, critically contributing to glacial expansion during cold periods and initiating deglaciation in phase with Northern Hemisphere summer insolation and global sea level rise.

Our ice sheet simulations include the sea level, CO_2 and orbital forcing of the Late Quaternary, but not the millennial scale variability associated with meltwater pulses in the North Atlantic.

The Southern Ocean and Antarctic warming that result from a meltwater-induced weakening of the meridional overturning circulation could further enhance concurrent melting of the Antarctic ice sheet. Similarly, our modeling setup precludes a consideration of the feedbacks between Antarctic ice sheet variability and climate, in particular the effect of Antarctic freshwater forcing on ocean circulation and resulting ice-ocean feedbacks (Menviel et al., 2010, 2011, Golledge et al., 2014). Such feedbacks have the potential to substantially accelerate AIS retreat and increase the Antarctic contribution to meltwater pulses (Menviel et al., 2010, Golledge et al., 2014). Irrespective of these millennial-scale contributions, our results highlight the joint role of sea level, CO_2 and local insolation as synchronous pace-makers of bipolar ice sheet variability.

CHAPTER 5

Synthesis

5.1 Summary of main findings

The response of earth's climate system to external forcing is highly nonlinear. Although the changes in earth's orbit responsible for variations in the seasonal and latitudinal distribution of insolation have shown stable oscillations over at least the past 50 million years (Ma) (Laskar et al., 2004), the response of earth's climate to these oscillations has varied widely over this period (Zachos et al., 2001, Lisiecki & Raymo, 2005). The expansion of Northern Hemisphere ice sheets around 3 Ma substantially increased earth's sensitivity to orbital forcing and initiated the large glacial-interglacial climate swings that mark the Quaternary (Fig. 1.1). This dissertation focused on two particular cases of nonlinear responses to orbital changes during the Late Quaternary, roughly defined as 800 thousand years ago (ka) until present:

- rectification of the zero annual mean precessional forcing into an annual mean climate response, as observed in numerous records of Quaternary climate variability
- modulation of the climate sensitivity to orbital forcing by the earth system response itself, i.e., the role of changes in e.g., atmospheric greenhouse gas concentrations, Northern Hemisphere

ice sheets and global sea level with a ~100 ka periodicity in rectifying the climate response to orbital forcing.

Chapter 2 examined this problem from a tropical perspective. Out of earth's three orbital parameters, precession is the one with the strongest expression in the tropics (Berger, 1978, Laskar et al., 2004). Much more so than at high latitudes, Quaternary climate records from the tropics contain strong precessional variability, in particular those recording hydroclimate (Fig. 2.1; e.g., Fritz et al., 2004, Wang et al., 2004b, Dykoski et al., 2005, Weldeab et al., 2007, Tjallingii et al., 2008, Deplazes et al., 2013, Tachikawa et al., 2014). Previous work investigating the origins of this precessional variability has mostly focused on the various continental monsoon systems and suggests that precipitation increases with summer insolation in response to precessional forcing (Kutzbach & Otto-Bliesner, 1982, Kutzbach & Guetter, 1986, Braconnot & Marti, 2003, Tuenter et al., 2003, Zhao et al., 2005, Wyrwoll et al., 2007, Braconnot et al., 2008, Kutzbach et al., 2008, Shi et al., 2011, Bosmans et al., 2012, Khon et al., 2012, Masson-Delmotte et al., 2013). Most of these studies however have primarily looked at the seasonal response of precipitation to changes in precession, without addressing the nonlinear mechanisms rectifying the precipitation changes in the annual mean.

In order to identify these nonlinear mechanisms, three time slice experiments were conducted with the Community Earth System Model (CESM) version 1.0.3 (Chikamoto et al., 2015): one simulation with high precession (Southern Hemisphere summer solstice in perihelion), one simulation with low precession (Northern Hemisphere summer solstice in perihelion) and one simulation where earth's orbit is circular ($e = 0$) so that precession does not matter. All simulations were conducted with pre-industrial atmospheric greenhouse gas concentrations, present-day obliquity, and the precessional runs both had an eccentricity $e = 0.067$ in order to maximize the effect of precession. The results showed that in a zonal mean sense, the paradigm of summer hemisphere with more insolation getting wetter is true. Regionally however, the annual precipitation changes are highly diverse, suggesting that regional dynamics play an important role in rectifying the annual mean precipitation response

to precessional forcing.

Over the tropical Atlantic, the response of the oceanic Intertropical Convergence Zone to precessional forcing is characterized by an annual mean shift towards the summer hemisphere with more insolation. At first glance this may seem to confirm 'the summer hemisphere with more insolation gets wetter'-framework. However, when looking at the seasonal evolution of precipitation changes over the Atlantic ocean, it was found that the seasonal precipitation response is opposite to the seasonal insolation forcing: Under maximum precession, when Northern Hemisphere summer receives less insolation and Northern Hemisphere winter receives more, boreal summer precipitation decreases north of 5 °N and strongly increases on and south of the equator, while in boreal winter precipitation decreases over the entire tropical Atlantic. The annual mean shift in the Atlantic ITCZ is due to both a change in its seasonal march and a change in the seasonal intensity of precipitation. Both of these changes can be attributed to the response of the neighboring continents, in particular the African continent, to the precessional insolation forcing.

The meridional *position* of the Atlantic ITCZ is affected by cross-equatorial gradients in sea surface temperature (SST). When insolation in boreal summer increases in response to precessional forcing ('minimum precession'), atmospheric temperatures over northern Africa increase, leading to a weakening of the north Atlantic trades. This reduces latent heat fluxes over the ocean, strengthening the meridional SST gradient and – through the Wind-Evaporation-SST (WES) feedback – pushing the ITCZ north. On the other hand, when insolation in boreal winter increases in response to precessional forcing ('maximum precession'), the location of maximum temperature increase does not coincide with maximum insolation forcing, surface wind changes over the Atlantic are small and the WES feedback does not operate. The seasonal *intensity* of the Atlantic ITCZ is modulated by the diabatic forcing associated with the African and South-American monsoon systems. Under maximum precession, the African summer monsoon weakens, causing a cooling of the upper troposphere that destabilizes the atmosphere and increases convective precipitation over the ocean. In boreal winter, precipitation increases over South America and southern Africa, leading to a decrease in precipitation over the Atlantic. However, the boreal winter response of the continental monsoon systems is weaker than

that in boreal summer, rectifying the annual mean effect of the diabatic forcing. These processes were schematically summarized in Fig. 2.6.

Oceanic precipitation in the tropics is the result of strong coupling between oceanic and atmospheric processes. Its response to seemingly simple seasonal insolation forcing is thus not straightforward. The annual mean precipitation response to precessional forcing over the Atlantic ocean is rectified by the mean climatology of rainfall, temperature and surface boundary conditions over the African and South American continents and the Atlantic, as well as by the geometry of the African continent, which plays an important role in driving the meridional march of the Atlantic ITCZ and determining the sensitivity of Atlantic surface winds to continental temperature changes. While the precessional forcing has only meridional gradients, the climatic response has strong zonal components. An important implication of this work is therefore that traditional zonal mean frameworks of assessing the ITCZ response to external forcing (e.g., Schneider, 1977, Lindzen & Hou, 1988, Kang et al., 2009, Schneider et al., 2014) do not apply here. Recent research on the topic of ITCZ position has argued that extratropical heating leads to a zonally uniform shift of the ITCZ towards the warming hemisphere (Broccoli et al., 2006, Kang et al., 2008, 2009, Chiang & Friedman, 2012, Donohoe et al., 2013, Schneider et al., 2014). A similar approach cannot be taken when the source of heating lies within the tropics (Kang et al., 2014). During the Quaternary, the response of tropical precipitation to orbital forcing thus strongly depends on the ratio of tropical to extratropical forcing (Clement et al., 2004), with the former dominating during periods of low ice volume and/or high eccentricity, and the latter dominating during glacial maxima and millennial-scale events.

Chapters 3 & 4 investigated the nonlinearities of the Quaternary response to orbital forcing at high latitudes, by looking at the drivers of Antarctic ice sheet (AIS) evolution over the last 800 ka. The AIS has varied substantially during the Late Quaternary, contributing more than 10 m to global sea level lowering during glacial periods (Denton & Hughes, 2002, Bentley et al., 2014), and an estimated 3–6 m to past interglacial sea level highstands (Dutton et al., 2015). The evolution of northern and southern polar ice sheets appears to be synchronous on orbital timescales, which is somewhat unexpected

given the fact that precession – essential for Northern Hemisphere glacial terminations through its impact on boreal summer insolation – is anti-phased between the two hemispheres. This has caused some to conclude that Northern Hemisphere glaciations remotely drive AIS evolution through changes in the meridional overturning circulation, global sea level and atmospheric greenhouse gases (Huybers, 2009, Denton et al., 2010, He et al., 2013), while others have proposed that the Antarctic environment is sensitive to a different phase of precessional forcing (spring insolation (Timmermann et al., 2009), summer length (Huybers & Denton, 2008, Huybers, 2009)), so that bipolar ice sheet evolution is synchronous, even when the mass balance at both poles is locally forced.

To identify whether regional orbital forcing or 100 ka Northern Hemisphere variability is more important for the evolution of the AIS, a methodology was developed to force the Penn State University ice sheet model (Pollard & DeConto, 2012b) with spatially and temporally evolving climate anomalies from a 784 ka long simulation with the Earth System Model of Intermediate Complexity (EMIC) LOVECLIM (Goosse et al., 2010, Timmermann et al., 2014). Late Quaternary climate variability in the southern high latitudes was found to be dominated by the evolution of atmospheric CO_2 for atmospheric temperatures, ocean temperatures and precipitation (through its dependence on atmospheric moisture content) alike, but with important differences between the different climatic variables. Southern Ocean temperature variability also contains a substantial precessional component through the effect of spring insolation on annual mean sea ice area (Timmermann et al., 2009). Temperatures over Antarctica are affected by obliquity both directly through its effect on high latitude insolation and indirectly through its modulation of the strength of the Southern Hemisphere westerlies (Timmermann et al., 2014). In addition to this modeled climate evolution, the ice sheet model was driven with changes in global sea level (Lisiecki & Raymo, 2005), which impact the position of the grounding line (Schoof, 2007, Pollard & DeConto, 2009). A series of sensitivity experiments over the last four glacial cycles was conducted to assess the relative contribution of individual drivers to overall AIS evolution.

In the full 784 ka ice sheet model simulation, the glacial-interglacial amplitude of Antarctic ice volume changes was found to be 10–12 m sea level equivalent (SLE). During glacial times, the

Antarctic grounding line extends to the continental shelf break almost everywhere, in accordance with reconstructions (Bentley et al., 2014). The contribution to past interglacial sea level highstands in this simulation was limited at 1–2 m SLE. None of the individual drivers – sea level, atmospheric forcing, ocean temperature changes – can singlehandedly explain the full ice sheet response. The combined response to individual drivers is larger than the sum of the individual components, indicating that the AIS response to forcing is highly nonlinear. Sea level changes pace the overall evolution of the AIS by converting floating ice to grounded ice when sea level drops, and vice versa (Schoof, 2007). Lowering sea level during Northern Hemisphere glaciation thus leads to equator-ward expansion of the Antarctic grounding line, but in the absence of climatic changes this expansion is limited by surface melting at the ice sheet edge. Glacial reductions in surface melt rates are thus important in allowing the ice sheet to attain its full glacial state, while large surface melt peaks critically contribute to the onset of Antarctic deglaciations. Surface melt rates depend on both annual mean and seasonal temperatures and as such increase when atmospheric CO_2 is high and when summers are long (i.e., low precession). The latter is modulated by the former, so that surface melt rates are uniformly low during periods of low CO_2, regardless of precessional phase. Accumulation and oceanic melt changes in the full simulation are a feedback due to the evolution of the AIS rather than a direct response to climatic forcing. Because accumulation rates and oceanic temperatures are higher at lower latitudes, the AIS receives more precipitation (a positive feedback) and experiences more melting at the ice-ocean interface (a negative feedback) as its grounding line expands equator-ward.

The answer to the question whether bipolar synchronization derives from remote (Northern Hemisphere) or local (orbital) forcing is thus: both. The evolution of the Antarctic ice sheet is in phase with the evolution of Northern Hemisphere ice sheets because the large marine margins of Antarctica are sensitive to changes in global sea level, because surface melt rates changes with atmospheric CO_2 and because surface melt rates vary with Southern Hemisphere summer length, in phase with Northern Hemisphere summer insolation. This explains why in the deep sea record, benthic $\delta^{18}O$ varies in phase across the world's oceans on precessional timescales (Lisiecki & Raymo, 2005, 2007). The dependency of surface melt rates on summer length furthermore rectifies the zero annual mean

precessional forcing into an annual mean mass balance response.

An additional sensitivity run was conducted in which a number of recently proposed parameterizations of ice sheet instability were included in the ice sheet model (Pollard et al., 2015). These parameterizations represent the pre-conditioning of ice shelves for calving due to high surface melt rates, thought to be important for the 2002 collapse of the Larsen B ice shelf (van den Broeke, 2005). With these mechanisms included, a reduction in Antarctic ice volume of 3–6 m during warm Late Quaternary interglacials (such as MIS 5e, 9 and 11) becomes very plausible. While throughout Part II of this dissertation the Antarctic ice sheet was modeled in an uncoupled setting, it is clear that the changes in ice sheet configuration and large meltwater pulses provide potentially important feedbacks on circulation in the Southern Ocean and deep water production.

5.2 Discussion and Outlook

The tropical Atlantic and Antarctic systems studied in this dissertation differ substantially in terms of both the dominant (orbital) forcing during the Late Quaternary and the climate dynamical response to this forcing. Yet still some interesting parallels can be drawn between these low and high latitude regions. Firstly, in both studies, continental geometry serves as an important modulator of the climate response to external forcing (see also e.g., Short et al., 1991). In the case of the tropical Atlantic, the 'bulge' of the African continent has been implicated as one of the reasons why the annual mean ITCZ resides north of the equator in present-day climate (Xie & Saito, 2001), and is also responsible for the fact that the north Atlantic trade winds are more sensitive to pressure changes over the African continent than the south Atlantic trades are (Chiang et al., 2001). The rectified response of the annual mean Atlantic ITCZ to seasonal forcing is thus in large part due to this particular property of the present-day continental geometry. In the case of Antarctica, the maximum extent of the (grounded) Antarctic ice sheet is determined by the shape of the Antarctic continent. Unlike in the Northern Hemisphere, where ice sheets could theoretically progress southward 'indefinitely' across the North American and Eurasian continents as long as temperatures and insolation would allow them to,

the growth of the southern polar ice sheet is limited by the presence of the circumpolar Southern Ocean. Presumably, when the AIS reaches its full extent but its mass balance is still increasingly positive, the dynamics of the ice sheet are altered. Further, the bathymetry below the ice sheet is a critical component of whether or not marine ice sheet instability can accelerate ice sheet retreat (Schoof, 2007). As such, the timing and patterns of the retreat history of the AIS are modulated by its underlying bathymetry.

Secondly, both parts of this dissertation have highlighted the potential for the seasonal forcing of the precessional cycle to generate annual mean climatic change, be it low latitude hydroclimate or ice sheet surface mass balance at high latitudes. This raises an interesting point with regards to the way paleoclimatic studies are used by the climate science community. The continuously rising atmospheric CO_2 concentrations of the twentieth and twenty-first century have generated interest in calculating the 'earth system sensitivity', or: how much does the climate warm for a given radiative forcing (Solomon et al., 2007). Earth system sensitivity can be estimated from the transient, and well-recorded, climate evolution over the past century, or from model projections of future climate change in response to e.g., a doubling of CO_2. Alternatively, modeling studies and reconstructions of paleoclimates have been used to estimate the global mean temperature response to external forcing in the past (Köhler et al., 2010, Hargreaves et al., 2012, Rohling et al., 2012). This is problematic for several reasons: Besides the obvious fact that earth system sensitivity is time-varying (meaning that glacial climates respond differently to external forcing than for instance the largely ice-free climate of the mid-Pliocene, see Fig. 1.1), defining radiative forcing – and distinguishing between so-called 'slow' and 'fast' feedbacks – throughout the Quaternary is not straightforward. This is particularly apparent in the case of precession, which in the purest definition of earth system sensitivity would comprise a radiative forcing of zero. Yet looking at the two runs that were conducted with CESM in Part I of this dissertation, the zero-annual mean precessional forcing in these simulations leads to an annual mean change in global mean temperature of 0.4 °C (P_{MAX}–P_{MIN}). Theoretically, this would imply an earth system sensitivity that is infinite! Thus, when calculating earth system sensitivity from transient paleoclimate simulations or reconstructions of past climates, it should be kept in mind

that earth system responses (to seasonal forcing) are included in the temperature response that are presently not equally represented in the radiative forcing.

As discussed in the Introduction and Sect. 2.4.3, long cycles with a periodicity of ~400 ka have been found in records of benthic $\delta^{13}C$ and carbonate preservation from the Cretaceous (145–66 Ma) through the Cenozoic (e.g. Tiedemann et al., 1994, Herbert, 1997, Tian et al., 2002, Wang et al., 2010). Interestingly, similar variability has not been found for $\delta^{18}O$, or at the 100 ka eccentricity period. These records seem to suggest that the amplitude modulation of precession by eccentricity results in a rectification of the global carbon cycle. In two recent modeling studies Russon et al. (2010) and Ma et al. (2011) used box models to test the effect of certain forcing functions (such as changes in total productivity, ratio of carbonate to organic carbon, and continental weathering) on variables for which records exist from the Pleistocene and Miocene respectively. Although both studies were able to match amplitude and phase relationships of model output to climate records, both studies used forcing functions with a built-in 400 ka period, thus bypassing the question of why these forcing functions would be responding to eccentricity at all. Time slice experiments with coupled earth system models, such as the simulations conducted for Part I of this dissertation, could be used to identify these nonlinear rectification mechanisms.

A measure of the eccentricity rectification is the degree to which the maximum (P_{MAX}) and minimum (P_{MIN}) precession deviates from the zero eccentricity state (E_{ZERO}) ($0.5 \times \left(x_{P_{MAX}} + x_{P_{MIN}}\right) - x_{E_{ZERO}}$; Eq. 2.10). Figure 5.1 shows the rectified response of net primary productivity and deep ocean $\delta^{13}C$ in the CESM simulations. (Phosphate was used as a proxy for $\delta^{13}C$ in the absence of a carbon isotope module in the model: $\delta^{13}C = -1.1 \times PO_4 + 2.9$ (Broecker & Maier-Reimer, 1992).) While the mechanisms responsible for this rectification still need to be further explored, this figure indicates that even in the absence of some of the proposed forcing functions (such as weathering changes), coupled earth system models can generate substantial eccentricity rectification in the carbon cycle[1].

[1]Note that these simulations were only 500 y long, so the carbon cycle was not fully equilibrated for the calculations for Fig. 5.1.

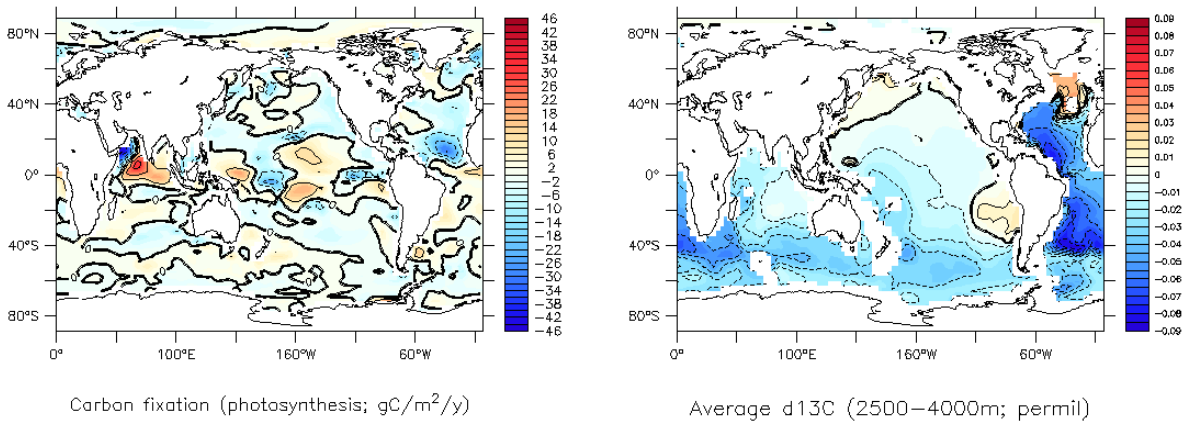

Figure 5.1: Eccentricity rectification of global carbon cycle – (left) carbon fixation from photosynthesis in surface ocean (gC m^{-2} y^{-1}); (right) deep-sea (2500–4000 m) $\delta^{13}C$ (permil; where $\delta^{13}C$ = -1.1 × PO_4 + 2.9 (Broecker & Maier-Reimer, 1992)).

Finally, a few things can be said about the future of modeling past climates. Until now, paleoclimate modeling efforts have been limited mostly by computing power. Rather than conduct long transient simulations of e.g., the entire Late Quaternary, most modeling studies therefore either model specific time slices (as done for the CESM simulations in Part I), or use accelerated boundary conditions (as done for the LOVECLIM simulations in Part II). The Climate Model Intercomparison Project (CMIP) has incorporated a number of paleoclimate time slices in their list of requested simulations, to facilitate the comparison of the performance of different climate models in 'out-of-sample' climates, and to construct ensemble simulations to compare paleorecords against. In some cases, these paleo-CMIP experiments have even been used to help constrain projections of future climate change (Schmidt et al., 2014). However, the work presented in this dissertation has shown that the climate system responds strongly to precession, and that different parts of the climate system are sensitive to different phases of precession. Yet the time slices chosen for the CMIP experiments (Last Glacial Maximum and mid-Holocene (6 ka)) only sample a limited range of precessional phases. It might therefore be worth considering adding an additional experiment to the CMIP list, for instance minimum precession during MIS 5e (130 ka). Moreover, care should be taken when using, e.g., the mid-Holocene simulation for projections of future climate, because the climate dynamical response

to orbital forcing is very distinct from that to greenhouse gas forcing (e.g., Clement et al., 2004, Ganopolski & Robinson, 2011, Erb et al., 2013).

The discussion in Part II of this dissertation has also highlighted the large degree to which climate and ice sheets feed back on each other during the glacial cycles of the Quaternary. To fully understand the massive transition between cold glacial climates and warm interglacial climates, one cannot study either the climate system or the ice sheet systems in isolation from each other. Although several research groups around the world have been working on developing high-resolution, full-physics, coupled models of ocean, atmosphere and ice sheet for the Antarctic region, these models will mostly be useful for modeling changes in the Southern Hemisphere environment in the near future (up to a century), given the extremely high demands on computing power that these systems impose. Furthermore, because of their regional scale, they will not be able to help answer some of the remaining open questions about Quaternary glacial cycles, such as the role of Antarctic freshwater fluxes in altering the global ocean circulation and mechanisms of bipolar coupling. Therefore it will be worthwhile for the paleoclimate and glaciological modeling communities to continue to invest in models of intermediate complexity (EMICs for climate and shallow ice/shallow shelf for ice sheets) that are inexpensive to run and that could be run in coupled mode over tens of thousands of years. Thus far this has been achieved for the Northern Hemisphere ice sheets (Ganopolski et al., 2010, Heinemann et al., 2014), but not for the Antarctic ice sheet or both ice sheets together. If then finally also a carbon cycle module is included, one could attempt true earth system modeling, where the only external forcing is the orbital forcing.

APPENDIX A

Atlantic moisture budget analysis

Changes in precipitation can be the result of changes in thermodynamics (a change in specific humidity as a result of temperature changes), by changes in mean circulation (the advection and convergence of moisture), by changes in the transient eddy moisture convergence, or by changes in evaporation. One can quantify these different contributions by determining the individual components that comprise the moisture budget. A similar approach was taken e.g. by Clement et al. (2004) and Merlis et al. (2013) for the precessional cycle, and by e.g. Held & Soden (2006) and Seager et al. (2010) for present-day climate change. Here we follow the formalism of Seager et al. (2010); a complete derivation can be found in Trenberth & Guillemot (1995).

The full moisture budget equation is:

$$\rho_w g(P-E) = -\int_0^{p_s} \nabla\cdot(\overline{\mathbf{u}}\,\overline{q})\,dp - \int_0^{p_s} \nabla\cdot\left(\overline{\mathbf{u}'q'}\right)dp - q_s\mathbf{u_s}\cdot\nabla p_s \tag{A.1}$$

where overbars indicate monthly means, primes indicate deviations from the monthly mean, ρ_w is the density of water, $P-E$ is precipitation minus evaporation, p is pressure, $\mathbf{u}$ are the horizontal wind velocities, q is specific humidity, and subscripts s indicate surface values. The first term on the

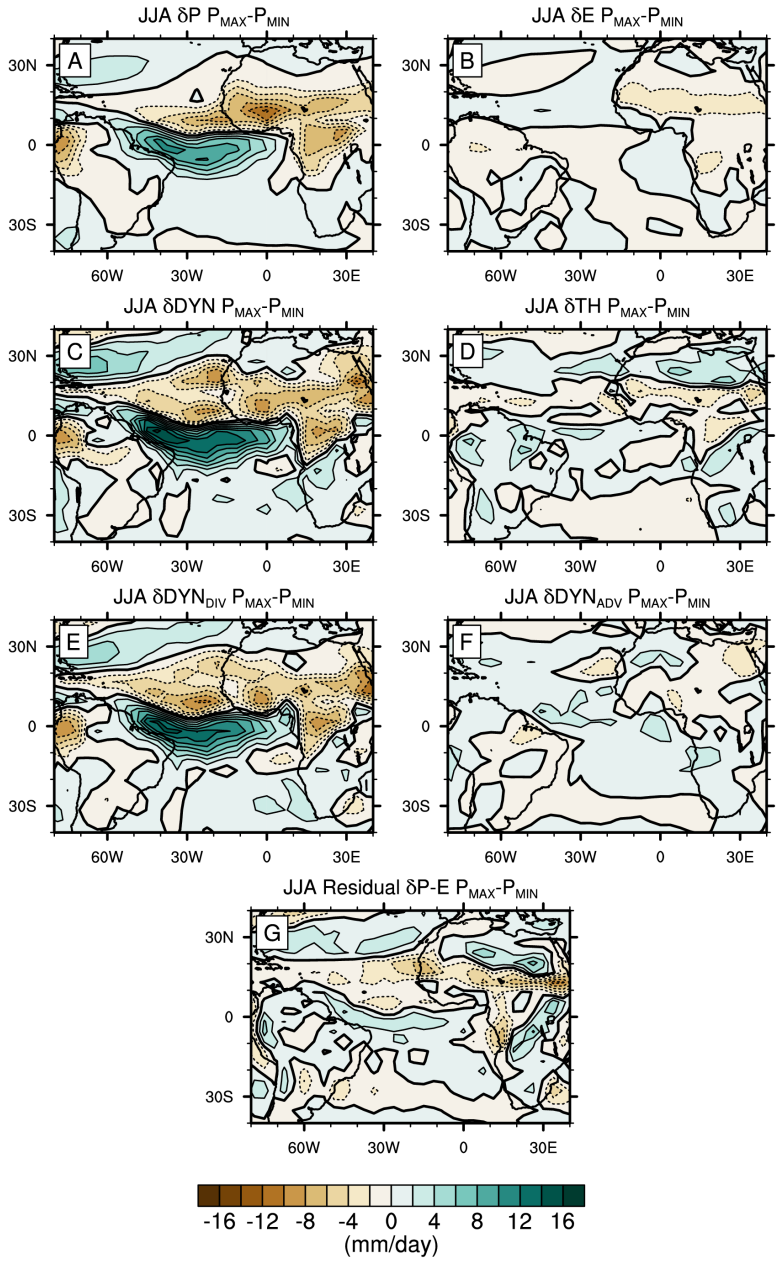

Figure A.1: JJA P_{MAX}–P_{MIN} change in precipitation (a); contributions to this change from changes in (b) evaporation; (c) winds (δDYN in Eq. (A.2)), (d) specific humidity (δTH in Eq. (A.2)), (e) divergence (δDYN_{DIV} in Eq. (A.3)) and (f) advection (δDYN_{ADV} in Eq. (A.3)); and (g) the difference between diagnosed and modeled changes in net precipitation

right-hand side describes moisture convergence by the mean flow, while the second term represents that due to transient eddies. The last term on the right-hand side is a surface term which is generally found to be small.

The P_{MAX}–P_{MIN} difference in the moisture budget becomes:

$$\begin{aligned}\delta(P-E) = &-\frac{1}{\rho_w g}\left\{\int_0^{p_s} \nabla\cdot\left(\delta\overline{\mathbf{u}}\ \overline{q}_{P_{MIN}}\right)dp\right.\\ &+\int_0^{p_s} \nabla\cdot\left(\overline{\mathbf{u}}_{P_{MIN}}\ \delta\overline{q}\right)dp\\ &+\int_0^{p_s} \nabla\cdot\delta\left(\overline{\mathbf{u}'q'}\right)dp\\ &+\int_0^{p_s} \nabla\cdot\left(\delta\overline{\mathbf{u}}\ \delta\overline{q}\right)dp\\ &\left.+\ \delta\left(q_s\mathbf{u_s}\cdot\nabla p_s\right)\right\}\\ \delta P = &\ \delta DYN+\delta TH+\delta TE+\delta NL-\delta S+\delta E\end{aligned} \tag{A.2}$$

where δ is the difference operator. The first term on the right-hand side represents changes in the moisture budget due to changes in the monthly mean circulation; we will refer to this term as the 'dynamic' contribution, δDYN. The second term is the contribution due to changes in the monthly mean specific humidity, which will be referred to as the 'thermodynamic' term δTH. The third, fourth, and fifth term represent the transient eddy contribution δTE, the nonlinear product of circulation and humidity changes δNL, and changes in the surface term δS, respectively. These are either found to be small (δNL and δS) or cannot be estimated from our model output (δTE).

We can further split the dynamical term δDYN into a part relating to the anomalous convergence of the mean specific humidity field, and a part relating to the anomalous advection of the mean specific humidity gradient:

$$\begin{aligned}\delta DYN &= -\int_0^{p_s}\left(\overline{q}_{P_{MIN}}\nabla\cdot\delta\overline{\mathbf{u}}\right)dp-\int_0^{p_s}\left(\delta\overline{\mathbf{u}}\cdot\nabla\overline{q}_{P_{MIN}}\right)dp\\ &= \delta DYN_{DIV}+\delta DYN_{ADV}\end{aligned} \tag{A.3}$$

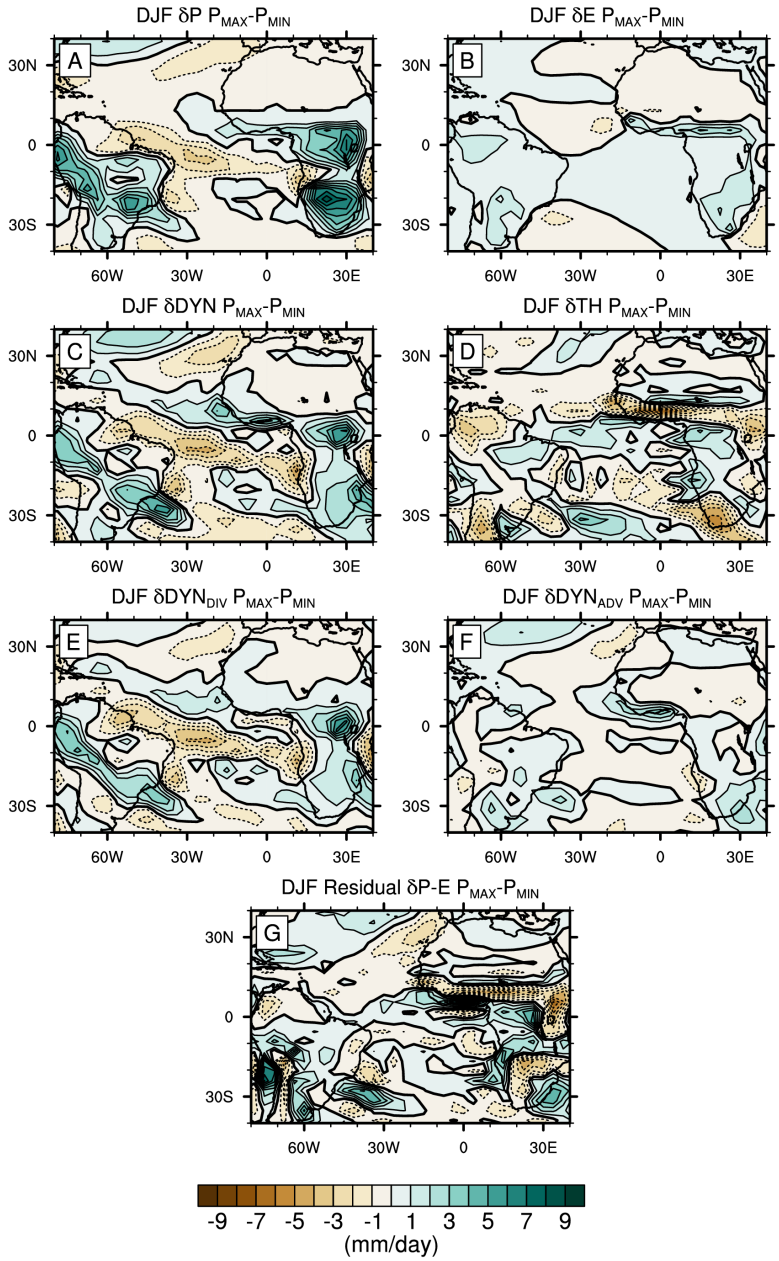

Figure A.2: DJF P_{MAX}–P_{MIN} change in precipitation (a); contributions to this change from changes in (b) evaporation; (c) winds (δDYN in Eq. (A.2)), (d) specific humidity (δTH in Eq. (A.2)), (e) divergence (δDYN_{DIV} in Eq. (A.3)) and (f) advection (δDYN_{ADV} in Eq. (A.3)); and (g) the difference between diagnosed and modeled changes in net precipitation

These various components are shown for JJA in Fig. A.1 and for DJF in Fig. A.2. First of all, it should be noted that the DJF precipitation response is smaller than the JJA response, especially over the ocean, and is not a mirror image of the JJA response. In both seasons, over the Atlantic Ocean as well as over the continents, the dynamic component (Figs. A.1c and A.2c) strongly dominates the response. Evaporation changes (Figs. A.1b and A.2b) are small, and generally of the same sign as the dynamical term. In JJA, the thermodynamic term (Fig. A.1d) too is small, and generally of the same sign as the dynamic term, except over the most northern part of Africa, the North Atlantic, and equatorial South America. In DJF on the other hand, the thermodynamic component (Fig. A.2d) is mostly opposite in sign to the dynamic changes. In JJA as well as DJF, the dynamic component is made up almost entirely of the $\delta \mathrm{DYN}_{\mathrm{DIV}}$ term (compare Fig. A.1e with A.1f and Fig. A.2e with A.2f). Differences between the diagnosed and modeled changes in net precipitation (Figs. A.1g and A.2g) stem from our ignoring of the transient eddy term, as well as calculation errors due to interpolation and discretization (Seager et al., 2010).

APPENDIX B

Antarctic mass balance during terminations

The figures on the following pages zoom in on Terminations I, II, III, IV, V and VII to better illustrate the mass balance changes driving Antarctic deglaciation.

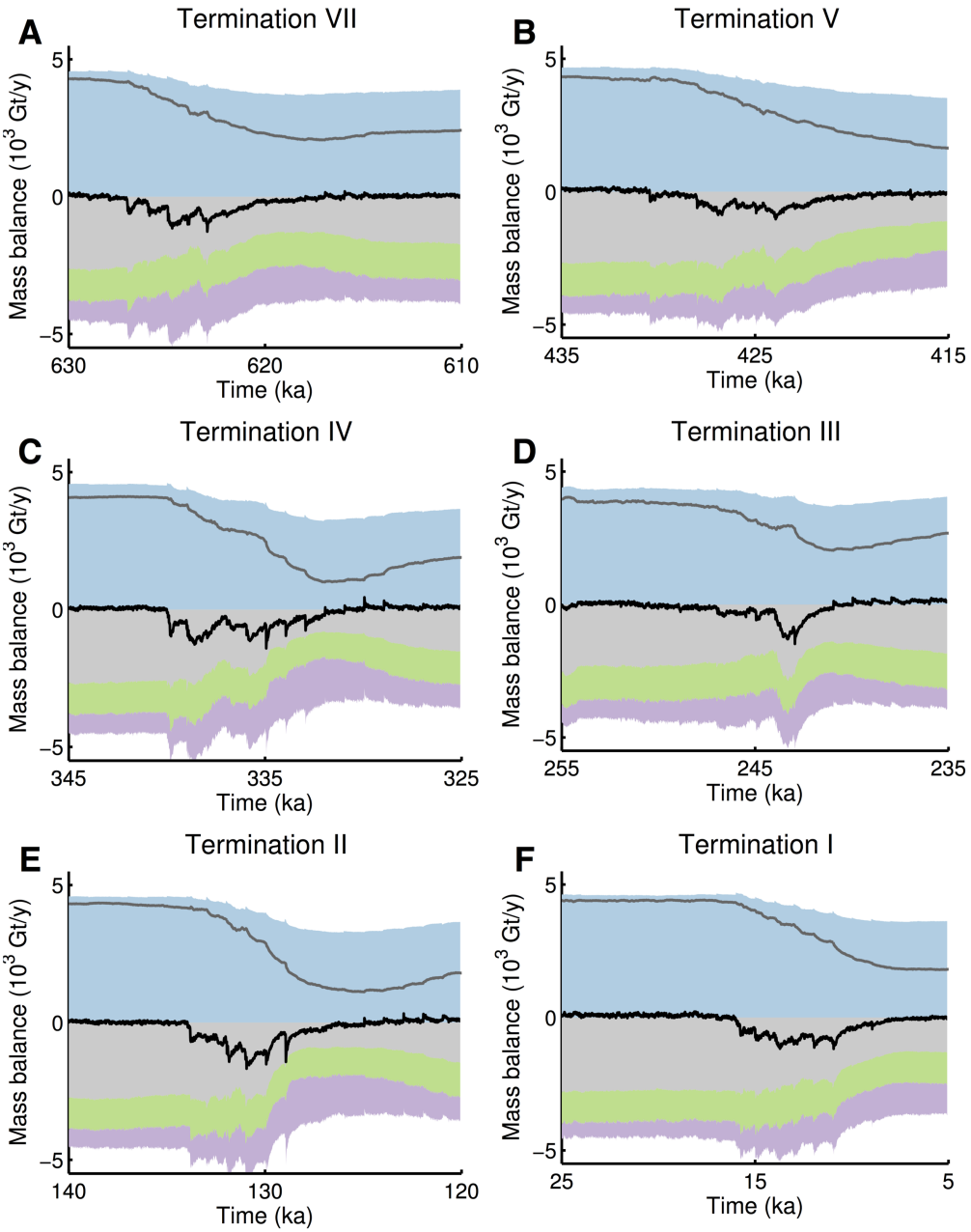

Figure B.1: Ice sheet integrated mass balance terms (shading; accumulation in blue, oceanic melt in grey, calving in green, residual ablation (see Methods) in purple) and net mass balance (black) in 10^3 Gt y^{-1} (10^3 Gt y^{-1} ~0.03 Sv) and ice sheet area (grey line) during (A) Termination VII, (B) Termination V, (C) Termination IV, (D) Termination III, (E) Termination II and (F) Termination I. Mass balance terms are plotted as 10-year averages.

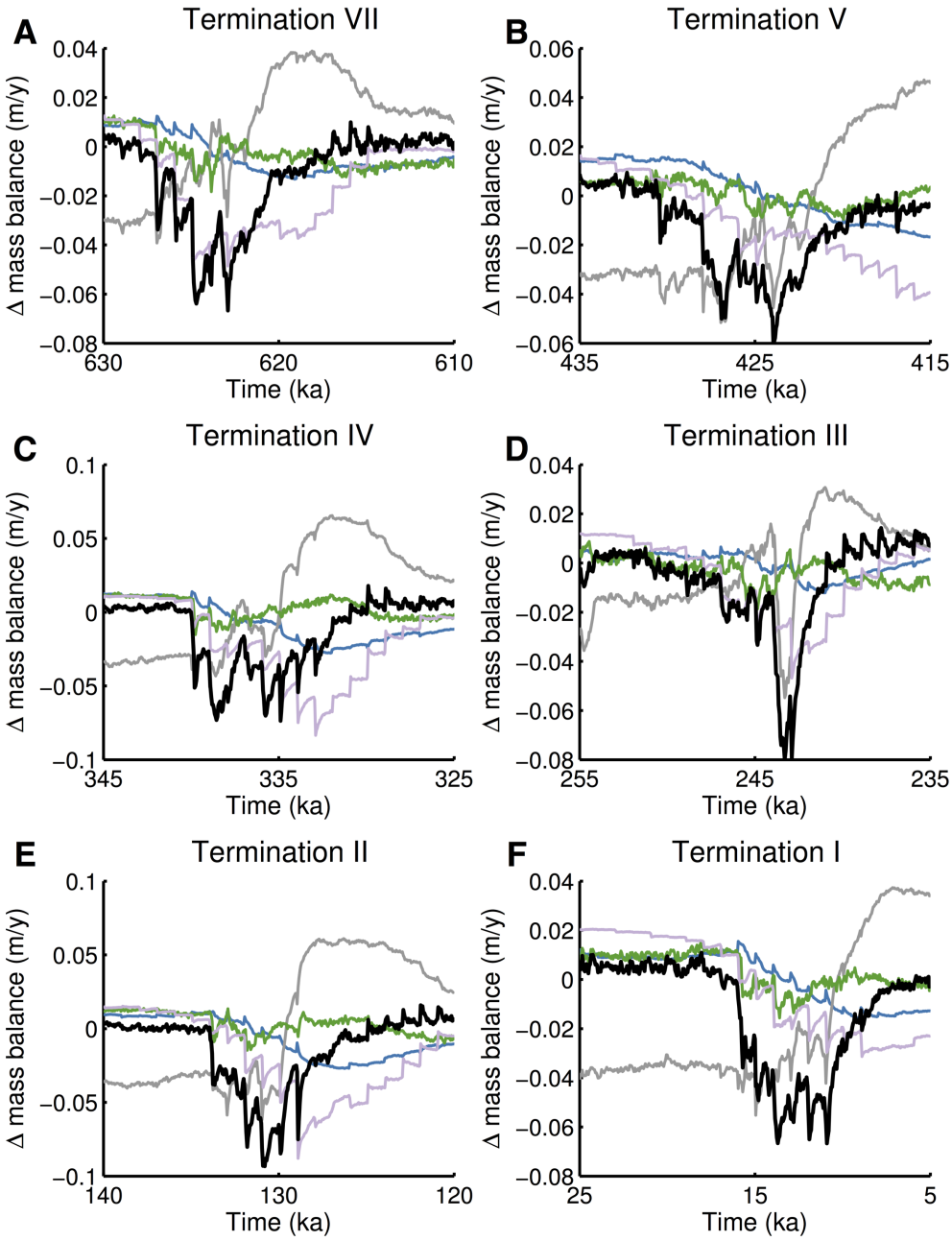

Figure B.2: Anomalies of ice sheet averaged mass balance terms with respect to the long-term mean (accumulation in blue, oceanic melt in grey, calving in green, residual ablation (see Methods) in purple) and net mass balance (black) in m y^{-1}(A) Termination VII, (B) Termination V, (C) Termination IV, (D) Termination III, (E) Termination II and (F) Termination I. Mass balance terms are plotted as 50-year averages.

Bibliography

Abe-Ouchi, A., Saito, F., Kawamura, K., Raymo, M. E., Okuno, J., Takahashi, K., & Blatter, H. (2013). Insolation-driven 100,000-year glacial cycles and hysteresis of ice-sheet volume. *Nature*, 500(7461), 190–193.

Abe-Ouchi, A., Segawa, T., & Saito, F. (2007). Climatic conditions for modelling the Northern Hemisphere ice sheets throughout the ice age cycle. *Climate of the Past*, 3, 423–438.

Alley, R. B., Clark, P. U., Huybrechts, P., & Joughin, I. (2005). Ice-sheet and sea-level changes. *Science*, 310, 456–461.

Annan, J. D. & Hargreaves, J. C. (2013). A new global reconstruction of temperature changes at the Last Glacial Maximum. *Climate of the Past*, 9(1), 367–376.

Arbuszewski, J. A., DeMenocal, P. B., Cléroux, C., Bradtmiller, L., & Mix, A. (2013). Meridional shifts of the Atlantic Intertropical Convergence Zone since the Last Glacial Maximum. *Nature Geoscience*, 6(11), 959–962.

Bar-Or, R., Erlick, C., & Gildor, H. (2008). The role of dust in glacial-interglacial cycles. *Quaternary Science Reviews*, 27(3-4), 201–208.

Bartoli, G., Sarnthein, M., Weinelt, M., Erlenkeuser, H., Garbe-Schönberg, D., & Lea, D. (2005). Final closure of Panama and the onset of northern hemisphere glaciation. *Earth and Planetary Science Letters*, 237(1-2), 33–44.

Bassis, J. N. & Walker, C. C. (2012). Upper and lower limits on the stability of calving glaciers from the yield strength envelope of ice. *Proceedings of the Royal Society A*, 468(2140), 913–931.

Bazin, L., Landais, a., Lemieux-Dudon, B., Toyé Mahamadou Kele, H., Veres, D., Parrenin, F., Martinerie, P., Ritz, C., Capron, E., Lipenkov, V., Loutre, M. F., Raynaud, D., Vinther, B., Svensson, a., Rasmussen, S. O., Severi, M., Blunier, T., Leuenberger, M., Fischer, H., Masson-Delmotte, V., Chappellaz, J., & Wolff, E. (2013). An optimized multi-proxy, multi-site Antarctic ice and gas orbital chronology (AICC2012): 120-800 ka. *Climate of the Past*, 9(4), 1715–1731.

Beaufort, L., van der Kaars, S., Bassinot, F. C., & Moron, V. (2010). Past dynamics of the Australian monsoon: precession, phase and links to the global monsoon concept. *Climate of the Past*, 6(5), 695–706.

Beckmann, A. & Goosse, H. (2003). A parameterization of ice shelf-ocean interaction for climate models. *Ocean Modelling*, 5, 157–170.

Bentley, M. J., Ó Cofaigh, C., Anderson, J. B., Conway, H., Davies, B., Graham, A. G., Hillenbrand, C.-D., Hodgson, D. a., Jamieson, S. S., Larter, R. D., Mackintosh, A., Smith, J. a., Verleyen, E., Ackert, R. P., Bart, P. J., Berg, S., Brunstein, D., Canals, M., Colhoun, E. a., Crosta, X., Dickens, W. a., Domack, E., Dowdeswell, J. a.,

Dunbar, R., Ehrmann, W., Evans, J., Favier, V., Fink, D., Fogwill, C. J., Glasser, N. F., Gohl, K., Golledge, N. R., Goodwin, I., Gore, D. B., Greenwood, S. L., Hall, B. L., Hall, K., Hedding, D. W., Hein, A. S., Hocking, E. P., Jakobsson, M., Johnson, J. S., Jomelli, V., Jones, R. S., Klages, J. P., Kristoffersen, Y., Kuhn, G., Leventer, A., Licht, K., Lilly, K., Lindow, J., Livingstone, S. J., Massé, G., McGlone, M. S., McKay, R. M., Melles, M., Miura, H., Mulvaney, R., Nel, W., Nitsche, F. O., O'Brien, P. E., Post, A. L., Roberts, S. J., Saunders, K. M., Selkirk, P. M., Simms, A. R., Spiegel, C., Stolldorf, T. D., Sugden, D. E., van der Putten, N., van Ommen, T., Verfaillie, D., Vyverman, W., Wagner, B., White, D. a., Witus, A. E., & Zwartz, D. (2014). A community-based geological reconstruction of Antarctic Ice Sheet deglaciation since the Last Glacial Maximum. *Quaternary Science Reviews*, (pp. 1–9).

Berger, A. L. (1978). Long-term variations of daily insolation and Quaternary climatic changes. *Journal of the Atmospheric Sciences*, 35, 2362–2367.

Biasutti, M., Battisti, D. S., & Sarachik, E. S. (2004). Mechanisms controlling the annual cycle of precipitation in the tropical Atlantic sector in an atmospheric GCM. *Journal of Climate*, 17, 4708–4723.

Biasutti, M., Battisti, D. S., & Sarachik, E. S. (2005). Terrestrial influence on the annual cycle of the Atlantic ITCZ in an AGCM coupled to a slab ocean model. *Journal of Climate*, 18(1), 211–228.

Bickert, T., Berger, W. H., Burke, S., Schmidt, H., & Wefer, G. (1993). Late Quaternary stable isotope record of benthic foraminifers: Sites 805 and 806, Ontong Java Plateau. In W. H. Berger, L. W. Kroenke, T. R. Janecek, & W. V. Sliter (Eds.), *Proceedings of the Ocean Drilling Program, Scientific Results*, volume 130 (pp. 411–420). College Station, TX: Ocean Drilling Program.

Blunier, T. & Brook, E. J. (2001). Timing of millennial-scale climate change in Antarctica and Greenland during the last glacial period. *Science*, 291(5501), 109–12.

Bosmans, J. H. C., Drijfhout, S., Tuenter, E., Lourens, L. J., Hilgen, F. J., & Weber, S. L. (2012). Monsoonal response to mid-Holocene orbital forcing in a high resolution GCM. *Climate of the Past*, 8(2), 723–740.

Bozzano, G., Kuhlmann, H., & Alonso, B. (2002). Storminess control over African dust input to the Moroccan Atlantic margin (NW Africa) at the time of maxima boreal summer insolation: a record of the last 220 kyr. *Palaeogeography, Palaeoclimatology, Palaeoecology*, 183(1-2), 155–168.

Braconnot, P. & Marti, O. (2003). Impact of precession on monsoon characteristics from coupled ocean atmosphere experiments: changes in Indian monsoon and Indian ocean climatology. *Marine Geology*, 201(1-3), 23–34.

Braconnot, P., Marti, O., Joussaume, S., & Leclainche, Y. (2000). Ocean feedback in response to 6 kyr BP insolation. *Journal of Climate*, 13, 1537–1553.

Braconnot, P., Marzin, C., Grégoire, L., Mosquet, E., & Marti, O. (2008). Monsoon response to changes in Earth's orbital parameters: comparisons between simulations of the Eemian and of the Holocene. *Climate of the Past*, 4(4), 281–294.

Broccoli, A. J., Dahl, K. A., & Stouffer, R. J. (2006). Response of the ITCZ to Northern Hemisphere cooling. *Geophysical Research Letters*, 33, 1–4.

Broecker, W. S. & Maier-Reimer, E. (1992). The influence of air and sea exchange on the carbon isotope distribution in the sea. *Global Biogeochemical Cycles*, 6(3), 315–320.

Bromwich, D. H. (1988). Snowfall in High Southern Latitudes. *Reviews of Geophysics*, 26(1), 149–168.

Brovkin, V., Ganopolski, A., & Svirezhev, Y. (1997). A continuous climate-vegetation classification for use in climate-biosphere studies. *Ecological Modelling*, 101, 251–261.

Carlson, A. E. & Clark, P. U. (2012). Ice sheet sources of sea level rise and freshwater discharge during the last deglaciation. *Reviews of Geophysics*, 50, RG4007.

Chapman, M. R. & Shackleton, N. J. (1999). Global ice-volume fluctuations, North Atlantic ice-rafting events, and deep-ocean circulation changes between 130 and 70 ka. *Geology*, 27, 795–798.

Cheng, H., Edwards, R. L., Broecker, W. S., Denton, G. H., Kong, X., Wang, Y., Zhang, R., & Wang, X. (2009). Ice age terminations. *Science*, 326(5950), 248–52.

Chiang, J. C., Biasutti, M., & Battisti, D. S. (2003). Sensitivity of the Atlantic Intertropical Convergence Zone to Last Glacial Maximum boundary conditions. *Paleoceanography*, 18(4), 1–18.

Chiang, J. C. & Bitz, C. M. (2005). Influence of high latitude ice cover on the marine Intertropical Convergence Zone. *Climate Dynamics*, 25(5), 477–496.

Chiang, J. C. & Friedman, A. R. (2012). Extratropical cooling, interhemispheric thermal gradients, and tropical climate change. *Annual Review of Earth and Planetary Sciences*, 40(1), 383–412.

Chiang, J. C., Kushnir, Y., & Giannini, A. (2002). Deconstructing Atlantic Intertropical Convergence Zone variability: Influence of the local cross-equatorial sea surface temperature gradient and remote forcing from the eastern equatorial Pacific. *Journal of Geophysical Research*, 107(D1), 4004.

Chiang, J. C. H., Zebiak, S. E., & Cane, M. A. (2001). Relative roles of elevated heating and surface temperature gradients in driving anomalous surface winds over tropical oceans. *Journal of Atmospheric Sciences*, 58, 1371–1394.

Chikamoto, Y., Timmermann, A., Stevenson, S., DiNezio, P., & Langford, S. (2015). Decadal predictability of soil water, vegetation, and wildfire frequency over North America. *Climate Dynamics*.

Church, J., Clark, P., Cazenave, A., Gregory, J., Jevrejeva, S., Levermann, A., Merrifield, M., Milne, G., Nerem, R., Nunn, P., Payne, A., Pfeffer, W., Stammer, D., & Unnikrishnan, A. (2013). Sea level change. In T. F. Stocker, D. Qin, G.-K. Plattner, M. Tignor, S. Allen, J. Boschung, A. Nauels, Y. Xia, V. Bex, & P. Midgley (Eds.), *Climate Change 2013: The Physical Science Basis. Contribution of Working Group I to the Fifth Assessment Report of the Intergovernmental Panel on Climate Change* (pp. 1137–1216). Cambridge, United Kingdom and New York, NY, USA: Cambridge University Press.

Clark, P. U., Archer, D., Pollard, D., Blum, J. D., Rial, J. A., Brovkin, V., Mix, A. C., Pisias, N. G., & Roy, M. (2006). The middle Pleistocene transition: characteristics, mechanisms, and implications for long-term changes in atmospheric pCO2. *Quaternary Science Reviews*, 25(23-24), 3150–3184.

Claussen, M., Fohlmeister, J., Ganopolski, A., & Brovkin, V. (2006). Vegetation dynamics amplifies precessional forcing. *Geophysical Research Letters*, 33(9), 2–5.

Clemens, S. C., Prell, W. L., & Sun, Y. (2010). Orbital-scale timing and mechanisms driving Late Pleistocene Indo-Asian summer monsoons: Reinterpreting cave speleothem δ^{18}O. *Paleoceanography*, 25(4), 1–19.

Clemens, S. C. & Tiedemann, R. (1997). Eccentricity forcing of Pliocene-Early Pleistocene climate revealed in a marine oxygen-isotope record. *Nature*, 385, 801–804.

Clement, A. C., Hall, A., & Broccoli, A. J. (2004). The importance of precessional signals in the tropical climate. *Climate Dynamics*, 22(4), 327–341.

Comiso, J. C. (2000). Variability and trends in Antarctic surface temperatures from In Situ and satellite infrared measurements. *Journal of Climate*, 13(10), 1674–1696.

Cortese, G., Abelmann, A., & Gersonde, R. (2007). The last five glacial-interglacial transitions: A high-resolution 450,000-year record from the subantarctic Atlantic. *Paleoceanography*, 22(4), 1–14.

Coxall, H. K. & Pearson, P. N. (2007). The Eocene-Oligocene transition. In M. Williams, A. M. Haywood, F. J. Gregory, & D. N. Schmidt (Eds.), *Deep-time perspectives on climate change: Marrying the signal from computer models and biological proxies* (pp. 351–387). The Micropaleontological Society Special Publications.

Cruz, F. W., Burns, S. J., Karmann, I., Sharp, W. D., Vuillen, M., Cardoso, A. O., Ferrari, J. A., Silva Dias, P. L., & Viana Jr, O. (2005). Insolation-driven changes in atmospheric circulation over the past 116,000 years in subtropical Brazil. *Nature*, 434, 63–66.

Curry, W. B. & Oppo, D. W. (1997). Synchronous, high-frequency oscillations in tropical sea surface temperatures and North Atlantic Deep Water production during the last glacial cycle. *Paleoceanography*, 12(1), 1–14.

Dansgaard, W., Johnsen, S. J., Clausen, H. B., Dahl-Jensen, D., Gundestrup, N., Hammer, C. U., & Oeschger, H. (1984). North Atlantic climatic oscillations revealed by deep Greenland ice cores BT - Climate Processes and Climate Sensitivity. *Climate Processes and Climate Sensitivity*, 29, 288–298.

Davies, B. J., Hambrey, M. J., Smellie, J. L., Carrivick, J. L., & Glasser, N. F. (2012). Antarctic Peninsula Ice Sheet evolution during the Cenozoic Era. *Quaternary Science Reviews*, 31, 30–66.

de Boer, B., Wal, R. S. W., Lourens, L. J., Bintanja, R., Reerink, T. J., de Boer, B., & van de Wal, R. S. W. (2012). A continuous simulation of global ice volume over the past 1 million years with 3-D ice-sheet models. *Climate Dynamics*, 41(5-6), 1365–1384.

De Rydt, J., Holland, P. R., Dutrieux, P., & Jenkins, A. (2014). Geometric and oceanographic controls on melting beneath Pine Island Glacier. *Journal of Geophysical Research: Oceans*, 119(4), 2420–2438.

DeConto, R. M. & Pollard, D. (2003). Rapid Cenozoic glaciation of Antarctica induced by declining atmospheric CO2. *Nature*, 421(6920), 245–9.

DeMenocal, P. B., Ortiz, J., Guilderson, T., Adkins, J., Sarnthein, M., Baker, L., & Yarusinsky, M. (2000). Abrupt onset and termination of the African Humid Period: rapid climate responses to gradual insolation forcing. *Quaternary Science Reviews*, 19, 347–361.

Denison, S. M., Maslin, M. A., Boot, C., Pancost, R. D., & Ettwein, V. J. (2005). Precession-forced changes in South West African vegetation during Marine Isotope Stages 101-100 (~2.56-2.51 Ma). *Palaeogeography, Palaeoclimatology, Palaeoecology*, 220(3-4), 375–386.

Denton, G. H., Anderson, R. F., Toggweiler, J. R., Edwards, R. L., Schaefer, J. M., & Putnam, a. E. (2010). The last glacial termination. *Science*, 328(5986), 1652–1656.

Denton, G. H. & Hughes, T. J. (2002). Reconstructing the Antarctic Ice Sheet at the Last Glacial Maximum. *Quaternary Science Reviews*, 21, 193–202.

Deplazes, G., Lückge, A., Peterson, L. C., Timmermann, A., Hamann, Y., Hughen, K. a., Röhl, U., Laj, C., Cane, M. a., Sigman, D. M., & Haug, G. H. (2013). Links between tropical rainfall and North Atlantic climate during the last glacial period. *Nature Geoscience*, 6(3), 213–217.

Deser, C., Tomas, R. A., & Sun, L. (2015). The role of ocean-atmosphere coupling in the zonal mean atmospheric response to Arctic sea ice loss. *Journal of Climate*, 28, 2168–2186.

DiNezio, P., Clement, A. C., Vecchi, G. A., Soden, B. J., Broccoli, A. J., Otto-Bliesner, B. L., & Braconnot, P. (2011). The response of the Walker circulation to Last Glacial Maximum forcing: Implications for detection in proxies. *Paleoceanography*, 26(3), 1–21.

Donohoe, A., Marshall, J., Ferreira, D., Mcgee, D., & Sciences, P. (2013). The relationship between ITCZ location and cross-equatorial atmospheric heat transport : From the seasonal cycle to the Last Glacial Maximum. *Journal of Climate*, 26(11), 3597–3618.

Dutton, A., Carlson, A. E., Long, A. J., Milne, G. A., Clark, P. U., DeConto, R. M., Horton, B. P., Rahmstorf, S., & Raymo, M. E. (2015). Sea-level rise due to polar ice-sheet mass loss during past warm periods. *Science*, 349(6244), 153–162.

Dykoski, C. A., Edwards, R. L., Cheng, H., Yuan, D., Cai, Y., Zhang, M., Lin, Y., Qing, J., An, Z., & Revenaugh, J. S. (2005). A high-resolution, absolute-dated Holocene and deglacial Asian monsoon record from Dongge Cave, China. *Earth and Planetary Science Letters*, 233(1-2), 71–86.

EPICA Community Members (2004). Eight glacial cycles from an Antarctic ice core. *Nature*, 429(6992), 623–8.

EPICA Community Members (2006). One-to-one coupling of glacial climate variability in Greenland and Antarctica. *Nature*, 444(7116), 195–198.

Erb, M. P., Broccoli, A. J., & Clement, A. C. (2013). The contribution of radiative feedbacks to orbitally-driven climate change. *Journal of Climate*, 26(16), 5897–5914.

Fretwell, P., Pritchard, H. D., Vaughan, D. G., Bamber, J. L., Barrand, N. E., Bell, R., Bianchi, C., Bingham, R. G., Blankenship, D. D., Casassa, G., Catania, G., Callens, D., Conway, H., Cook, a. J., Corr, H. F. J., Damaske, D., Damm, V., Ferraccioli, F., Forsberg, R., Fujita, S., Gim, Y., Gogineni, P., Griggs, J. a., Hindmarsh, R. C. a., Holmlund, P., Holt, J. W., Jacobel, R. W., Jenkins, a., Jokat, W., Jordan, T., King, E. C., Kohler, J., Krabill, W., Riger-Kusk, M., Langley, K. a., Leitchenkov, G., Leuschen, C., Luyendyk, B. P., Matsuoka, K., Mouginot, J., Nitsche, F. O., Nogi, Y., Nost, O. a., Popov, S. V., Rignot, E., Rippin, D. M., Rivera, a., Roberts, J., Ross, N., Siegert, M. J., Smith, a. M., Steinhage, D., Studinger, M., Sun, B., Tinto, B. K., Welch, B. C., Wilson, D., Young, D. a., Xiangbin, C., & Zirizzotti, a. (2013). Bedmap2: Improved ice bed, surface and thickness datasets for Antarctica. *Cryosphere*, 7(1), 375–393.

Friedrich, T., Timmermann, A., Menviel, L., Timm, O. E., Mouchet, A., & Roche, D. M. (2010). The mechanism behind internally generated centennial-to-millennial scale climate variability in an earth system model of intermediate complexity. *Geoscientific Model Development*, 3(2), 377–389.

Frieler, K., Clark, P. U., He, F., Buizert, C., Reese, R., Ligtenberg, S. R. M., van den Broeke, M. R., Winkelmann, R., & Levermann, A. (2015). Consistent evidence of increasing Antarctic accumulation with warming. *Nature Climate Change*, 5(4), 348–352.

Fritz, S. C., Baker, P. A., Lowenstein, T. K., Seltzer, G. O., Rigsby, C. A., Dwyer, G. S., Tapia, P. M., Arnold, K. K., Ku, T.-L., & Luo, S. (2004). Hydrologic variation during the last 170,000 years in the southern hemisphere tropics of South America. *Quaternary Research*, 61(1), 95–104.

Fučkar, N. S., Xie, S.-P. P., Farneti, R., Maroon, E. A., & Frierson, D. M. W. (2013). Influence of the extratropical ocean circulation on the intertropical convergence zone in an idealized coupled general circulation model. *Journal of Climate*, 26(13), 4612–4629.

Ganopolski, A. & Calov, R. (2011). The role of orbital forcing, carbon dioxide and regolith in 100 kyr glacial cycles. *Climate of the Past*, 7(4), 1415–1425.

Ganopolski, A., Calov, R., & Claussen, M. (2010). Simulation of the last glacial cycle with a coupled climate ice-sheet model of intermediate complexity. *Climate of the Past*, 6, 229–244.

Ganopolski, A. & Robinson, A. (2011). Palaeoclimate: The past is not the future. *Nature Geoscience*, 4(10), 661–663.

Gasse, F. (2000). Hydrological changes in the African tropics since the Last Glacial Maximum. *Quaternary Science Reviews*, 19(1-5), 189–211.

Gent, P. R., Danabasoglu, G., Donner, L. J., Holland, M. M., Hunke, E. C., Jayne, S. R., Lawrence, D. M., Neale, R. B., Rasch, P. J., Vertenstein, M., Worley, P. H., Yang, Z.-L., & Zhang, M. (2011). The Community Climate System Model version 4. *Journal of Climate*, 24(19), 4973–4991.

Gersonde, R., Crosta, X., Abelmann, A., & Armand, L. (2005). Sea-surface temperature and sea ice distribution of the Southern Ocean at the EPILOG Last Glacial MaximumâĂŤa circum-Antarctic view based on siliceous microfossil records. *Quaternary Science Reviews*, 24(7-9), 869–896.

Gildor, H. & Tziperman, E. (2001). A sea ice climate switch mechanism for the 100-kyr glacial cycles seas. *Journal of Geophysical Research*, 106(C5), 9117–9133.

Gill, A. E. (1980). Some simple solutions for heat-induced tropical circulation. *Quarterly Journal of the Royal Meteorological Society*, 106(449), 447–462.

Golledge, N. R., Fogwill, C. J., Mackintosh, A. N., & Buckley, K. M. (2012). Dynamics of the last glacial maximum Antarctic ice-sheet and its response to ocean forcing. *Proceedings of the National Academy of Sciences*, 109(40), 16052–16056.

Golledge, N. R., Menviel, L., Carter, L., Fogwill, C. J., England, M. H., Cortese, G., & Levy, R. H. (2014). Antarctic contribution to meltwater pulse 1A from reduced Southern Ocean overturning. *Nature Communications*, 5, 5107.

Goosse, H., Brovkin, V., Fichefet, T., Haarsma, R., Huybrechts, P., Jongma, J. I., Mouchet, A., Selten, F., Barriat, P.-Y., Campin, J.-M., Deleersnijder, E., Driesschaert, E., Goelzer, H., Janssens, I., Loutre, M.-F., Morales Maqueda, M. A., Opsteegh, T., Mathieu, P.-P., Munhoven, G., Pettersson, E. J., Renssen, H., Roche, D. M., Schaeffer, M., Tartinville, B., Timmermann, A., & Weber, S. L. (2010). Description of the Earth system Model of Intermediate Complexity LOVECLIM version 1.2. *Geoscientific Model Development*, 3(2), 603–633.

Goosse, H. & Fichefet, T. (1999). Importance of ice-ocean interactions for the global ocean circulation: A model study. *Journal of Geophysical Research*, 104(C10), 23337–23355.

Hargreaves, J. C., Annan, J. D., Yoshimori, M., & Abe-Ouchi, A. (2012). Can the Last Glacial Maximum constrain climate sensitivity? *Geophysical Research Letters*, 39(24), L24702.

Haug, G. H. & Tiedemann, R. (1998). Effect of the formation of the Isthmus of Panama on Atlantic Ocean thermohaline circulation. *Nature*, 393, 673–676.

Haywood, a. M., Hill, D. J., Dolan, a. M., Otto-Bliesner, B. L., Bragg, F., Chan, W.-L., Chandler, M. a., Contoux, C., Dowsett, H. J., Jost, a., Kamae, Y., Lohmann, G., Lunt, D. J., Abe-Ouchi, A., Pickering, S. J., Ramstein, G., Rosenbloom, N. a., Salzmann, U., Sohl, L., Stepanek, C., Ueda, H., Yan, Q., & Zhang, Z. (2013). Large-scale features of Pliocene climate: results from the Pliocene Model Intercomparison Project. *Climate of the Past*, 9(1), 191–209.

He, F., Shakun, J. D., Clark, P. U., Carlson, A. E., Liu, Z., Otto-Bliesner, B. L., & Kutzbach, J. E. (2013). Northern Hemisphere forcing of Southern Hemisphere climate during the last deglaciation. *Nature*, 494(7435), 81–5.

Heinemann, M., Timmermann, A., Timm, O. E., Saito, F., & Abe-Ouchi, A. (2014). Deglacial ice sheet meltdown: orbital pacemaking and CO_2 effects. *Climate of the Past*, 10(4), 1567–1579.

Heinrich, H. (1988). Origin and consequences of cyclic ice rafting in the Northeast Atlantic Ocean during the past 130,000 years. *Quaternary Research*, 29(2), 142–152.

Held, I. M. & Soden, B. J. (2006). Robust responses of the hydrological cycle to global warming. *Journal of Climate*, 19(21), 5686–5699.

Hellmer, H. H., Kauker, F., Timmermann, R., Determann, J., & Rae, J. (2012). Twenty-first-century warming of a large Antarctic ice-shelf cavity by a redirected coastal current. *Nature*, 485(7397), 225–8.

Herbert, T. D. (1997). A long marine history of carbon cycle modulation by orbital-climatic changes. *Proceedings of the National Academy of Sciences*, 94(16), 8362–9.

Hilgen, F. J. (1991). Astronomical calibration of Gauss to Matuyama sapropels in the Mediterranean and implication for the Geomagnetic Polarity Time Scale. *Earth and Planetary Science Letters*, 104(2-4), 226–244.

Ho, S. L., Mollenhauer, G., Lamy, F., Martínez-Garcia, A., Mohtadi, M., Gersonde, R., Hebbeln, D., Nunez-Ricardo, S., Rosell-Melé, A., & Tiedemann, R. (2012). Sea surface temperature variability in the Pacific sector of the Southern Ocean over the past 700 kyr. *Paleoceanography*, 27, 1–15.

Holland, P. R., Jenkins, A., & Holland, D. M. (2008). The Response of Ice Shelf Basal Melting to Variations in Ocean Temperature. *Journal of Climate*, 21(11), 2558–2572.

Hurrell, J. W., Holland, M. M., Gent, P. R., Ghan, S., Kay, J. E., Kushner, P. J., Lamarque, J.-F., Large, W. G., Lawrence, D., Lindsay, K., Lipscomb, W. H., Long, M. C., Mahowald, N., Marsh, D. R., Neale, R. B., Rasch, P., Vavrus, S., Vertenstein, M., Bader, D., Collins, W. D., Hack, J. J., Kiehl, J., & Marshall, S. (2013). The Community Earth System Model: A Framework for Collaborative Research. *Bulletin of the American Meteorological Society*, 94(9), 1339–1360.

Huybers, P. (2009). AntarcticaâĂŹs Orbital Beat. *Science*, 325, 1085–1086.

Huybers, P. & Denton, G. H. (2008). Antarctic temperature at orbital timescales controlled by local summer duration. *Nature Geoscience*, 1(11), 787–792.

Huybers, P. & Wunsch, C. (2003). Rectification and precession signals in the climate system. *Geophysical Research Letters*, 30(19), 1–4.

Huybrechts, P. (2002). Sea-level changes at the LGM from ice-dynamic reconstructions of the Greenland and Antarctic ice sheets during the glacial cycles. *Quaternary Science Reviews*, 21(1-3), 203–231.

Huybrechts, P., Gregory, J., Janssens, I., & Wild, M. (2004). Modelling Antarctic and Greenland volume changes during the 20th and 21st centuries forced by GCM time slice integrations. *Global and Planetary Change*, 42(1-4), 83–105.

Imbrie, J., Berger, A. L., Boyle, E. A., Clemens, S. C., Duffy, A., Howard, W. R., Kukla, G., Kutzbach, J. E., Martinson, D. G., McIntyre, A., Mix, A. C., Molfino, B., Morley, J. J., Peterson, L. C., Pisias, N. G., Prell, W. L., Raymo, M. E., Shackleton, N. J., & Toggweiler, J. R. (1993). On the structure and origin of major glaciation cycles. 2. The 100,000-year cycle. *Paleoceanography*, 8(6), 699–735.

Imbrie, J. & Imbrie, J. Z. (1980). Modeling the climatic response to orbital variations. *Science*, 207(4434), 943–953.

Jacobs, S. S., Helmer, H. H., Doake, C. S. M., Jenkins, A., & Frolich, R. M. (1992). Melting of ice shelves and the mass balance of Antarctica. *Journal of Glaciology*, 38(130), 375–387.

Jacobs, S. S., Jenkins, A., Giulivi, C. F., & Dutrieux, P. (2011). Stronger ocean circulation and increased melting under Pine Island Glacier ice shelf. *Nature Geoscience*, 4(8), 519–523.

Joughin, I. & Alley, R. B. (2011). Stability of the West Antarctic ice sheet in a warming world. *Nature Geoscience*, 4(8), 506–513.

Jouzel, J., Masson-Delmotte, V., Cattani, O., Dreyfus, G., Falourd, S., Hoffmann, G., Minster, B., Nouet, J., Barnola, J.-M., Chappellaz, J., Fischer, H., Gallet, J. C., Johnsen, S. J., Leuenberger, M., Loulergue, L., Luethi, D., Oerter, H., Parrenin, F., Raisbeck, G., Raynaud, D., Schilt, A., Schwander, J., Selmo, E., Souchez, R., Spahni, R., Stauffer, B., Steffensen, J. P., Stenni, B., Stocker, T. F., Tison, J.-L., Werner, M., & Wolff, E. W. (2007). Orbital and millennial Antarctic climate variability over the past 800,000 years. *Science*, 317(5839), 793–6.

Justino, F., Timmermann, A., Merkel, U., & Souza, E. P. (2005). Synoptic reorganization of atmospheric flow during the Last Glacial Maximum. *Journal of Climate*, 18(15), 2826–2846.

Kang, S. M., Frierson, D. M. W., & Held, I. M. (2009). The Tropical Response to Extratropical Thermal Forcing in an Idealized GCM: The Importance of Radiative Feedbacks and Convective Parameterization. *Journal of the Atmospheric Sciences*, 66(9), 2812–2827.

Kang, S. M., Held, I. M., Frierson, D. M. W., & Zhao, M. (2008). The response of the ITCZ to extratropical thermal forcing: Idealized slab-ocean experiments with a GCM. *Journal of Climate*, 21(14), 3521–3532.

Kang, S. M., Held, I. M., & Xie, S.-P. (2014). Contrasting the tropical responses to zonally asymmetric extratropical and tropical thermal forcing. *Climate Dynamics*, 42(7-8), 2033–2043.

Kawamura, K., Parrenin, F., Lisiecki, L. E., Uemura, R., Vimeux, F., Severinghaus, J. P., Hutterli, M. A., Nakazawa, T., Aoki, S., Jouzel, J., Raymo, M. E., Matsumoto, K., Nakata, H., Motoyama, H., Fujita, S., Goto-Azuma, K., Fujii, Y., & Watanabe, O. (2007). Northern Hemisphere forcing of climatic cycles in Antarctica over the past 360,000 years. *Nature*, 448(7156), 912–6.

Kennett, J. P. & Stott, L. D. (1991). Abrupt deep-sea warming, palaeoceanographic changes and benthic extinctions at the end of the Palaeocene. *Nature*, 353, 225–229.

Khon, V. C., Park, W., Latif, M., Mokhov, I. I., & Schneider, B. (2010). Response of the hydrological cycle to orbital and greenhouse gas forcing. *Geophysical Research Letters*, 37(19), L19705.

Khon, V. C., Park, W., Latif, M., Mokhov, I. I., & Schneider, B. (2012). Tropical circulation and hydrological cycle response to orbital forcing. *Geophysical Research Letters*, 39(15), L15708.

Knies, J., Matthiessen, J., Mackensen, A., Stein, R., Vogt, C., Frederichs, T., & Nam, S.-I. (2007). Effects of Arctic freshwater forcing on thermohaline circulation during the Pleistocene. *Geology*, 35(12), 1075–1078.

Knies, J. & Vogt, C. (2003). Freshwater pulses in the eastern Arctic Ocean during Saalian and Early Weichselian ice-sheet collapse. *Quaternary Research*, 60(3), 243–251.

Koenig, S. J., DeConto, R. M., & Pollard, D. (2011). Late Pliocene to Pleistocene sensitivity of the Greenland Ice Sheet in response to external forcing and internal feedbacks. *Climate Dynamics*, 37(5-6), 1247–1268.

Kohfeld, K. E. & Harrison, S. P. (2001). DIRTMAP: The geological record of dust. *Earth-Science Reviews*, 54(1-3), 81–114.

Köhler, P., Bintanja, R., Fischer, H., Joos, F., Knutti, R., Lohmann, G., & Masson-Delmotte, V. (2010). What caused Earth's temperature variations during the last 800,000 years? Data-based evidence on radiative forcing and constraints on climate sensitivity. *Quaternary Science Reviews*, 29(1-2), 129–145.

Krebs, U. & Timmermann, A. (2007). Tropical air-sea interactions accelerate the recovery of the Atlantic Meridional Overturning Circulation after a major shutdown. *Journal of Climate*, 20(19), 4940–4956.

Kuechler, R., Schefuß, E., Beckmann, B., Dupont, L., & Wefer, G. (2013). NW African hydrology and vegetation during the Last Glacial cycle reflected in plant-wax-specific hydrogen and carbon isotopes. *Quaternary Science Reviews*, 82, 56–67.

Kusahara, K., Sato, T., Oka, A., Obase, T., Greve, R., Abe-Ouchi, A., & Hasumi, H. (2015). Modelling the Antarctic marine cryosphere at the Last Glacial Maximum. *Annals of Glaciology*, 56(69), 425–435.

Kutzbach, J. E. & Guetter, P. J. (1986). The influence of changing orbital parameters and surface boundary conditions on climate simulations for the past 18000 years. *Journal of the Atmospheric Sciences*, 43(16), 1726–1759.

Kutzbach, J. E., Liu, X., Liu, Z., & Chen, G. (2008). Simulation of the evolutionary response of global summer monsoons to orbital forcing over the past 280,000 years. *Climate Dynamics*, 30(6), 567–579.

Kutzbach, J. E. & Liu, Z. (1997). Response of the African monsoon to orbital forcing and ocean feedbacks in the middle Holocene. *Science*, 278(5337), 440–443.

Kutzbach, J. E. & Otto-Bliesner, B. L. (1982). The sensitivity of the African-Asian monsoonal climate to orbital parameter changes for 9000 years B.P. in a low-resolution General Circulation Model. *Journal of the Atmospheric Sciences*, 39(6), 1177–1188.

Laepple, T. & Lohmann, G. (2009). Seasonal cycle as template for climate variability on astronomical timescales. *Paleoceanography*, 24(4), 1–15.

Laepple, T., Werner, M., & Lohmann, G. (2011). Synchronicity of Antarctic temperatures and local solar insolation on orbital timescales. *Nature*, 471(7336), 91–4.

Laskar, J., Robutel, P., Joutel, F., Gastineau, M., Correia, A. C. M., & Levrard, B. (2004). A long-term numerical solution for the insolation quantities of the Earth. *Astronomy & Astrophysics*, 428(1), 261–285.

Le Brocq, A. M., Payne, A. J., & Vieli, A. (2010). An improved Antarctic dataset for high resolution numerical ice sheet models (ALBMAPv1). *Earth System Science Data*, 2, 247–260.

Lindzen, R. S. & Hou, A. Y. (1988). Hadley circulations for zonally averaged heating centered off the equator. *Journal of the Atmospheric Sciences*, 45(17), 2416–2427.

Lindzen, R. S. & Nigam, S. (1987). On the role of sea surface temperature gradients in forcing low-level winds and convergence in the Tropics. *Journal of the Atmospheric Sciences*, 44(17), 2418–2436.

Lisiecki, L. E. & Raymo, M. E. (2005). A Pliocene-Pleistocene stack of 57 globally distributed benthic $\delta^{18}O$ records. *Paleoceanography*, 20(1), 1–17.

Lisiecki, L. E. & Raymo, M. E. (2007). Plio-Pleistocene climate evolution: trends and transitions in glacial cycle dynamics. *Quaternary Science Reviews*, 26(1-2), 56–69.

Liu, X. & Shi, Z. (2009). Effect of precession on the Asian summer monsoon evolution: A systematic review. *Chinese Science Bulletin*, 54(20), 3720–3730.

Liu, Z., Pagani, M., Zinniker, D., DeConto, R. M., Huber, M., Brinkhuis, H., Shah, S. R., Leckie, R. M., & Pearson, A. (2009). Global cooling during the Eocene-Oligocene climate transition. *Science*, 323(5918), 1187–90.

Locarnini, R. A., Mishonov, A. V., Antonov, J. I., Boyer, T. P., Garcia, H. E., Baranova, O. K., Zweng, M. M., & Johnson, D. R. (2010). World Ocean Atlas 2009, Volume 1: Temperature. In S. Levitus (Ed.), *NOAA Atlas NESDIS 68*. U.S. Government Printing Office.

Loulergue, L., Schilt, A., Spahni, R., Masson-Delmotte, V., Blunier, T., Lemieux, B., Barnola, J.-M., Raynaud, D., Stocker, T. F., & Chappellaz, J. (2008). Orbital and millennial-scale features of atmospheric CH_4 over the past 800,000 years. *Nature*, 453(7193), 383–6.

Lourens, L. J., Antonarakou, A., Hilgen, F. J., van Hoof, A. A. M., Vergnaud-Grazzini, C., & Zachariasse, W. J. (1996). Evaluation of the Plio-Pleistocene astronomical timescale. *Paleoceanography*, 11(4), 391–413.

Lüthi, D., Le Floch, M., Bereiter, B., Blunier, T., Barnola, J.-M., Siegenthaler, U., Raynaud, D., Jouzel, J., Fischer, H., Kawamura, K., & Stocker, T. F. (2008). High-resolution carbon dioxide concentration record 650,000-800,000 years before present. *Nature*, 453(7193), 379–82.

Ma, W., Tian, J., Li, Q., & Wang, P. (2011). Simulation of long eccentricity (400-kyr) cycle in ocean carbon reservoir during Miocene Climate Optimum: Weathering and nutrient response to orbital change. *Geophysical Research Letters*, 38(10), 1–5.

Mackintosh, A., Golledge, N., Domack, E., Dunbar, R., Leventer, A., White, D., Pollard, D., DeConto, R., Fink, D., Zwartz, D., Gore, D., & Lavoie, C. (2011). Retreat of the East Antarctic ice sheet during the last glacial termination. *Nature Geoscience*, 4(3), 195–202.

Mackintosh, A. N., Verleyen, E., O'Brien, P. E., White, D. a., Jones, R. S., McKay, R., Dunbar, R., Gore, D. B., Fink, D., Post, A. L., Miura, H., Leventer, A., Goodwin, I., Hodgson, D. a., Lilly, K., Crosta, X., Golledge, N. R., Wagner, B., Berg, S., van Ommen, T., Zwartz, D., Roberts, S. J., Vyverman, W., & Masse, G. (2013). Retreat history of the East Antarctic Ice Sheet since the Last Glacial Maximum. *Quaternary Science Reviews*, 100, 10–30.

Marino, G., Rohling, E. J., Rodríguez-Sanz, L., Grant, K. M., Heslop, D., Roberts, a. P., Stanford, J. D., & Yu, J. (2015). Bipolar seesaw control on last interglacial sea level. *Nature*, 522(7555), 197–201.

Maris, M. N. A., de Boer, B., Ligtenberg, S. R. M., Crucifix, M., van de Berg, W. J., & Oerlemans, J. (2014). Modelling the evolution of the Antarctic ice sheet since the last interglacial. *The Cryosphere*, 8(4), 1347–1360.

Maris, M. N. A., de Boer, B., & Oerlemans, J. (2012). A climate model intercomparison for the Antarctic region: present and past. *Climate of the Past*, 8(2), 803–814.

Maris, M. N. A., van Wessem, J. M., van de Berg, W. J., de Boer, B., & Oerlemans, J. (2015). A model study of the effect of climate and sea-level change on the evolution of the Antarctic Ice Sheet from the Last Glacial Maximum to 2100. *Climate Dynamics*, 45(3-4), 837–851.

Marshall, J., Armour, K. C., Scott, J. R., Kostov, Y., Hausmann, U., Ferreira, D., Shepherd, T. G., & Bitz, C. M. (2014). The ocean's role in polar climate change: asymmetric Arctic and Antarctic responses to greenhouse gas and ozone forcing. *Philosphical Transactions of the Royal Society A*, 372, 20130040.

Marshall, J., Kushnir, Y., Battisti, D. S., Chang, P., Czaja, A., Dickson, R., Hurrell, J., McCartney, M., Saravanan, R., & Visbeck, M. (2001). North Atlantic climate variability: phenomena, impacts and mechanisms. *International Journal of Climatology*, 21(15), 1863–1898.

Martin, M. A., Winkelmann, R., Haseloff, M., Albrecht, T., Bueler, E., Khroulev, C., & Levermann, A. (2011). The Potsdam Parallel Ice Sheet Model (PISM-PIK) âĂŞ Part 2: Dynamic equilibrium simulation of the Antarctic ice sheet. *The Cryosphere*, 5(3), 727–740.

Martínez-Garcia, A., Rosell-Melé, A., Geibert, W., Gersonde, R., Masqué, P., Gaspari, V., & Barbante, C. (2009). Links between iron supply, marine productivity, sea surface temperature, and CO2 over the last 1.1 Ma. *Paleoceanography*, 24(1), 1–14.

Marzin, C., Braconnot, P., & Kageyama, M. (2013). Relative impacts of insolation changes, meltwater fluxes and ice sheets on African and Asian monsoons during the Holocene. *Climate Dynamics*.

Maslin, M. A., Li, X. S., Loutre, M. F., & Berger, A. (1998). The contribution of orbital forcing to the progressive intensification of Northern Hemisphere glaciation. *Quaternary Science Reviews*, 17(4-5), 411–426.

Masson-Delmotte, V., Schulz, M., Abe-Ouchi, A., Beer, J., Ganopolski, A., Gonzalez Rouco, J. F., Jansen, E., Lambeck, K., Luterbacher, J., Naish, T. R., Osborn, T., Otto-Bliesner, B. L., Quinn, T., Ramesh, R., Rojas, M., Shao, X., & Timmermann, A. (2013). Information from Paleoclimate Archives. In T. F. Stocker, D. Qin, G.-K. Plattner, M. Tignor, S. K. Allen, J. Boschung, A. Nauels, Y. Xia, V. Bex, & P. M. Midgley (Eds.), *Climate Change 2013: The Physical Science Basis. Contribution of Working Group I to the Fifth Assessment Report of the Intergovernmental Panel on Climate Change* (pp. 383–464). Cambridge, United Kingdom and New York, NY, USA: Cambridge University Press.

McKay, R. M., Naish, T. R., Powell, R. D., Barrett, P. J., Scherer, R. P., Talarico, F., Kyle, P., Monien, D., Kuhn, G., Jackolski, C., & Williams, T. (2012). Pleistocene variability of Antarctic Ice Sheet extent in the Ross Embayment. *Quaternary Science Reviews*, 34, 93–112.

Menviel, L. (2008). *Climate-carbon cycle interactions on millennial to glacial timescales as simulated by a model of intermediate complexity*. PhD thesis, University of Hawaii.

Menviel, L., Timmermann, A., Friedrich, T., & England, M. H. (2014). Hindcasting the continuum of DansgaardâĂŞ-Oeschger variability: mechanisms, patterns and timing. *Climate of the Past*, 10(1), 63–77.

Menviel, L., Timmermann, A., Timm, O. E., & Mouchet, a. (2010). Climate and biogeochemical response to a rapid melting of the West Antarctic Ice Sheet during interglacials and implications for future climate. *Paleoceanography*, 25(4), 1–12.

Menviel, L., Timmermann, A., Timm, O. E., & Mouchet, A. (2011). Deconstructing the Last Glacial termination: the role of millennial and orbital-scale forcings. *Quaternary Science Reviews*, 30(9-10), 1155–1172.

Merlis, T. M., Schneider, T., Bordoni, S., & Eisenman, I. (2013). The tropical precipitation response to orbital precession. *Journal of Climate*, 26(6), 2010–2021.

Milankovitch, M. (1941). Kanon der Erdbestrahlung und seine Anwendung auf das Eiszeitenproblem. In *Royal Serbian Academy Special Publication 132*, volume 33 (pp. 633). Belgrade: Royal Serbian Academy.

Mitchell, T. P. & Wallace, J. M. (1992). The annual cycle in equatorial convection and sea surface temperature. *Journal of Climate*, 5, 1140–1156.

Mix, A. C., Harris, S. E., & Janecek, T. R. (1995). Estimating lithology from nonintrusive reflectance spectra: Leg 138. *Proceedings of the Ocean Drilling Program, Scientific Results*, 138, 413–427.

Moore, J. K., Lindsay, K., Doney, S. C., Long, M. C., & Misumi, K. (2013). Marine Ecosystem Dynamics and Biogeochemical Cycling in the Community Earth System Model [CESM1(BGC)]: Comparison of the 1990s with the 2090s under the RCP4.5 and RCP8.5 Scenarios. *Journal of Climate*, 26(23), 9291–9312.

Neelin, J. D. & Held, I. M. (1987). Modeling tropical convergence based on the moist static energy budget. *Monthly Weather Review*, 115(1), 3–12.

Nick, F. M., Vieli, A., Andersen, M. L., Joughin, I., Payne, A., Edwards, T. L., Pattyn, F., & van de Wal, R. S. W. (2013). Future sea-level rise from Greenland's main outlet glaciers in a warming climate. *Nature*, 497(7448), 235–8.

Nobre, P. & Shukla, J. (1996). Variations of sea surface temperature, wind stress, and rainfall over the Tropical Atlantic and South America. *Journal of Climate*, 9, 2464–2479.

North Greenland Ice Core Project Members (2004). High-resolution record of Northern Hemisphere climate extending into the last interglacial period. *Nature*, 431(7005), 147–51.

Nürnberg, D. & Groeneveld, J. (2006). Pleistocene variability of the Subtropical Convergence at East Tasman Plateau: Evidence from planktonic foraminiferal Mg/Ca (ODP Site 1172A). *Geochemistry, Geophysics, Geosystems*, 7(4).

Oerlemans, J. (1982). Glacial cycles and ice-sheet modeling. *Climatic Change*, 4, 353–374.

Oppo, D. W., Keigwin, L. D., McManus, J. F., & Cullen, J. L. (2001). Persistent suborbital climate variability in marine isotope stage 5 and Termination II. *Paleoceanography*, 16(3), 280–292.

Oppo, D. W., McManus, J. F., & Cullen, J. L. (2006). Evolution and demise of the Last Interglacial warmth in the subpolar North Atlantic. *Quaternary Science Reviews*, 25(23-24), 3268–3277.

Opsteegh, J. D., Haarsma, R. J., Selten, F. M., & Kattenberg, A. (1998). ECBILT: A dynamic alternative to mixed boundary conditions in ocean models. *Tellus*, 50A(3), 348–367.

Overpeck, J. T., Otto-Bliesner, B. L., Miller, G. H., Muhs, D. R., Alley, R. B., & Kiehl, J. T. (2006). Paleoclimatic evidence for future ice-sheet instability and rapid sea-level rise. *Science*, 311(5768), 1747–1750.

Pagani, M., Zachos, J. C., Freeman, K. H., Tipple, B., & Bohaty, S. M. (2005). Marked decline in atmospheric carbon dioxide concentrations during the Paleogene. *Science*, 309(5734), 600–3.

Paillard, D. (1998). The timing of Pleistocene glaciations from a simple multiple-state climate model. *Nature*, 391, 916–918.

Paillard, D. (2001). Glacial cycles: toward a new paradigm. *Reviews of Geophysics*, 39(3), 325–346.

Paolo, F. S., Fricker, H. A., & Padman, L. (2015). Volume loss from Antarctic ice shelves is accelerating. *Science*, 348(6232), 327–332.

Parrenin, F., Masson-Delmotte, V., Köhler, P., Raynaud, D., Paillard, D., Schwander, J., Barbante, C., Landais, a., Wegner, A., & Jouzel, J. (2013). Synchronous change of atmospheric CO2 and Antarctic temperature during the last deglacial warming. *Science*, 339(6123), 1060–3.

Parrenin, F., Rémy, F., Ritz, C., Siegert, M. J., & Jouzel, J. (2004). New modeling of the Vostok ice flow line and implication for the glaciological chronology of the Vostok ice core. *Journal of Geophysical Research D: Atmospheres*, 109(20).

Peltier, W. R. (2004). Global glacial isostasy and the surface of the ice-age earth: The ICE-5G (VM2) model and GRACE. *Annual Review of Earth and Planetary Sciences*, 32(1), 111–149.

Petit, J.-R., Jouzel, J., Raynaud, D., Barkov, N. I., Barnola, J.-M., Basile, I., Benders, M., Chappellaz, J., Davis, M., Delaygue, G., Delmotte, M., Kotlyakov, V. M., Legrand, M., Lipenkov, V. Y., Lorius, C., Pépin, L., Ritz, C., Saltzman, E., & Stievenard, M. (1999). Climate and atmospheric history of the past 420,000 years from the Vostok ice core, Antarctica. *Nature*, 399, 429–436.

Pollard, D. & DeConto, R. M. (2009). Modelling West Antarctic ice sheet growth and collapse through the past five million years. *Nature*, 458(7236), 329–32.

Pollard, D. & DeConto, R. M. (2012a). A simple inverse method for the distribution of basal sliding coefficients under ice sheets, applied to Antarctica. *The Cryosphere*, 6(5), 953–971.

Pollard, D. & DeConto, R. M. (2012b). Description of a hybrid ice sheet-shelf model, and application to Antarctica. *Geoscientific Model Development*, 5(5), 1273–1295.

Pollard, D., DeConto, R. M., & Alley, R. B. (2015). Potential Antarctic Ice Sheet retreat driven by hydrofracturing and ice cliff failure. *Earth and Planetary Science Letters*, 412, 112–121.

Prell, W. L. & Kutzbach, J. E. (1987). Monsoon variability over the past 150,000 years. *Journal of Geophysical Research*, 92, 8411–8425.

Pritchard, H. D., Ligtenberg, S. R. M., Fricker, H. a., Vaughan, D. G., van den Broeke, M. R., & Padman, L. (2012). Antarctic ice-sheet loss driven by basal melting of ice shelves. *Nature*, 484(7395), 502–5.

Reeh, N. (1991). Parameterization of melt rate and surface temperature on the Greenland ice sheet. *Polarforschung*, 59(3), 113–128.

Rial, J. A., Pielke Sr., R. A., Beniston, M., Claussen, M., Canadell, J., Cox, P., Held, H., de Noblet-Ducoudré, N., Prinn, R., Reynolds, J. F., & Salas, J. D. (2004). Nonlinearities, feedbacks and critical thresholds within the Earth's climate system. *Climatic Change*, 65, 11–38.

Richter, I., Xie, S. P., Behera, S. K., Doi, T., & Masumoto, Y. (2014). Equatorial Atlantic variability and its relation to mean state biases in CMIP5. *Climate Dynamics*, 42(1-2), 171–188.

Richter, I., Xie, S.-P., Wittenberg, A. T., & Masumoto, Y. (2012). Tropical Atlantic biases and their relation to surface wind stress and terrestrial precipitation. *Climate Dynamics*, 38(5-6), 985–1001.

Rignot, E., Velicogna, I., van den Broeke, M. R., Monaghan, A., & Lenaerts, J. T. M. (2011). Acceleration of the contribution of the Greenland and Antarctic ice sheets to sea level rise. *Geophysical Research Letters*, 38(5), L05503.

Ritz, C., Rommelaere, V., & Dumas, C. (2001). Modeling the evolution of Antarctic ice sheet over the last 420,000 years: Implications for altitude changes in the Vostok region. *Journal of Geophysical Research*, 106(D23), 31943–31964.

Roche, D. M., Crosta, X., & Renssen, H. (2012). Evaluating Southern Ocean sea-ice for the Last Glacial Maximum and pre-industrial climates: PMIP-2 models and data evidence. *Quaternary Science Reviews*, 56, 99–106.

Roche, D. M., Dokken, T. M., Goosse, H., Renssen, H., & Weber, S. L. (2007). Climate of the Last Glacial Maximum: sensitivity studies and model-data comparison with the LOVECLIM coupled model. *Climate of the Past*, 3(2), 205–224.

Roe, G. H. & Lindzen, R. S. (2001). The mutual interaction between continental-scale ice sheets and atmospheric stationary waves. *Journal of Climate*, 14(7), 1450–1465.

Rohling, E. J., Rohling, E. J., Sluijs, A., Dijkstra, H. A., Köhler, P., van de Wal, R. S. W., von der Heydt, A. S., Beerling, D. J., Berger, A., Bijl, P. K., Crucifix, M., DeConto, R., Drijfhout, S. S., Fedorov, A., Foster, G. L., Ganopolski, A., Hansen, J., Hönisch, B., Hooghiemstra, H., Huber, M., Huybers, P., Knutti, R., Lea, D. W., Lourens, L. J., Lunt, D., Masson-Demotte, V., Medina-Elizalde, M., Otto-Bliesner, B., Pagani, M., Pälike, H., Renssen, H., Royer, D. L., Siddall, M., Valdes, P., Zachos, J. C., & Zeebe, R. E. (2012). Making sense of palaeoclimate sensitivity. *Nature*, 491(7426), 683–691.

Russon, T., Paillard, D., & Elliot, M. (2010). Potential origins of 400-500 kyr periodicities in the ocean carbon cycle: A box model approach. *Global Biogeochemical Cycles*, 24(2), 1–16.

Scherer, R. P., Aldahan, A., Tulaczyk, S., Engelhardt, H., & Kamb, B. (1998). Pleistocene Collapse of the West Antarctic Ice Sheet. *Science*, 281, 82–85.

Scherer, R. P., Bohaty, S. M., Dunbar, R., Esper, O., Flores, J. A., Gersonde, R., Harwood, D. M., Roberts, A. P., & Taviani, M. (2008). Antarctic records of precession-paced insolation-driven warming during early Pleistocene Marine Isotope Stage 31. *Geophysical Research Letters*, 35, 1–5.

Schmidt, G. A., Annan, J. D., Bartlein, P. J., Cook, B. I., Guilyardi, E., Hargreaves, J. C., Harrison, S. P., Kageyama, M., LeGrande, a. N., Konecky, B., Lovejoy, S., Mann, M. E., Masson-Delmotte, V., Risi, C., Thompson, D., Timmermann, A., Tremblay, L.-B., & Yiou, P. (2014). Using palaeo-climate comparisons to constrain future projections in CMIP5. *Climate of the Past*, 10(1), 221–250.

Schmidt, M. W., Spero, H. J., & Lea, D. W. (2004). Links between salinity variation in the Caribbean and North Atlantic thermohaline circulation. *Nature*, 428(6979), 160–3.

Schneider, E. K. (1977). Axially symmetric steady-state models of the basic state for instability and climate studies. Part II. Nonlinear calculations. *Journal of the Atmospheric Sciences*, 34(2), 280–296.

Schneider, T., Bischoff, T., & Haug, G. H. (2014). Migrations and dynamics of the intertropical convergence zone. *Nature*, 513(7516), 45–53.

Schoof, C. (2007). Ice sheet grounding line dynamics: Steady states, stability, and hysteresis. *Journal of Geophysical Research: Earth Surface*, 112(3), 1–19.

Schulz, K. G. & Zeebe, R. E. (2006). Pleistocene glacial terminations triggered by synchronous changes in Southern and Northern Hemisphere insolation: The insolation canon hypothesis. *Earth and Planetary Science Letters*, 249(3-4), 326–336.

Seager, R., Naik, N., & Vecchi, G. A. (2010). Thermodynamic and dynamic mechanisms for large-scale changes in the hydrological cycle in response to global warming. *Journal of Climate*, 23(17), 4651–4668.

Shackleton, N. J. (2000). The 100,000-year ice-age cycle identified and found to lag temperature, carbon dioxide and orbital eccentricity. *Science*, 289(5486), 1897–1902.

Shakun, J. D., Clark, P. U., He, F., Marcott, S. A., Mix, A. C., Liu, Z., Otto-Bliesner, B. L., Schmittner, A., & Bard, E. (2012). Global warming preceded by increasing carbon dioxide concentrations during the last deglaciation. *Nature*, 484(7392), 49–54.

Shi, Z., Liu, X. D., Sun, Y., An, Z., Liu, Z., & Kutzbach, J. E. (2011). Distinct responses of East Asian summer and winter monsoons to astronomical forcing. *Climate of the Past*, 7(4), 1363–1370.

Shields, C. A., Bailey, D. A., Danabasoglu, G., Jochum, M., Kiehl, J. T., Levis, S., & Park, S. (2012). The Low-Resolution CCSM4. *Journal of Climate*, 25(12), 3993–4014.

Short, D. A., Mengel, J. G., Crowley, T. J., Hyde, W. T., & North, G. R. (1991). Filtering of milankovitch cycles by earth's geography. *Quaternary Research*, 35(2), 157–173.

Sigman, D. M., Hain, M. P., & Haug, G. H. (2010). The polar ocean and glacial cycles in atmospheric CO2 concentration. *Nature*, 466(7302), 47–55.

Siongco, A. C., Hohenegger, C., & Stevens, B. (2014). The Atlantic ITCZ bias in CMIP5 models. *Climate Dynamics*.

Sluijs, A., Schouten, S., Pagani, M., Woltering, M., Brinkhuis, H., Damsté, J. S. S., Dickens, G. R., Huber, M., Reichart, G.-J., Stein, R., Matthiessen, J., Lourens, L. J., Pedentchouk, N., Backman, J., Moran, K., & the Expedition 302 Scientists (2006). Subtropical Arctic Ocean temperatures during the Palaeocene/Eocene thermal maximum. *Nature*, 441(7093), 610–613.

Solomon, S., Qin, D., Manning, M., Chen, Z., Marquis, M., Averyt, K. B., Tignor, M., & Miller, H. L., Eds. (2007). *Climate Change 2007: The Physical Science Basis*. Cambridge, United Kingdom and New York, NY, USA: Cambridge University Press.

Stap, L. B., van de Wal, R. S. W., de Boer, B., Bintanja, R., & Lourens, L. J. (2014). Interaction of ice sheets and climate during the past 800 000 years. *Climate of the Past*, 10(3), 2135–2152.

Steig, E. J., Ding, Q., Battisti, D., & Jenkins, A. (2012). Tropical forcing of Circumpolar Deep Water Inflow and outlet glacier thinning in the Amundsen Sea Embayment, West Antarctica. *Annals of Glaciology*, 53(60), 19–28.

Steig, E. J., Morse, D. L., Waddington, E. D., Stuiver, M., Grootes, P. M., Mayewski, P. A., Twickler, M. S., & Whitlow, S. I. (2000). Wisconsinan and Holocene climate history from an ice core at Taylor Dome, Western Ross Embayment, Antarctica. *Geografiska Annaler*, 82A, 213–235.

Stenni, B., Buiron, D., Frezzotti, M., Albani, S., Barbante, C., Bard, E., Barnola, J.-M., Baroni, M., Baumgartner, M., Bonazza, M., Capron, E., Castellano, E., Chappellaz, J., Delmonte, B., Falourd, S., Genoni, L., Iacumin, P., Jouzel, J., Kipfstuhl, S., Landais, A., Lemieux-Dudon, B., Maggi, V., Masson-Delmotte, V., Mazzola, C., Minster, B., Montagnat, M., Mulvaney, R., Narcisi, B., Oerter, H., Parrenin, F., Petit, J.-R., Ritz, C., Scarchilli, C., Schilt, A., Schüpbach, S., Schwander, J., Selmo, E., Severi, M., Stocker, T. F., & Udisti, R. (2011). Expression of the bipolar see-saw in Antarctic climate records during the last deglaciation. *Nature Geoscience*, 4(1), 46–49.

Stevenson, S., Timmermann, A., Chikamoto, Y., Langford, S., & DiNezio, P. (2015). Stochastically Generated North American Megadroughts. *Journal of Climate*, 28(5), 1865–1880.

Stuiver, M. & Grootes, P. M. (2000). GISP2 oxygen isotope ratios. *Quaternary Research*, 53(3), 277–284.

Tachikawa, K., Timmermann, A., Vidal, L., Sonzogni, C., & Timm, O. E. (2014). CO2 radiative forcing and Intertropical Convergence Zone influences on western Pacific warm pool climate over the past 400ka. *Quaternary Science Reviews*, 86, 24–34.

Thoma, M., Jenkins, A., Holland, D. M., & Jacobs, S. S. (2008). Modelling Circumpolar Deep Water intrusions on the Amundsen Sea continental shelf, Antarctica. *Geophysical Research Letters*, 35(18), L18602.

Tian, J., Wang, P., Cheng, X., & Li, Q. (2002). Astronomically tuned Plio-Pleistocene benthic δ^{18}O record from South China Sea and Atlantic-Pacific comparison. *Earth and Planetary Science Letters*, 203, 1015–1029.

Tiedemann, R., Sarnthein, M., & Shackleton, N. J. (1994). Astronomic timescale for the Pliocene Atlantic δ^{18}O and dust flux records of Ocean Drilling Program site 659. *Paleoceanography*, 9(4), 619–638.

Timm, O. E., Köhler, P., Timmermann, A., & Menviel, L. (2010). Mechanisms for the onset of the African Humid Period and Sahara Greening 14.5-11 ka BP. *Journal of Climate*, 23(10), 2612–2633.

Timm, O. E. & Timmermann, A. (2007). Simulation of the last 21,000 years using accelerated transient boundary conditions. *Journal of Climate*, 20(17), 4377–4401.

Timmermann, A., Friedrich, T., Timm, O. E., Chikamoto, M. O., Abe-Ouchi, A., & Ganopolski, A. (2014). Modeling obliquity and CO2 effects on Southern Hemisphere climate during the past 408 ka. *Journal of Climate*, 27(5), 1863–1875.

Timmermann, A., Knies, J., Timm, O. E., Abe-Ouchi, A., & Friedrich, T. (2010). Promotion of glacial ice sheet buildup 60-115 kyr B.P. by precessionally paced Northern Hemispheric meltwater pulses. *Paleoceanography*, 25(4), 1–9.

Timmermann, A., Okumura, Y., An, S.-I., Clement, A. C., Dong, B., Guilyardi, E., Hu, A., Jungclaus, J. H., Renold, M., Stocker, T. F., Stouffer, R. J., Sutton, R., Xie, S.-P., & Yin, J. H. (2007). The influence of a weakening of the Atlantic Meridional Overturning Circulation on ENSO. *Journal of Climate*, 20(19), 4899–4919.

Timmermann, A., Timm, O. E., Stott, L., & Menviel, L. (2009). The roles of CO_2 and orbital forcing in driving Southern Hemispheric temperature variations during the last 21000 yr. *Journal of Climate*, 22(7), 1626–1640.

Tjallingii, R., Claussen, M., Stuut, J.-B. W., Fohlmeister, J., Jahn, A., Bickert, T., Lamy, F., & Röhl, U. (2008). Coherent high- and low-latitude control of the northwest African hydrological balance. *Nature Geoscience*, 1(10), 670–675.

Tomas, R. A., Holton, J. R., & Webster, P. J. (1999). The influence of cross-equatorial pressure gradients on the location of near-equatorial convection. *Quarterly Journal of the Royal Meteorological Society*, 125(556), 1107–1127.

Tomas, R. A. & Webster, P. J. (1997). The role of inertial instability in determining the location and strength of near-equatorial convection. *Quarterly Journal of the Royal Meteorological Society*, 123(541), 1445–1482.

Trenberth, K. E. & Guillemot, C. J. (1995). Evaluation of the global atmospheric moisture budget as seen from analyses. *Journal of Climate*, 8, 2255–2272.

Tuenter, E. (2004). *Modeling orbital induced variations in circum-Mediterranean climate*. PhD thesis, Universiteit Utrecht.

Tuenter, E., Weber, S. L., Hilgen, F. J., & Lourens, L. J. (2003). The response of the African summer monsoon to remote and local forcing due to precession and obliquity. *Global and Planetary Change*, 36(4), 219–235.

Tuenter, E., Weber, S. L., Hilgen, F. J., & Lourens, L. J. (2005). Sea-ice feedbacks on the climatic response to precession and obliquity forcing. *Geophysical Research Letters*, 32(24), 2–5.

Uemura, R., Masson-Delmotte, V., Jouzel, J., Landais, a., Motoyama, H., & Stenni, B. (2012). Ranges of moisture-source temperature estimated from Antarctic ice cores stable isotope records over glacial-interglacial cycles. *Climate of the Past*, 8(3), 1109–1125.

Vallelonga, P., Barbante, C., Cozzi, G., Gabrieli, J., Schüpbach, S., Spolaor, A., & Turetta, C. (2013). Iron fluxes to Talos Dome, Antarctica, over the past 200 kyr. *Climate of the Past*, 9(2), 597–604.

van de Berg, W. J., van den Broeke, M. R., Reijmer, C. H., & van Meijgaard, E. (2006). Reassessment of the Antarctic surface mass balance using calibrated output of a regional atmospheric climate model. *Journal of Geophysical Research: Atmospheres*, 111(11), 1–15.

van den Broeke, M. (2005). Strong surface melting preceded collapse of Antarctic Peninsula ice shelf. *Geophysical Research Letters*, 32(12), 1–4.

Venz, K. A. & Hodell, D. A. (2002). New evidence for changes in Plio-Pleistocene deep water circulation from Southern Ocean ODP Leg 177 Site 1090. *Palaeogeography, Palaeoclimatology, Palaeoecology*, 182, 197–220.

Waelbroeck, C., Labeyrie, L., Michel, E., Duplessy, J., McManus, J., Lambeck, K., Balbon, E., & Labracherie, M. (2002). Sea-level and deep water temperature changes derived from benthic foraminifera isotopic records. *Quaternary Science Reviews*, 21(1-3), 295–305.

Wang, P., Tian, J., Cheng, X., Liu, C., & Xu, J. (2003). Carbon reservoir changes preceded major ice-sheet expansion at the mid-Brunhes event. *Geology*, 31(3), 239–242.

Wang, P., Tian, J., Cheng, X., Liu, C., & Xu, J. (2004a). Major Pleistocene stages in a carbon perspective: The South China Sea record and its global comparison. *Paleoceanography*, 19(4), 1–16.

Wang, P., Tian, J., & Lourens, L. J. (2010). Obscuring of long eccentricity cyclicity in Pleistocene oceanic carbon isotope records. *Earth and Planetary Science Letters*, 290(3-4), 319–330.

Wang, X., Auler, A. S., Edwards, R. L., Cheng, H., Cristalli, P. S., Smart, P. L., Richards, D. A., & Shen, C.-C. (2004b). Wet periods in northeastern Brazil over the past 210 kyr linked to distant climate anomalies. *Nature*, 432(7018), 740–3.

Wang, X., Auler, A. S., Edwards, R. L., Cheng, H., Ito, E., Wang, Y., Kong, X., & Solheid, M. (2007). Millennial-scale precipitation changes in southern Brazil over the past 90,000 years. *Geophysical Research Letters*, 34(23), 1–5.

Wang, Y., Cheng, H., Edwards, R. L., Kong, X., Shao, X., Chen, S., Wu, J., Jiang, X., Wang, X., & An, Z. (2008). Millennial- and orbital-scale changes in the East Asian monsoon over the past 224,000 years. *Nature*, 451(7182), 1090–3.

Weldeab, S., Lea, D. W., Schneider, R. R., & Andersen, N. (2007). 155,000 years of West African monsoon and ocean thermal evolution. *Science*, 316(5829), 1303–7.

Wyrwoll, K.-H., Liu, Z., Chen, G., Kutzbach, J. E., & Liu, X. (2007). Sensitivity of the Australian summer monsoon to tilt and precession forcing. *Quaternary Science Reviews*, 26(25-28), 3043–3057.

Xie, P. & Arkin, P. A. (1997). Global precipitation: A 17-Year monthly analysis based on gauge observations, satellite estimates, and numerical model outputs. *Bulletin of the American Meteorological Society*, 78(11), 2539–2558.

Xie, S.-P. (1996). Effects of seasonal solar forcing on latitudinal asymmetry of the ITCZ. *Journal of Climate*, 9, 2945–2950.

Xie, S.-P. (2005). The shape of continents, air-sea interaction, and the rising branch of the Hadley circulation. In H. F. Diaz & R. S. Bradley (Eds.), *The Hadley Circulation: Present, Past and Future* chapter 4, (pp. 121–152). Kluwer Academic Publishers.

Xie, S.-P. & Carton, J. A. (2004). Tropical Atlanctic variability: Patterns, mechanisms, and impacts. In C. Wang, S.-P. Xie, & J. A. Carton (Eds.), *Earth's Climate: The Ocean-Atmosphere Interaction* (pp. 1–26). Washington D.C.: Geophycial Monograph, AGU.

Xie, S.-P. & Philander, S. G. H. (1994). A coupled ocean-atmosphere model of relevance to the ITCZ in the eastern Pacific. *Tellus*, 46A, 340–350.

Xie, S.-P. & Saito, K. (2001). Formation and variability of a northerly ITCZ in a hybrid coupled AGCM: Continental forcing and oceanic-atmospheric feedback. *Journal of Climate*, 14, 1262–1276.

Yin, Q. Z. & Berger, A. L. (2010). Insolation and CO_2 contribution to the interglacial climate before and after the Mid-Brunhes Event. *Nature Geoscience*, 3(4), 243–246.

Zachos, J. C., Pagani, M., Sloan, L., Thomas, E., & Billups, K. (2001). Trends, rhythms, and aberrations in global climate 65 Ma to present. *Science*, 292(5517), 686–693.

Zhao, Y., Braconnot, P., Marti, O., Harrison, S. P., Hewitt, C. D., Kitoh, A., Liu, Z., Mikolajewicz, U., Otto-Bliesner, B. L., & Weber, S. L. (2005). A multi-model analysis of the role of the ocean on the African and Indian monsoon during the mid-Holocene. *Climate Dynamics*, 25(7-8), 777–800.

Ziegler, M., Tuenter, E., & Lourens, L. J. (2010). The precession phase of the boreal summer monsoon as viewed from the eastern Mediterranean (ODP Site 968). *Quaternary Science Reviews*, 29(11-12), 1481–1490.